Variations in crustal properties from teleseismic methods in the South Island, New Zealand

By

Kevin Ramlakhan

A Thesis submitted to the Faculty of Graduate Studies of

The University of Manitoba

In partial fulfillment of the requirements of the degree of

MASTER OF SCIENCE

Clayton H. Riddell Faculty of Environment, Earth, and Resources

Department of Earth Sciences

University of Manitoba

Winnipeg, Manitoba

March 2022

Abstract

Traditionally, H-k stacking of receiver functions has been used to measure the thickness and Vp/Vs ratio of the crust. This involves receiver-function deconvolution followed by stacking along the travel time curves of the Ps conversion and other later phases. Deconvolution of noisy, narrow banded receiver function data imposes a non-unique inverse problem, which can potentially introduce artefacts. The deconvolution step can be avoided by employing the transfer function method. The relationship between the vertical component and the radial component can be predicted by creating an array of synthetic transfer functions. Each transfer function is convolved with the vertical component to calculate a radial component and then the misfit between the calculated and real radial component is determined. The presence of a sedimentary layer can cause large outliers in apparent crustal thickness and Vp/Vs ratio from H-k stacking and result in unreliable measurements in sedimentary basins. The transfer function method allows the detection of sedimentary basins and resolves crustal thickness and Vp/Vs ratio without the influence of the sedimentary layer. In addition, transfer functions may be applied to areas where a more complex model of the crust is needed, whereas the H-k stacking method treats the crust as a single homogeneous layer. The transfer function approach is completed on 27 stations and over 2500 events and revealed variations of crustal thickness and V_p/V_s ratio from 15.2 – 25.6 km and 1.55 – 1.9 respectively. In addition, sedimentary thicknesses and lower crust thicknesses ranging from 0.1 – 4.4 and 4 - 15 km respectively, were resolved. The highest values of crustal thickness are located southwest near the Alpine Fault and the lowest values of crustal thickness are seen near the Otago Schist, southeast of the Alpine Fault.

Acknowledgements

I would like to use the opportunity to express my gratitude toward everyone who supported me throughout the completion of this thesis. I am thankful for their aspiring guidance, unwavering patience, and invaluable advice during this project.

First, I would like to express my sincere gratitude to my advisor, Dr Andrew Frederiksen for his continuous support, guidance, motivation, enthusiasm, and vast knowledge of seismology.

Second, I would like to acknowledge GNS Science and the Earthquake Commission for providing the data from the GeoNet project.

Third, I would like to thank the Department of Earth Sciences for their warm guidance and encouragement.

A very special thanks goes out to my family, specifically my wife for her constant love and inspiration to follow my academic endeavours.

Finally, I would like to thank my friends for always being understanding and supportive.

Table of Contents

List of Tables

List of Figures

1 Introduction

In the early 1900's, an earthquake occurred near Pokupsko, approximately 40 km southeast of Croatia. This event was of interest to the seismologist, Andrija Mohorovičić. He collected seismograms over Europe and detected an increase in seismic velocity at around 50 km depth, through the study of P and S arrival times (Mohorovicic, 1909). The amount of data was quite insignificant relative to the amount of information available today. However, due to the thick crust under the Dinarides mountain belt, the difference between the crustal and mantle arrivals occurred at a considerable distance from the source. This motivated the study of other crustal structures using seismic waves (e.g. Jeffrey's and Conrad discontinuities) and led to the recognition of the Mohorovicic discontinuity (Moho).

The Moho is described as a first order feature of the lithosphere, although there was little global mapping of the discontinuity fifty years after its discovery. In the sixties, the Moho was defined as "that level in the earth where the compressional wave velocity increases rapidly or discontinuously to a value between 7.6 and 8.6 km/s. In the absence of an identifiable rapid increase in velocity, the Mohorovicic discontinuity is taken to be the level at which the compressional wave velocity first exceeds 7.6 km/s" (Steinhart, 1967). More generally the Moho is described as the interface between the crust and the mantle, even though the crust-mantle transition thickness varies, depending on tectonic setting (Thybo *et al*., 2013).

Early maps of the crustal thickness are often underestimated due to the lower crust being misinterpreted as the Moho for the following reasons: Firstly, in refraction studies, the high velocity lower crust may be a "hidden layer". Secondly, in wide-angle reflection surveys, the strongest arrival may be due to the lower crust. Lastly, in receiver function studies, the strongest conversion may be caused by the lower crust (Thybo *et al*., 2013). Current seismic experiments

have decreased this uncertainty by improving resolution (through change in methodology and logistics), resulting in a wider depth range in crustal thickness (Thybo *et al*., 2013). Here we consider crustal thickness variations in South Island, New Zealand across the Alpine Fault. We can record teleseismic waves that interact with the large velocity contrast across the discontinuity. At the sharp boundary between the Earth's crust and mantle, the independence of primary (P) and secondary (S) waves breaks down. An incident P or S wave will generate P and S converted waves transmitted into the Earth's crust, as well as P and S waves reflected back into the mantle. From observing the separation in arrival times between the primary wave and primary to secondary conversions, an estimation of crustal thickness can be calculated. These arrival times are primarily dependent on crustal thickness (H) as well as the Vp/Vs velocity ratio (k).

Variations in the depth to Moho can be a marker for tectonic transitions and can indicate whether major faults are crustal-scale. For this study, the transfer function approach will be conducted on a data set from the South Island, New Zealand. The Alpine fault is a major strike-slip fault, which must be crustal-scale since it is located at the plate boundary between the Australian and Pacific plate. A question to answer will be if a change in Moho depth is visibly associated with the fault. As a proof of concept, the transfer function approach was applied by Frederiksen *et al*. (2015) in western Turkey, over a major strike-slip fault where there are geological differences from one side of the fault to another; in this research, I will examine whether the same is true for the Alpine Fault.

2 Imaging the Moho through Seismic Methods

2.1 Deep Reflection and Refraction

During the 1990s and 2000s, the introduction of digital recording caused a breakthrough in seismic recording and interpretation. In North America, the collaboration between the United States Geological Survey in the United States, LITHOPROBE in Canada, and IRIS/PASSCAL, lead to the development of digital recording devices. This allowed the world to have access to these instruments with high recording and storage capacity to execute large-scale exploration projects (Prodehl *et al*., 2013). Various examples are described below of imaging the Moho using refraction/wide angle reflection and conventional reflection on scales comparable to the South Island, New Zealand. Reflection has high vertical and lateral resolution but strong velocity/depth trade-off, while refraction is good at velocity versus depth but lateral resolution is poor. Wide-angle reflections are generally seen on refraction lines and are included in the refraction interpretation (Lowrie, 2007).

Among the first projects with the new digital seismic equipment were the Lithoprobe experiments in the Southern Cordillera and Abitibi-Grenville area. While Lithoprobe was in its later stages of development, Leinster Granite Seismics (LEGS), in southeast Ireland was being used in 1999. They acquired 200 TEXAN stations from the University of Texas and 100 TEXAN stations from University of Copenhagen (Figure 2.1; Prodehl *et al*., 2013). This project also incorporated magnetotelluric data and wide angle reflection profiles (VARNET experiment) to determine the overall crustal thickness of Ireland.

Figure 2.1. TEXAN instrument used for high-density recording in land-based controlled source profiling in southeastern Ireland (Prodehl et al., 2013).

An extension of the finite difference method was used to compute the reflection travel times from the Moho discontinuity. From a constant Moho depth, the algorithm was used to iteratively modify a Moho reflector until a there was an agreement for most of the PmP phases within 0.2-0.3 s. The deepest crust is found in the centre of the study area of approximately 33 km (beneath the Killarny, Mallow and Shannon Estuary region), and thins towards the southern coastline to 28-29 km, as shown in the final model in Figure 2.2 (Landes *et al*., 2003). This crustal thinning toward the coast is also seen over a gravity high, which Landes et al. suggest is attributable to the crustal thinning from the Mesozoic crustal extension in the adjacent offshore sedimentary basins.

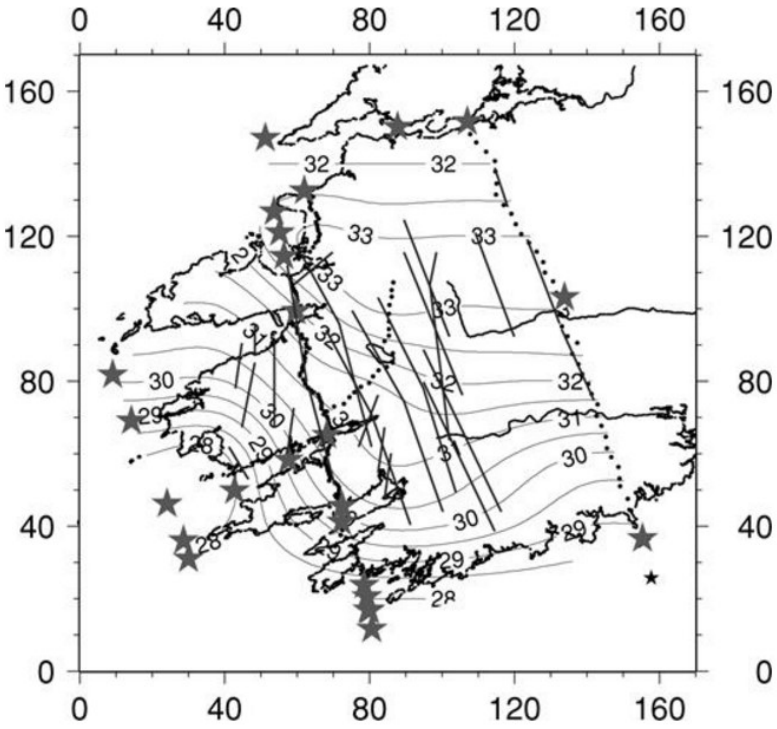

Figure 2.2. Final model of Moho discontinuity from the VARNET experiment. Dark black lines indicate reflection points (Landes et al., 2003). Water bodies and the VARNET seismic profiles are also shown (Landes et al., 2003).

The DEKORP-BASIN Group performed a seismic reflection experiment in the southeastern Baltic Sea. A grid of marine seismic reflection profiles was recorded over Sweden, Denmark, and northeastern Germany. The project was also extended onto land into northeastern Germany with a detailed seismic reflection line. Bayer et al. produced a processed reflection line with interpreted arrivals shown in Figure 2.3.

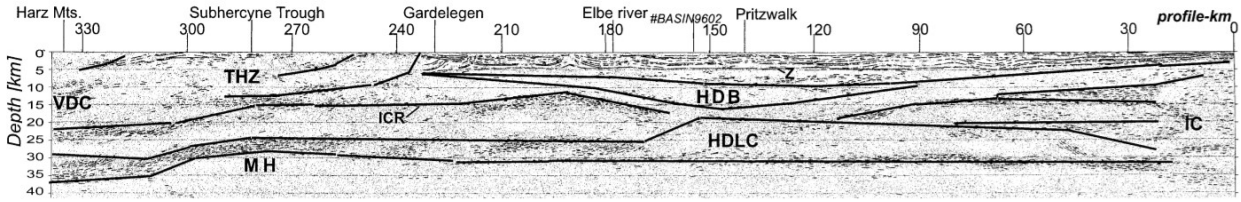

Figure 2.3. Interpretation of the seismic reflection line from the DEKORP-BASIN project (Bayer et al., 1999). From Bayer et al., 1999: Z: Base Zechstein reflector; VDC: Variscan deformed crust; MH: Moho; ICL: intracrustal layer; HDB: high-density body; HDLC: high-denisty lower crust; IC: intermediate crust.

Under the thrust zone, the Moho has an anticlinal structure with a relatively steep flank in the south and slight dip on the southern limb. Bayer et al., suggests that the morphology of this "updoming" could be a sign of buckling of the crustal plate during the late Cretaceous to Tertiary transition. In general, the reflection Moho depth in the Baltic sea was observed to be 28-35 km (Prodehl *et al*., 2013).

In Poland, the CELEBRATION-2000 (Central European Lithospheric Experiment Based on RefrAcTION) project explored the Trans-European Suture Zone (TESZ), the southwestern portion of the East European Craton, the western Carpathian Mountains, the Pannonian basin (Hungary), and the Bohemian massif (Czech Republic) (Prodehl *et al*., 2013). This project was carried out with the aid of the ALP'2000 project, with focus on the Eastern Alps and western Carpathians (Prodehl *et al*., 2013). Some profiles crossed the Bohemian Massif and others were centred on the Pannonian basin. 920 TEXAN stations were set up for 13 seismic refraction profiles (4300 km total). Record sections from the experiment are shown in Figure 2.4. The large number of TEXAN stations made it possible to make dense recordings at the same time. Maximum crustal thickness determined is approximately 55 km.

From the examples shown above, mapping crustal thickness proves difficult when looking at large scale mapping (amount of resources needed to obtain a cross section or map). In

addition, it becomes very expensive to look at the crustal thickness over a large study area. Generally, reflection has high vertical and lateral resolution but strong velocity/depth trade-off. and refraction surveys are is better at resolving velocity vs. depth but lateral resolution is poor. (Lowrie, 2007). It would require both survey types to fully characterize a large survey area, at all wavelengths to obtain a unique model (Neves and Singh, 1996). This would take considerable time, especially with denser arrays to increase resolution. It is desirable to look towards passive source seismic techniques to offset costs and still produce high quality data.

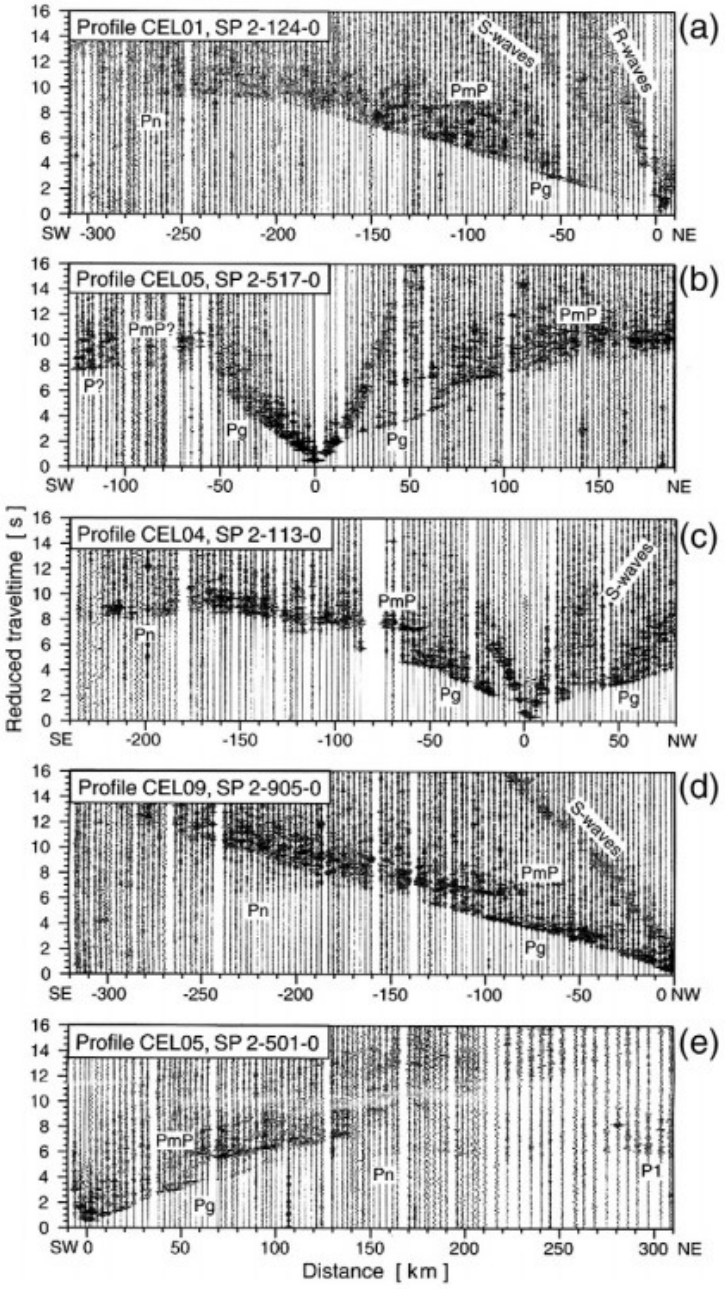

Figure 2.4. Celebration-2000 record section in Central Europe. A through E are different sections where PmP is the P response from the Moho (Prodehl et al., 2013).

2.2 Teleseismic Earthquake Techniques

2.2.1 Receiver Functions

Most parts of the world managed to sustain progress in controlled source seismology; however, in recent years, large scale refraction studies are held back by cost. Broadband seismic recording of ground motion has become widely available at observatories and for portable instrument deployments with large numbers of stations. This availability of high-quality seismological data has led to the development of a range of techniques oriented to the receiver side structure, more specifically the Moho. Such approaches mostly use the wave conversions and reverberations that accompany the onset of a teleseismic signal (Zhu and Kanamori, 2000).

A recording of a teleseismic or distant earthquake is used to represent the interaction of an incoming near-vertical waveform with the receiver-side structure. The wave can take many ray paths, as shown in Figure 2.5. At the station, the vertical component recording is often used as an approximation of the source time function. On the other hand, the radial component is dominated by P to S conversions (Ps) and is used to derive the receiver function (Zhu and Kanamori, 2000).

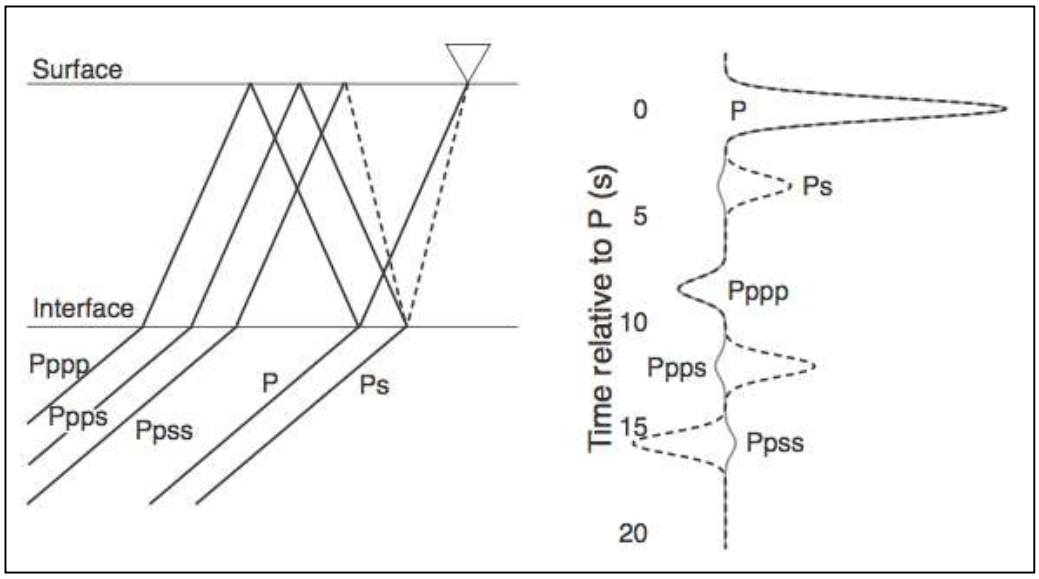

Figure 2.5. Ray paths for a teleseismic event shown on the left. Arrival times for a given ray path shown on the right. Solid lines represent arrivals that appear on the vertical component and dashed lines represent arrivals that appear on the radial component (Frederiksen, 2014).

The vertical component *z(t)* and the radial component *r(t)* are given by the equations:

$$z(t) = s(t) * g_z(t) \tag{2.1}$$

$$r(t) = s(t) * g_r(t) \tag{2.2}$$

where *s(t)* is the source time function, $g_z(t)$ is the vertical Green's function and $g_r(t)$ is the radial Green's function, and the asterisk represents convolution. The vertical Green's function is approximately equal to a delta function (ideal singular spike).

$$g_z(t) \approx \delta(t) \tag{2.3}$$

Therefore, the vertical component in Equation 2.1 can be approximated as the source time function. It is necessary to note that this approximation breaks down when the crust is not homogeneous (for example, if a sedimentary basin is present under a station).

$$z(t) = s(t) * g_z(t) \approx s(t) * \delta(t) \approx s(t) \tag{2.4}$$

Since $z(t) \approx s(t)$, Equation 2.2 becomes:

$$r(t) = z(t) * g_r(t) \tag{2.5}$$

and deconvolution of the radial component is possible to approximate the radial Green's function (the receiver function). To compute the deconvolution, the Fourier transform can be applied to Equation 2.5:

$$R(\omega) \approx Z(\omega)G(\omega) \tag{2.6}$$

and the radial Green's function can be recovered through division.

$$G(\omega) \approx \frac{R(\omega)}{Z(\omega)} \tag{2.7}$$

In practice, $z(t)$ is noisy and zero at some frequencies, therefore the above equation is reformulated to:

$$G(\omega) \approx \frac{R(\omega)Z^*(\omega)}{Z(\omega)Z^*(\omega) + \lambda^2} \tag{2.8}$$

where $Z^*(\omega)$ is the complex conjugate of $Z(\omega)$ and λ is the damping factor. The introduction of the complex conjugate ensures that the denominator is a real number ($\in \mathbb{R}$), and so that the damping factor does not incur a phase change (i.e. the denominator is zero phase). Finally, the inverse Fourier transform is applied to Equation 2.8 to obtain the receiver function (Zhu and Kanamori, 2000).

Calculating a set of receiver functions through deconvolution can be difficult when there are not enough earthquakes from all azimuths and additional smaller events must be included to fill in the gaps. With the introduction of these weaker signals, the deconvolutions yield noisy receiver functions (Ligorria and Ammon, 1999). To reduce the noise, a least squares

simultaneous deconvolution can be done for any number of seismograms at a given azimuth (Bostock, 1998). Equation 2.8 can be altered to Equation 2.8b for N seismograms:

$$G(\omega) \approx \frac{\sum_n^N R_n(\omega) {Z_n}^*(\omega)}{\sum_n^N Z_n(\omega) {Z_n}^*(\omega) + \lambda^2} \quad 2.8b$$

Generally, the Moho is the strongest velocity contrast on the receiver side of the teleseismic wave and therefore produces the strongest arrivals in the receiver function (Lowrie, 2007). As mentioned in the previous section, the radial component consists of the Ps conversion and multiples (PpPs and PpSs) (Zhu and Kanamori, 2000). The difference between the P and Ps conversion arrivals can be used to estimate crustal thickness:

$$H = \frac{t_{Ps}}{\frac{1}{V_s}\left(\sqrt{1 - p^2 {V_s}^2}\right) - \frac{1}{V_p}\left(\sqrt{1 - p^2 {V_p}^2}\right)} \quad 2.9$$

where t_{ps} is the time separation between Ps and P, Vp, Vs are the crustal P and S velocity respectively, and p is the ray parameter (a quantity that can be calculated from the epicentral distance from the earthquake) of the incident wave (Frederiksen, 2014). Estimating crustal thickness using only Equation 2.9, it trades off strongly with crustal velocities, particularly Vp/Vs (Vp/Vs = k). Additional constraints can be introduced by using the later phases and reducing ambiguity so H and k can both be calculated:

$$H = \frac{t_{PpPs}}{\frac{1}{V_s}\left(\sqrt{1 - p^2 {V_s}^2}\right) + \frac{1}{V_p}\left(\sqrt{1 - p^2 {V_p}^2}\right)} \quad 2.10$$

$$H = \frac{t_{PpSs}}{\frac{2}{V_s}\left(\sqrt{1 - p^2 {V_s}^2}\right)} \quad 2.11$$

Identifying and measuring the Ps conversion and associated multiples from a discontinuity on a single receiver function can be difficult due to scattering from crustal heterogeneities, other Ps conversions from other discontinuities, and background noise (Zhu and Kanamori, 2000). By stacking receiver functions from multiple events, the signal to noise ratio can be boosted. This H-k stacking method is done in the time domain and defined as:

$$S(H,k) = w_1 r(t_{Ps}) + w_2 r(t_{PpPs}) + w_3 r(t_{PpSs}) \quad 2.12$$

where *r(t)* is the radial receiver function at the Ps, PpPs, and PpSs conversion arrival times corresponding to the H and k values in Equations 2.9, 2.10 and 2.11. A weighting is assigned to each arrival as they are summed together, such that all the weights added together equal one. The S(H, k) reaches a maximum once all three conversions are stacked coherently with the correct H and k, as shown in Figure 2.6 (Zhu and Kanamori, 2000). The derived crustal thickness and Vp/Vs values should be regarded as apparent values, considering that this technique treats the crust as a single homogeneous layer (Darbyshire *et al*., 2007).

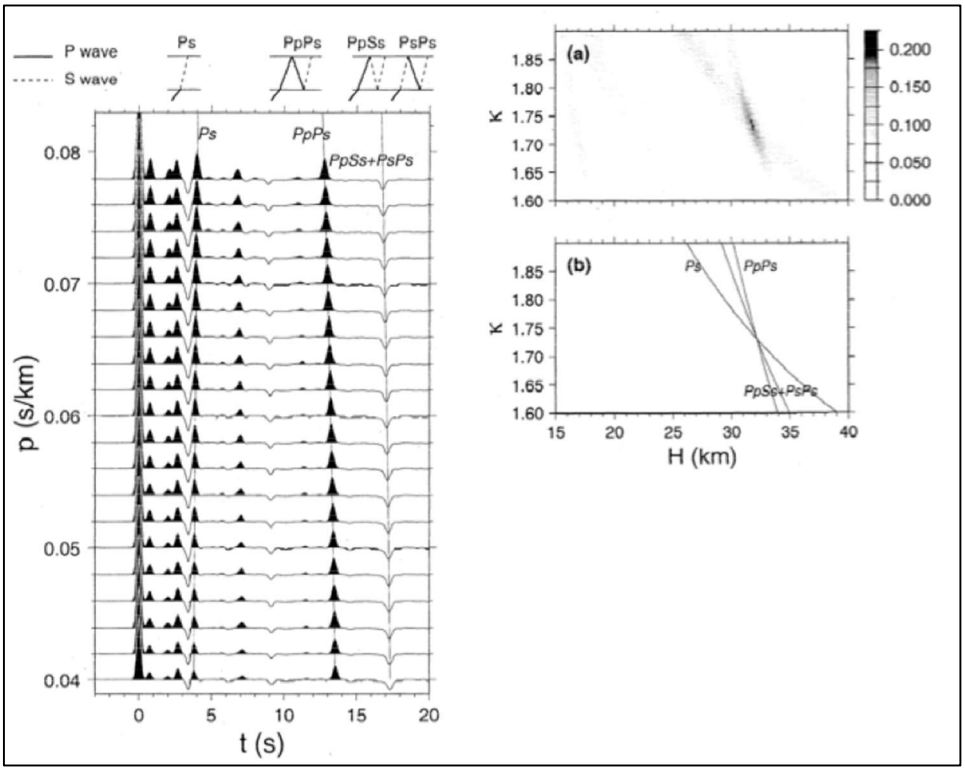

Figure 2.6. The plot on the left displays the radial receiver functions as a function of ray parameter. The travel times for Ps, PpPs and PpSs are labeling with their ray paths outlined above. The right plot (a) shows the results of Equation 12 once S (H, k) reaches the maximum (solid area) when correct values of H and k are used during stacking. The relationship between H and k (b) as shown in Equation 2.9-2.11, for different phases shown in the plot on the right. Contributions for each phase in stacking is represented by its associated curve, and where they converge is the solution for H and k (Zhu and Kanamori, 2000).

To achieve better resolution, it is possible to stack the traces using the nth-root stacking technique (Rost and Thomas, 2009). Instead of applying a linear stack,

$$\sum_{i=1}^{N} d_i \qquad 2.13$$

where, $d_i = d_1, d_2, d_3, \ldots d_N$

a non-linear stacking method is used to improve the signal to noise ratio:

$$\left(\sum_{i=1}^{N} \text{sign}(d_i) * |d_i|^{\frac{1}{n}} \right)^n \qquad 2.14$$

The sign of each sample is preserved and therefore the polarities of the stacked traces are correct. Taking the nth-root of the individual traces reduces the amplitude variance of each trace and the processing boosts the coherency of the signal rather than the amplitudes. After the summation is completed, the nth power is taken and effectively enhances the amplitude differences again. In this study the 4^{th} root is used like the vespagrams shown in Rost and Thomas, (2009).

There are several advantages and disadvantages to the H-k stacking method. Firstly, from obtaining a value for the Vp/Vs ratio, it is possible to constrain the mafic content beneath the station. Generally, a higher Vp/Vs implies that the material between the station and the Moho is more mafic or higher fluid content. Secondly, by stacking multiple receiver functions we can conveniently process massive amounts of teleseismic data (Zhu and Kanamori, 2000). Thirdly, picking travel times for converted phases is not necessary. Lastly, by stacking receiver functions from different locations, the effect of lateral structure variations is repressed, resulting in an average crustal model. Zhu and Kanamori (2000) suggest that calculating measurements directly from stacking receiver functions is more robust than estimates just using the Ps and PpPs conversions. The later phase (PpSs+PsPs), which takes a longer ray path through the crust than the primary conversion and has an extra reflection on the surface, is much more sensitive to lateral structural variations. Dipping Moho or surface topography is a good example of this, where a small dip angle (5°) can change the arrival time of the PpPs phase by 3 s depending on if the incoming wave is propagating in the updip or downdip directions. The effects of lateral variations are significantly reduced from the Zhu and Kanamori (2000) style algorithm using receiver functions from different directions and distances. However, H-k stacking can fail in areas with a strong intracrustal interface. An example of this would be in an area with a deep sedimentary basin such as the Williston basin. In sedimentary basins, there are high velocity

contrasts between the sediments and the basement rock that generate large basin reverberations that mask the later Moho conversions (Zhu and Kanamori, 2000). In addition, the range of slowness in a receiver function study is not enough to remove the ambiguity in the velocity-depth information and a priori information is needed (Ammon, 1990).

2.2.2 Transfer Functions

The Earth is not really a one-layer problem; therefore, a different approach is desirable. We can go back to Equations 2.1 and 2.2 in the frequency domain, shown below as Equations 2.15 and 2.16.

$$R(\omega) = S(\omega)G_r(\omega) \tag{2.15}$$

$$Z(\omega) = S(\omega)G_Z(\omega) \tag{2.16}$$

The deconvolution step can be avoided by manipulating Equations 2.15 and 2.16 to produce Equation 2.17, which demonstrates a relationship between the vertical and radial components. The vertical and radial Green's functions can be combined into a single term called the transfer function (Frederiksen and Delaney, 2015).

$$R(\omega) = \frac{G_r(\omega)}{G_z(\omega)} Z(\omega) = T_{zr}(\omega)Z(\omega) \tag{2.17}$$

Synthetic transfer functions can be generated to predict the relation between the vertical and radial components. Using a large set of precalculated transfer functions, the convolution between the measured vertical component and each transfer function can be computed to produce a theoretical radial function. The precalculated transfer functions can be produced from a suite of geological models that have each parameter, such as thickness or velocity, changed in small increments (a traditional grid search procedure). Another method to produce precalculated transfer functions is to change each parameter randomly between a set maximum and minimum

(a Monte Carlo style search). A misfit can then be calculated using either method by determining the error between the predicted and real radial components by calculating the root mean square difference, that is not affected by deconvolution artefacts (Frederiksen and Delaney, 2015). In the time domain, assuming ray-theoretical wave propagation in the pre-critical regime, where each layer is represented by a constant velocity and separated by sharp, flat interfaces, the vertical and radial Green's functions are:

$$g_r(t) = \sum_{j=1}^{N} a_j \delta(t - t_j) \tag{2.18}$$

$$g_z(t) = \sum_{j=1}^{N} b_j \delta(t - t_j) \tag{2.19}$$

The Green's functions are spike series, where t_j is the travel time of the jth arrival, a_j, b_j are the amplitudes of the radial and vertical components respectively, and δ is the Dirac delta function (Frederiksen and Delaney, 2015). The Fourier transform is applied to Equations 2.18 and 2.19 to produce Equations 2.20 and 2.21, in the frequency domain.

$$G_r(\omega) = \sum_{j=1}^{N} a_j e^{-i\omega t_j} \tag{2.20}$$

$$G_r(\omega) = \sum_{j=1}^{N} b_j e^{-i\omega t_j} \tag{2.21}$$

Then the transfer function is obtained by dividing Equation 20 and Equation 21. This implies spectral division; however, the denominator is full-band and the transfer function will be uniquely determined (Frederiksen and Delaney, 2015).

$$T_{zr}(\omega) = \frac{\sum_{j=1}^{N} a_j e^{-i\omega t_j}}{\sum_{j=1}^{N} b_j e^{-i\omega t_j}} \tag{2.22}$$

An example of one and two-layer crustal models is shown in Figure 2.7, with sample vertical and radial Green's functions and corresponding Z-R transfer functions. As mentioned in the previous section, the presence of a sedimentary layer introduces serious complexity to the radial Green's function. The conversion at the base of the sedimentary layer generates a second peak that causes the P arrival to appear delayed on the radial component. This effect is stronger on the transfer function and contains oscillatory sequences that may obscure the converted and reverberated arrivals of the Moho. The presence of these basinal effects in transfer functions indicates that modelling the transfer functions will account for them (Frederiksen and Delaney, 2015). In addition, in the two-layer crust model, the vertical Green's function has a negative spike at approximately 1 s which violates the assumption that the vertical Green's function is approximately equal to a delta function (Equation 2.3).

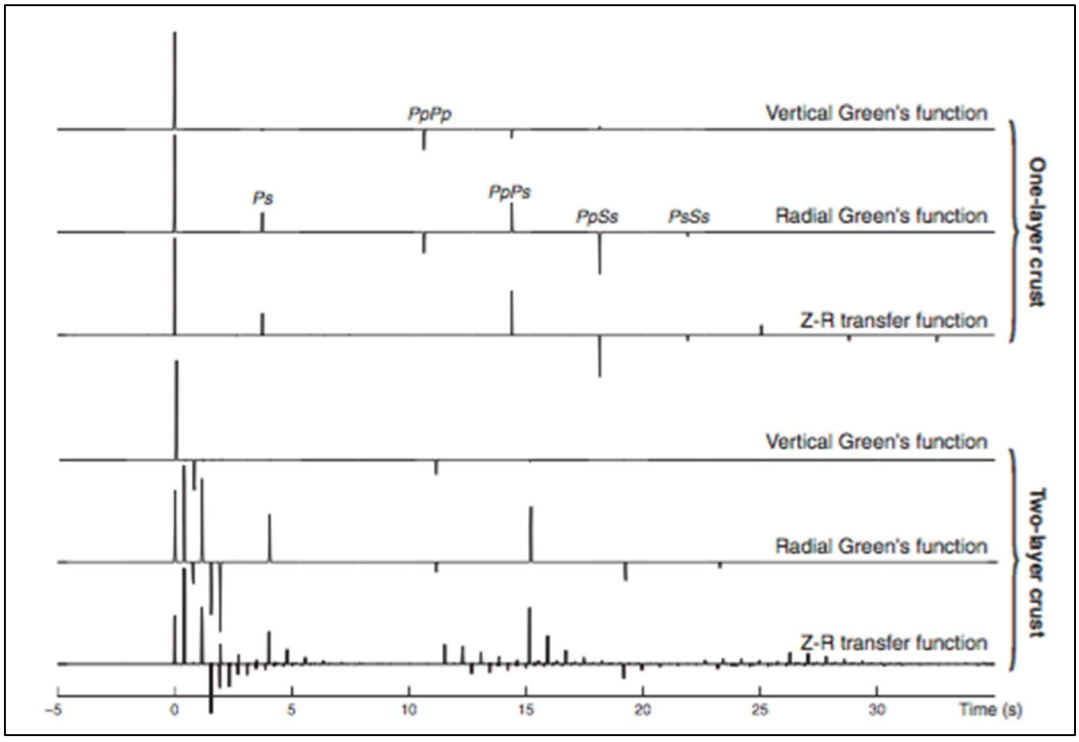

Figure 2.7. Example of Green's functions and corresponding transfer functions for a one and two-layer crustal model (Frederiksen and Delaney, 2015).

The transfer function approach was used in a study done in the Williston basin and adjacent areas, which sit on the Superior basement, by Frederiksen and Delaney (2015). Earthscope broadband seismometers were used to record events greater than magnitude 6 in the teleseismic range (30 - 100° or 3336 – 11120 km) from 2009 to 2011. The results of the H-k stacking are shown in Figure 2.8. The results shown are quite consistent between the linear stack and the 4th root stack. Both show crustal thinning from east to west. The size of the circles represents the quality of the station. Moving westward the sizes of the circles decrease, indicating that the presence of the Williston basin reduces the quality of the stack.

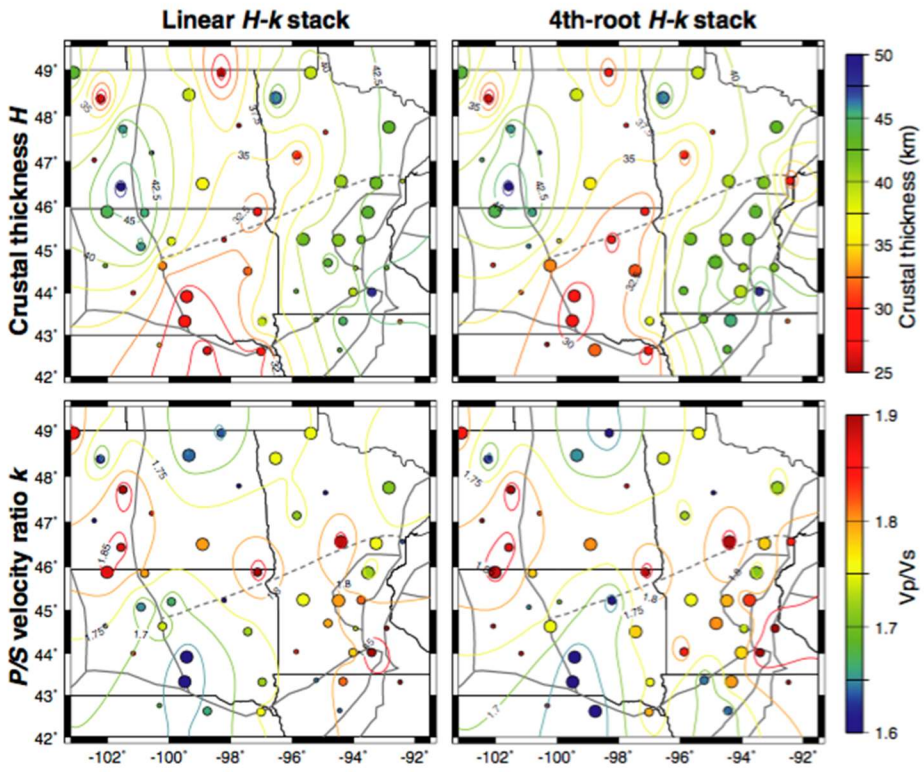

Figure 2.8. H-k stacking results in Superior Province by Frederiksen and Delaney, 2015. On the left panel is the linear stack and, on the right, is the 4th root stack.

In addition, Frederiksen and Delaney performed the transfer function method using a grid search procedure for a one and two-layer model. The resulting misfit map for the best fitting one

and two-layer crustal model is shown in Figure 2.9. In the one-layer model, an increase in error westward corresponds to the sedimentary basin thickness along with a localised zone of high misfit centred in northeastern South Dakota (Frederiksen and Delaney, 2015). The two-layer result generally shows a lower misfit and less of an increase in error westward.

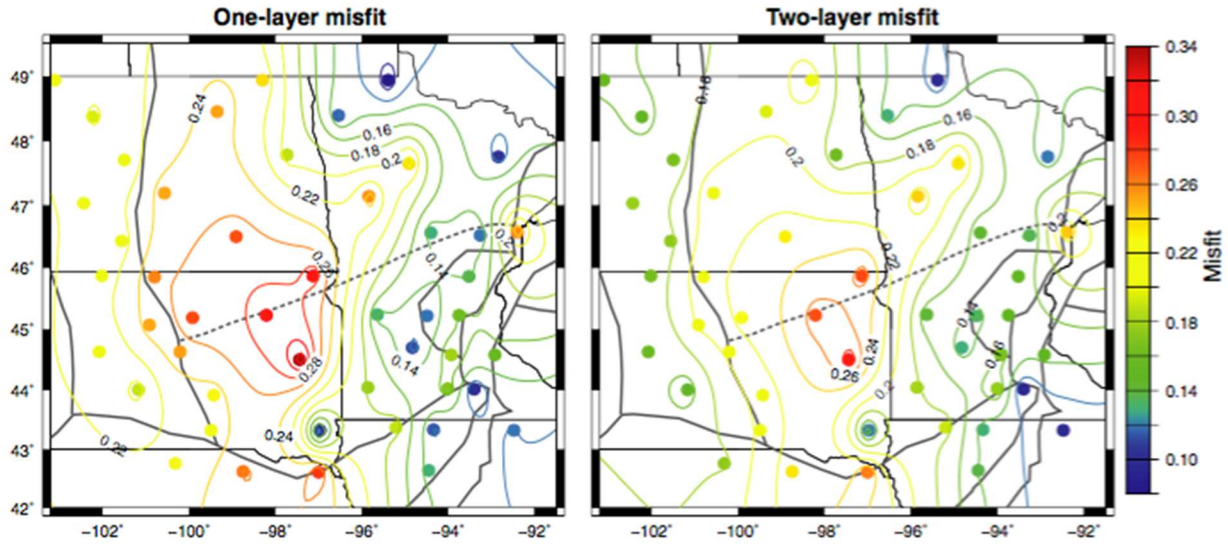

Figure 2.9. Misfit map for a one and two-layer crustal model using the transfer function method, in the Superior Province (Frederiksen and Delaney, 2015).

The final results of the experiment are shown in Figure 2.10. The first panel is a combination of the one and two-layer model. In other words, for each station, whichever model gave a lower misfit was the model that was used. The recovered crustal thickness variation is significantly different than the results from the H-k stack, mostly because the spatial pattern is more consistent with fewer outliers. The second panel is sedimentary thickness. In general, the thickness of sedimentary layer increases from east to west. The third panel is the difference in crustal thickness between the first panel and the 4th root stacking result shown previously. The largest different in crustal thickness is in the southeast and the northwest of the study area. The fourth panel is the Vp/Vs ratio of the basement rock. The velocity ratio using the transfer

function method is related to the basement rock, compared to resulted using the H-k stack method, which is presumably influenced by the sedimentary basin (Frederiksen and Delaney, 2015).

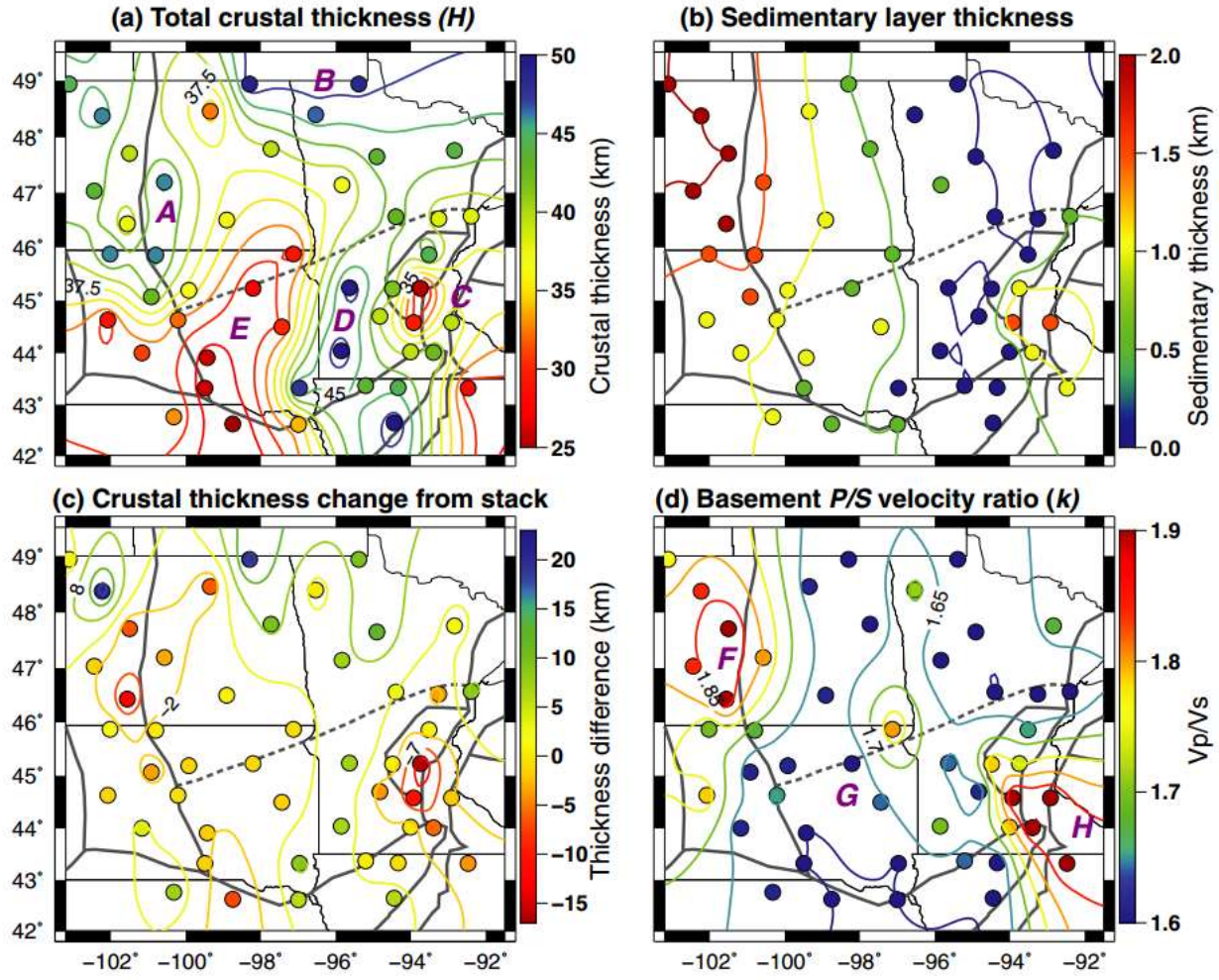

Figure 2.10. Final results of experiment. A: Total crustal thickness resolved from transfer function technique. B: Sediment layer thickness from best fitting two-layer model. C: Difference between crustal thickness model obtained from H-k stacking of receiver functions and the transfer function technique. D: Vp/Vs ratio of the basement rock (Frederiksen and Delaney, 2015).

A transfer function study was conducted along the northern boundary of the Anatolian Plate is the North Anatolian Fault Zone (NAFZ) which is analogous to what this project is trying to accomplish across the Alpine Fault. The NAFZ is a young geological feature formed by

westward propagation, that is a 1500 km long right-lateral strike-slip fault (Frederiksen *et al*., 2015). In western Turkey, the NAFZ is separated into two strands, the northern strand and the southern strand. The northern strand has been the most seismically active of the two and has been the source of two major earthquakes in 1999 (Barka *et al.,* 2002; Gülen *et al.,* 2002).

To understand the NAFZ and the relationship between the northern and southern strands, 66 broadband seismometers were deployed in western Turkey from May 2012 through September 2013 (Kahraman *et al*., 2015). Figure 2.11 outlines the distribution of the stations, six north-south trending lines with 11 stations each, and seven stations surrounding the array in a semi-circle (Frederiksen *et al*., 2015). Over 16 months, teleseismic data was recorded for events with magnitude greater than 5.5.

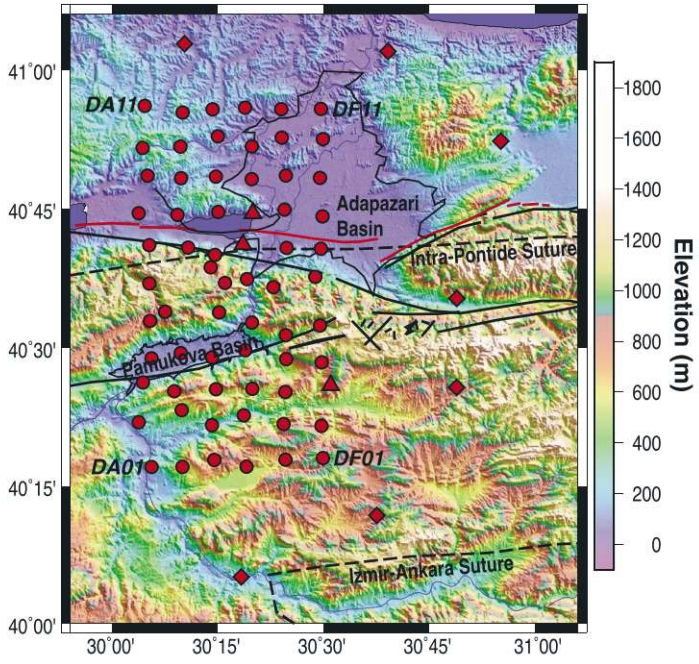

Figure 2.11. Seismometer distribution over the study area, overlying topographic map provided by NASA Shuttle Radar Topographic Mission. Circles represent stations from the SEIS-UK Dense Array and the diamonds represented by the stations operated by Kandilli Observatory. Thick black lines outline the fault and the dashed black lines outline the suture zones (Frederiksen et al., 2015).

The transfer function technique was employed to perform a grid search over three parameters: total crustal thickness, Vp/Vs of the basement rock and the thickness of the overlying sediment layer. The misfit was then calculated to determine the difference in observed and calculated radial components, then plotted for each station. The first panel in Figure 2.12 shows the variation in misfit over the study area, where stations in black were excluded (misfit greater than 0.18). The second panel outlines the variation is sediment layer thickness. Only two stations were better fitted by a one-layer model, the rest were fitted with a two-layer model, with sediment thicknesses ranging from 1.5-5.5 km. Two thick zones, over 3.5 km are resolved: one to the north of the northern strand and one overlying the southern strand. The third and forth panel show the error calculated for the crustal thickness and the Vp/Vs ratio respectively (Frederiksen *et al*., 2015).

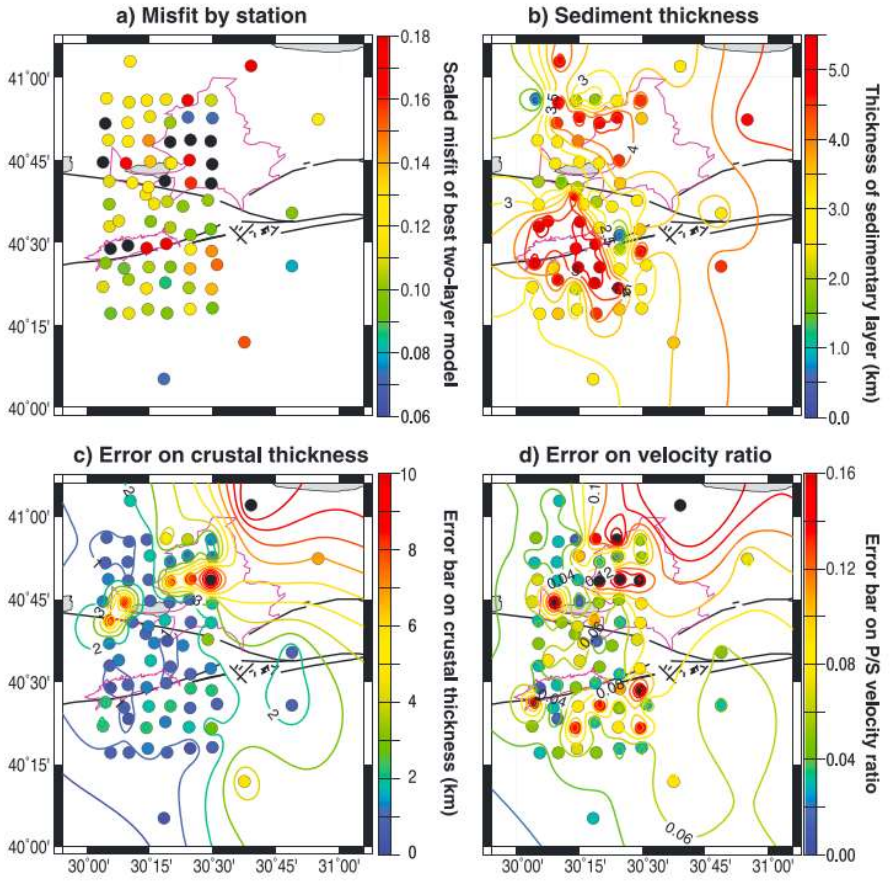

Figure 2.12. A: Variation in misfit between the observed and calculated radial components. B: Sediment layer thickness from best fitting two-layer model. C: Error derived for crustal thickness. D: Error derived for Vp/Vs ratio (Frederiksen et al., 2015).

Total crustal thickness increases from the south to the north, ranging from 30-45 km (Figure 2.13). The thickest crust is located north of the northern strand, followed by thinner crust less than 40 km, south of the northern strand. There is more of a variation in Vp/Vs of the basement rock than the total crustal thickness. This is most likely due to a more complex structure not being adequately represented by a two-layer model. However, there is a distinct increase in Vp/Vs, south of the southern strand. A possible explanation for the increase in crustal thickness north of the northern strand and the increase in Vp/Vs south of the southern strand, is that both strands follow pre-existing geological features related to the Tethyan accretion.

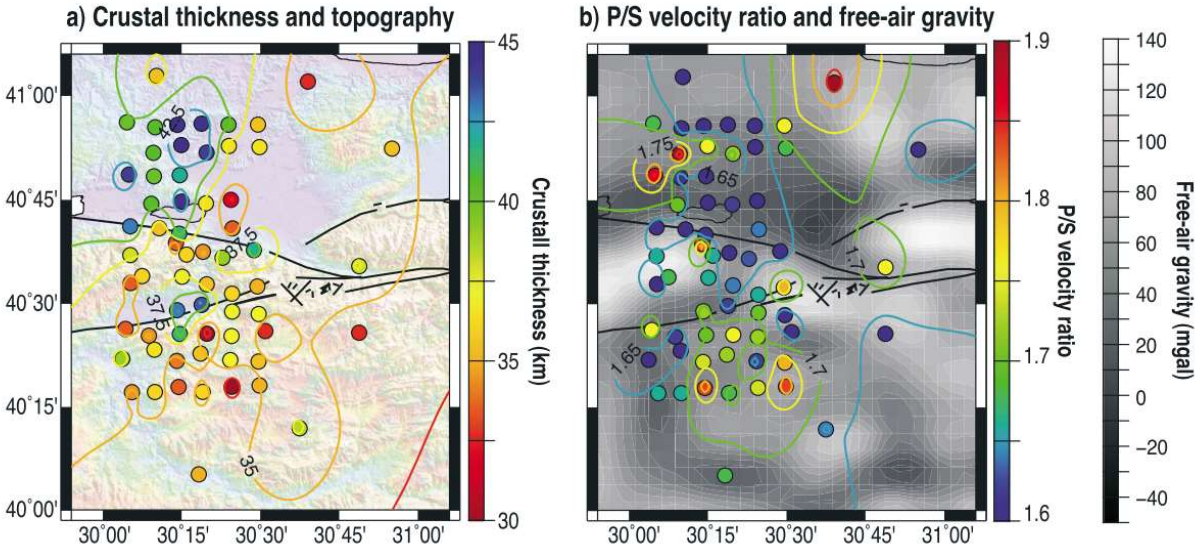

Figure 2.13. A: Total crustal thickness, superimposed on a topographic map from NASA Shuttle Radar Topographic Mission. B: Vp/Vs ratio of the basement rock, superimposed on free-air gravity map from RGM2008 global model (Frederiksen et al., 2015).

3 Regional Geology and Tectonics

3.1 Plate Tectonics

The South Island, New Zealand, lies on the margin of the Pacific Plate and the Australian Plate (Figure 3.1). This plate boundary can be split up into three zones described below from north to south (Bourguignon, 2009):

1. The Pacific Plate is subducting under the Australian Plate at the Hikurangi Trough, north of the South Island. This system extends southward into the Hikurangi Plateau, where it subducts beneath the North Island, New Zealand (Salmon, *et al.,* 2013). The Hikurangi subduction has formed a back arc spreading centre, where continental crust forms the Central Volcanic Region. Toward the end of the Hikurangi margin, the Australian plate is being deformed in the downward direction forming the Wanganui Basin. At the south end of the North Island, subduction ceases and transitions to a series of strike slip faults, which converge into the Alpine fault.
2. The Southern Alps collision zone where the Campbell Plateau and the Chatham Rise converge obliquely with the Challenger Plateau (Walcott, 1998).
3. To the southwest of the South Island, the Australian Plate is subducting under the Pacific Plate at the Fjordland Trough and the Puysegur Trench. This is a younger subduction zone (~10 Ma) than the subduction zone in the north (~30 Ma).

The plate boundary consists of two subduction zones that are subducting in opposite directions and the Alpine Fault continental transform links them together (Walcott, 1998).

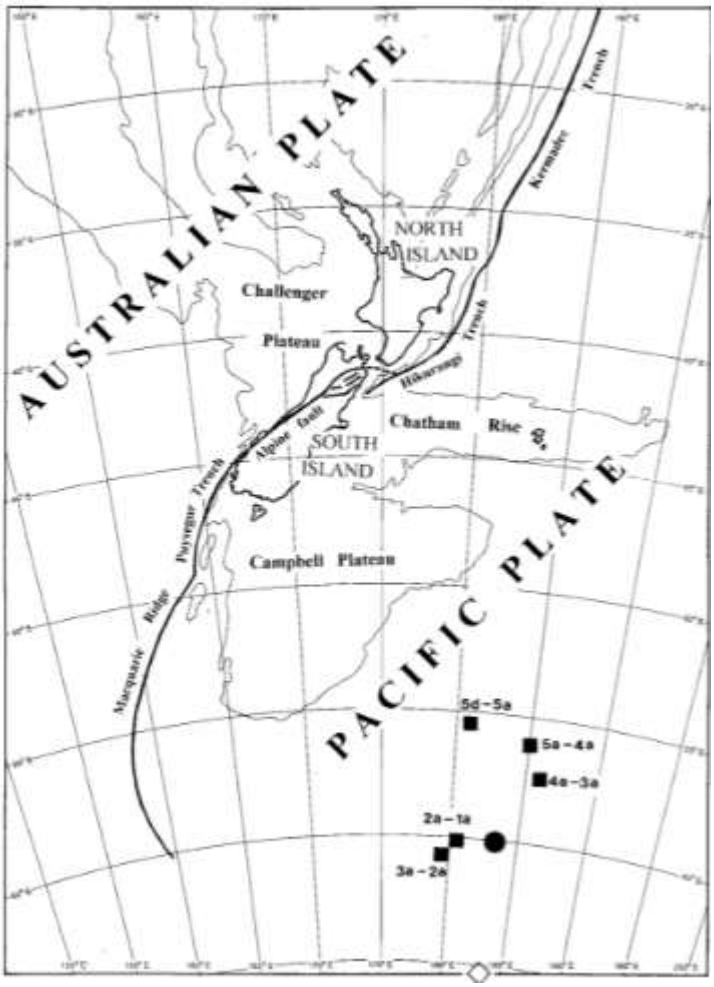

Figure 3.1. Geological setting of the New Zealand. The Australian plate is located to the west and the Pacific plate is to the east (Walcott, 1998).

3.2 Eastern Province

The geologic terranes of South Island, New Zealand can be divided into two main crustal lithotectonic subdivisions: the Eastern Province and the Western Province, separated by the Median Tectonic Zone (MTZ) as shown in Figure 3.2 (Davey *et. al.*, 1998). The Alpine Fault has offset the MTZ over South Island during the Cenozoic period such that the Eastern and Western Provinces lie largely on the Pacific and Australian plates respectively (Van Avendonk et al., 2004).

Figure 3.2: Location of the East and West Provinces relative to the Alpine Fault in South Island, New Zealand (Van Avendonk et al., 2004).

The Eastern Province lies in the southeast where the Pacific plate includes several geologic terranes that seem to have been derived from an island arc system. The majority of the central and eastern South Island is covered by the Torlesse greywackes which are quartzofeldspathic sediments that are Permian to Jurassic in age and have been deposited in the Pacific oceanic crust. The sedimentary rocks of the Eastern Province were exhumed in the early Cretaceous from the mid to lower crustal depth and because of the recent exhumation near the Alpine Fault, the grade of metamorphism of the basement ranges from greenschist in the Haast Scheist terrane to zeolite and prehnite-pumpellyite facies in the Torlesse terrane in the east (Van Avendonk et al., 2004). Toward the southwest, the Otago schist is the deepest exhumed segments

of the Late Paleozoic-Mesozoic accretionary prism that developed along the south Gondwana margin facing the paleo-Pacific Ocean (Mortimer, 2000).

3.3 Western Province

The Western Province lies in the northwest on the Australian plate which including the Nelson Westland block in the north and the Fiordland block to the south (Van Avendonk et al., 2004). These blocks are considered a fragment of Gondwana, and are comprised of lower Paleozoic metasediments that were cratonized during the mid-Paleozoic and intruded by granitoids. Accretion of the Eastern Province occurred in the early Cretaceous onto the Gondwana margin and was associated with continental arc volcanism. The Nelson block also contains granulites that constitute a significant portion of the lower crust while the upper crust is mostly characterized by metagraywackes and granitic rocks (Van Avendonk et al., 2004).

3.4 Geologic Structure and Terranes

The geological structure differs significantly between the two sides of the Alpine Fault and its extension along the Wairau Fault (Eberhart-Phillips and Reyners, 1997). Northwest of the Alpine fault is the northwest Nelson region, where the basement rocks consist of Cretaceous and Devonian-Carboniferous granite and Paleozoic sandstone and limestones (Mortimer, 1993). Northwest of the Wairau Fault, there is an area of schist is bounded on the west by a Permian terrane which includes a belt of ultramafic rocks. The region south of both faults consists largely of Torlesse terrane greywacke, which grades to schist near the Alpine Fault. The Torlesse terrane is an extensive accretionary prism which contains Permian to Early Cretaceous quartzo-feldspathic, submarine fan deposits. The Torlesse rocks in the west are Permian to Late Triassic, belonging to the Rakaia sub-terrane and the Torlesse rocks to the east are Jurassic to Early

Cretaceous and belong to the Pahau sub-terrane (Eberhart-Phillips and Reyners, 1997). These geologic structures and terranes are shown in Figure 3.3.

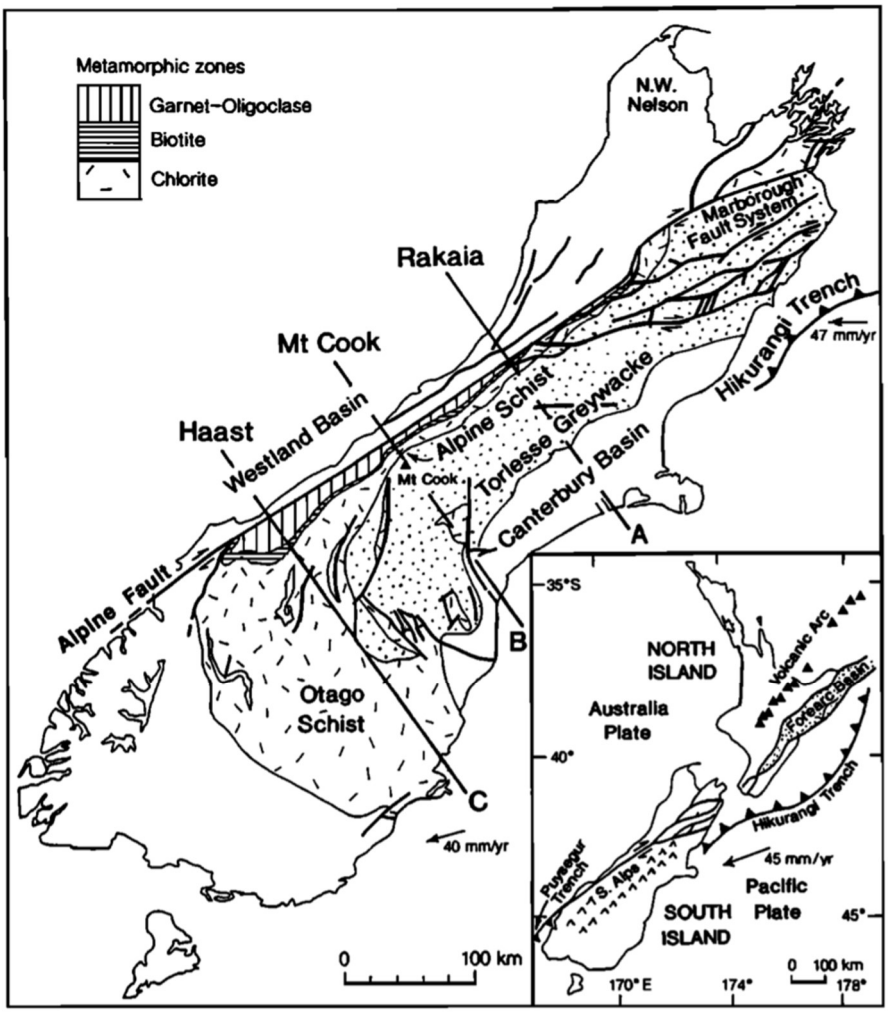

Figure 3.3: Geologic structure and terranes over South Island, New Zealand (Beaumont, et. al., 1996).

3.5 Alpine Fault

The Alpine Fault is in the centre of the island and is an oblique dextral strike-slip fault that extends approximately 460 km and strikes northeast-southwest. Toward the southwest, the dip of the fault is suggested to be around 40-55 degrees, determined from seismic reflections at

20-30 km depth (Kleffman *et. al.,* 1998). In the central area of the fault, it is suggested that the dip is about 10-15 degrees shallower, and towards the southeast (Bourguignon, 2009). Dip-slip rates of the Alpine Fault are the following:

a) 6 mm/yr in the northeast
b) 0 mm/yr in the southwest
c) 8-12 mm/yr in the centre

The strike-slip motion is less erratic, the rate being estimated to be 27 mm/yr across the entire fault (Bourguignon, 2009). The fault is currently responsible for 50-70% of plate movement and is causing the uplift of the Southern Alps along the spine of the South Island (Salmon, *et al.,* 2013).

4 Previous Geophysical Studies

4.1 Gravity

Many geophysical studies have been completed over the South Island of New Zealand, including magnetics, gravity, and seismic studies. A large airborne gravity survey was completed over both the North Island and South Island by GNS Science, Victoria University of Wellington and Land Information New Zealand (McCubbine et al, 2017). There were negative gravity anomalies found throughout the centre of the island and positive anomalies seen along the northwest, southwest and southeast coasts.

An expanded ground gravity dataset was acquired in the central West Coast of New Zealand South Island and interpreted along with data from the New Zealand Primary Gravity Network and the South Island Geophysical Transect (SIGHT) shown in Figure 4.1 (Davy et. al., 2013). The gravity along the northmost line of the SIGHT transect was modelled to delineate the South Westland Fault, which is a thrust fault system northwest (~20 km) and striking subparallel to the Alpine Fault. The gravity model over the South Westland Basin allows the prediction of the depth of the basin along the profile shown in Figure 4.2. On the northwest end of the profile the basin reaches approximately 3 km and shallows to 1.2 km towards the east approaching the South Westland Fault (Davy et. al., 2013). These predictions will assist in making assumptions for the density and depth constraints for the sedimentary layer in the transfer function approach.

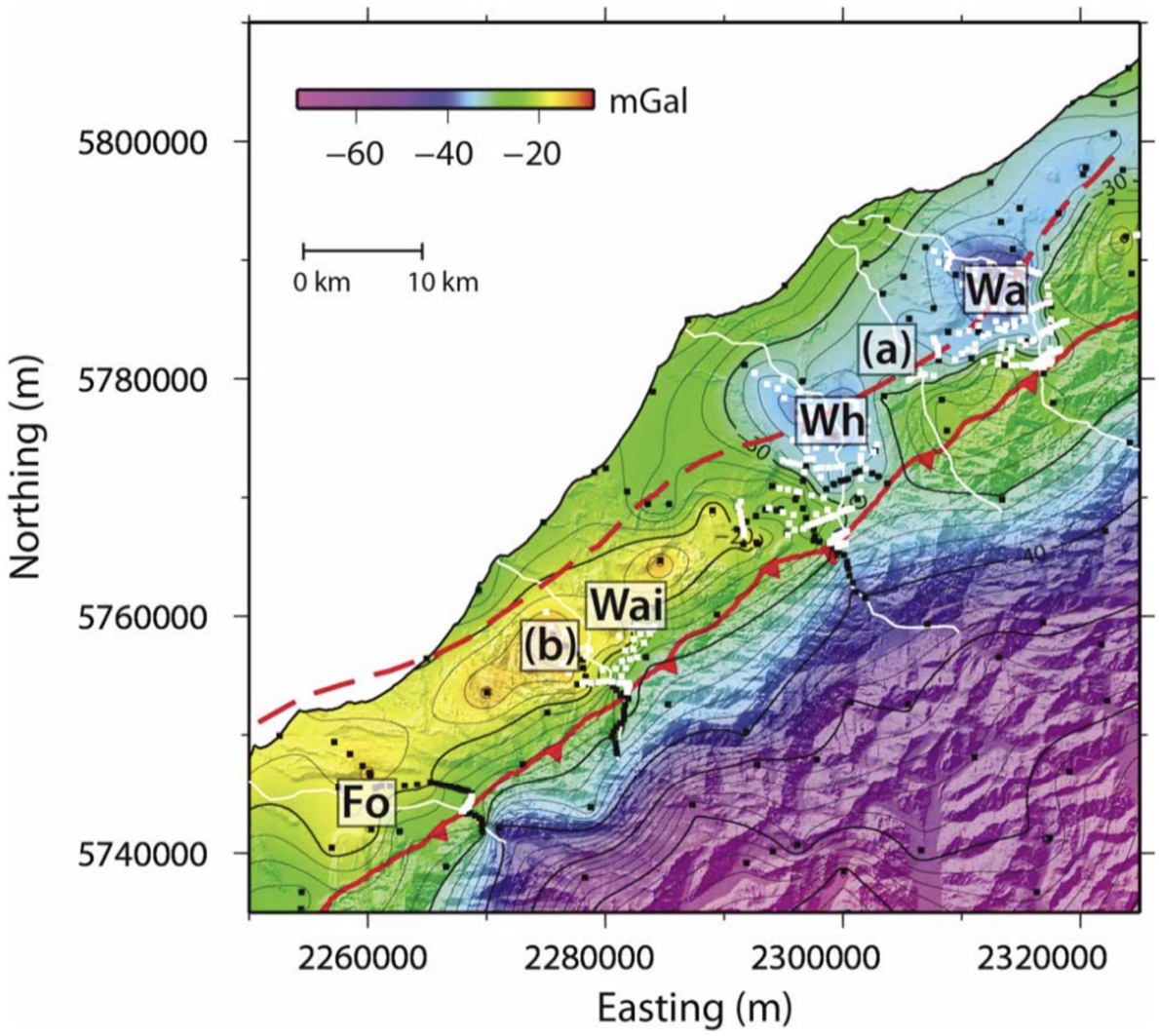

Figure 4.1: New gravity stations are denoted as white squares, and historic gravity stations are denoted as black squares overlain on a Bouguer gravity map provided by Reilly & Whiteford (1972). Structures are superimposed on the map as a dashed red lines (South Westland Fault) and solid red lines (Alpine Fault) (Davy et. al., 2013).

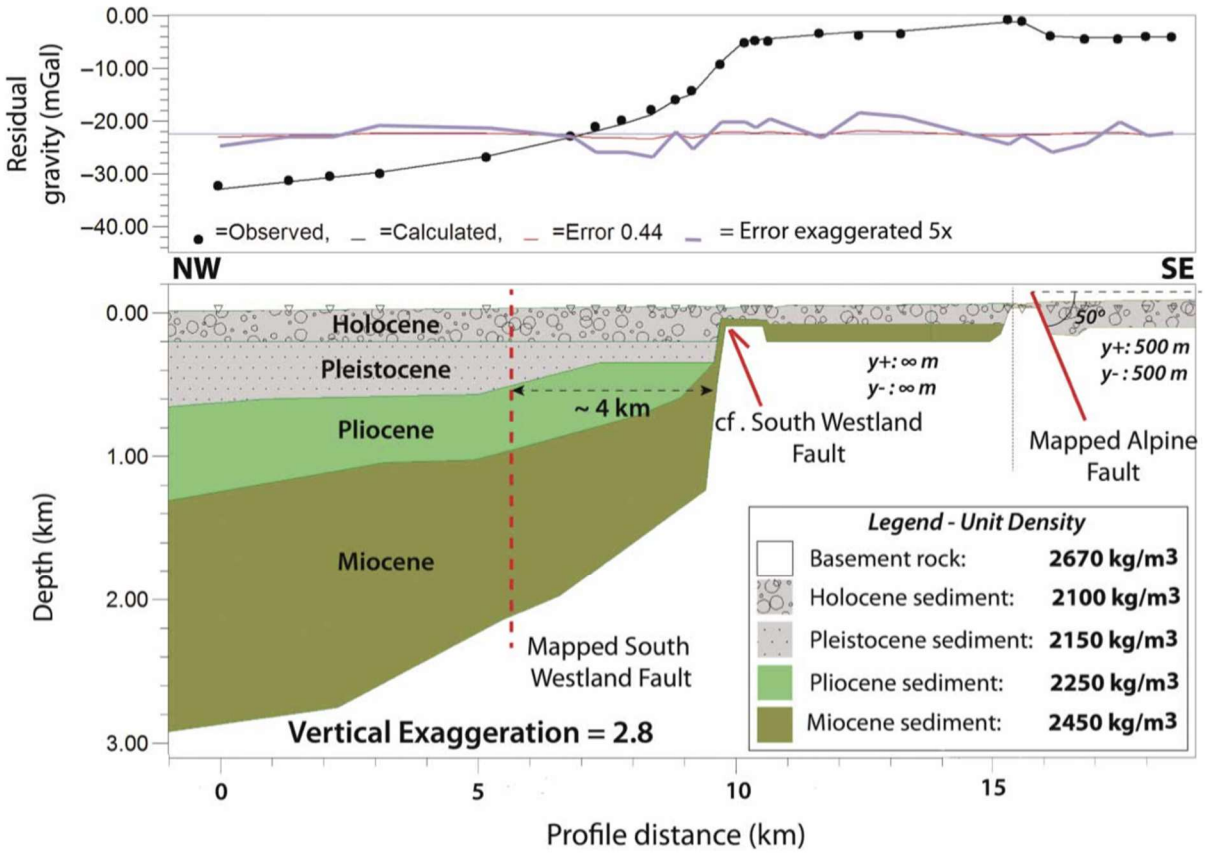

Figure 4.2: Gravity model for the data along the SIGHT transect line 1. Four units were included for the South Westland Basin and the fault locations (South Westland Fault and Alpine Fault) are approximated in model.

4.2 Magnetotellurics

Magnetotellurics uses passive electromagnetic waves as sources to image the resistivity structure of the Earth at crustal and mantle scales (Wannamaker, et. al., 2002). As a part of the South Island Geophysical Transect (SIGHT) experiment, forty-one wideband magnetotelluric (MT) soundings were measured along the northern transect shown in Figure 4.3 (Davey *et al*., 1998). Two inversion algorithms were used on the MT data and both yielded similar results, both showing a lower crust of moderate to low conductivity on the west side of the island (Wannamaker, et. al., 2002). The conductivity in this area is resolved much better with

transverse magnetic (TM) mode data, where the current flows perpendicular to strike (as opposed to transverse electric mode where the current flows parallel to strike) (Wannamaker, et. al., 2002). In addition, there is a deep crustal conductor under the Southern Alps, which is interpreted by Wannamaker, et. al., (2002) as a volume of fluid arising from prograde metamorphism within a thickening crust (Figure 4.4). The underlying mantle is relatively lower conductivity than the overlying crust, which allows the Moho boundary to be resolved as shown in the interpreted resistivity section shown in Figure 4.5 (Wannamaker, et. al., 2002).

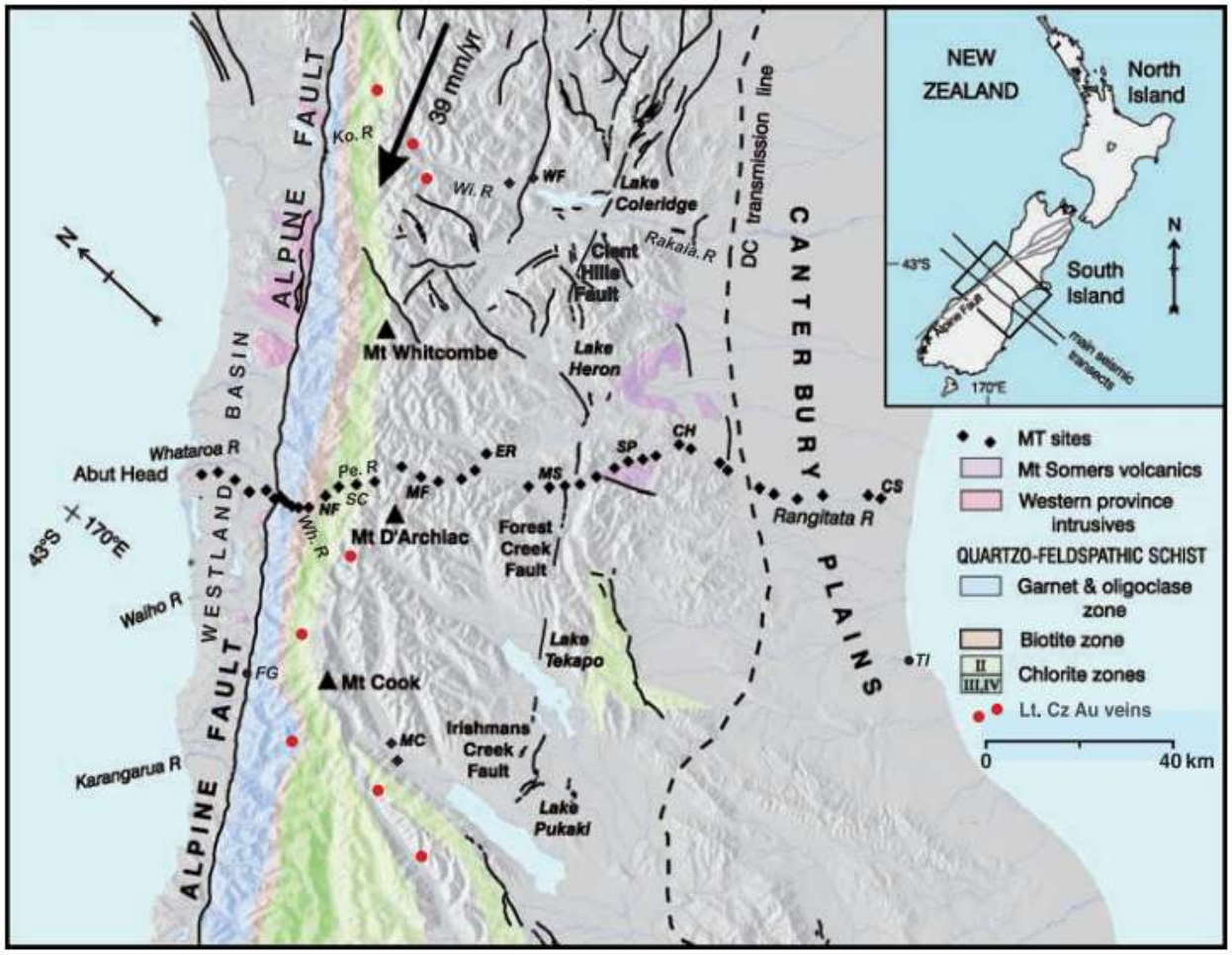

Figure 4.3: MT sounding locations denoted by the diamonds overlying relief elevation and geology (Wannamaker, et. al., 2002).

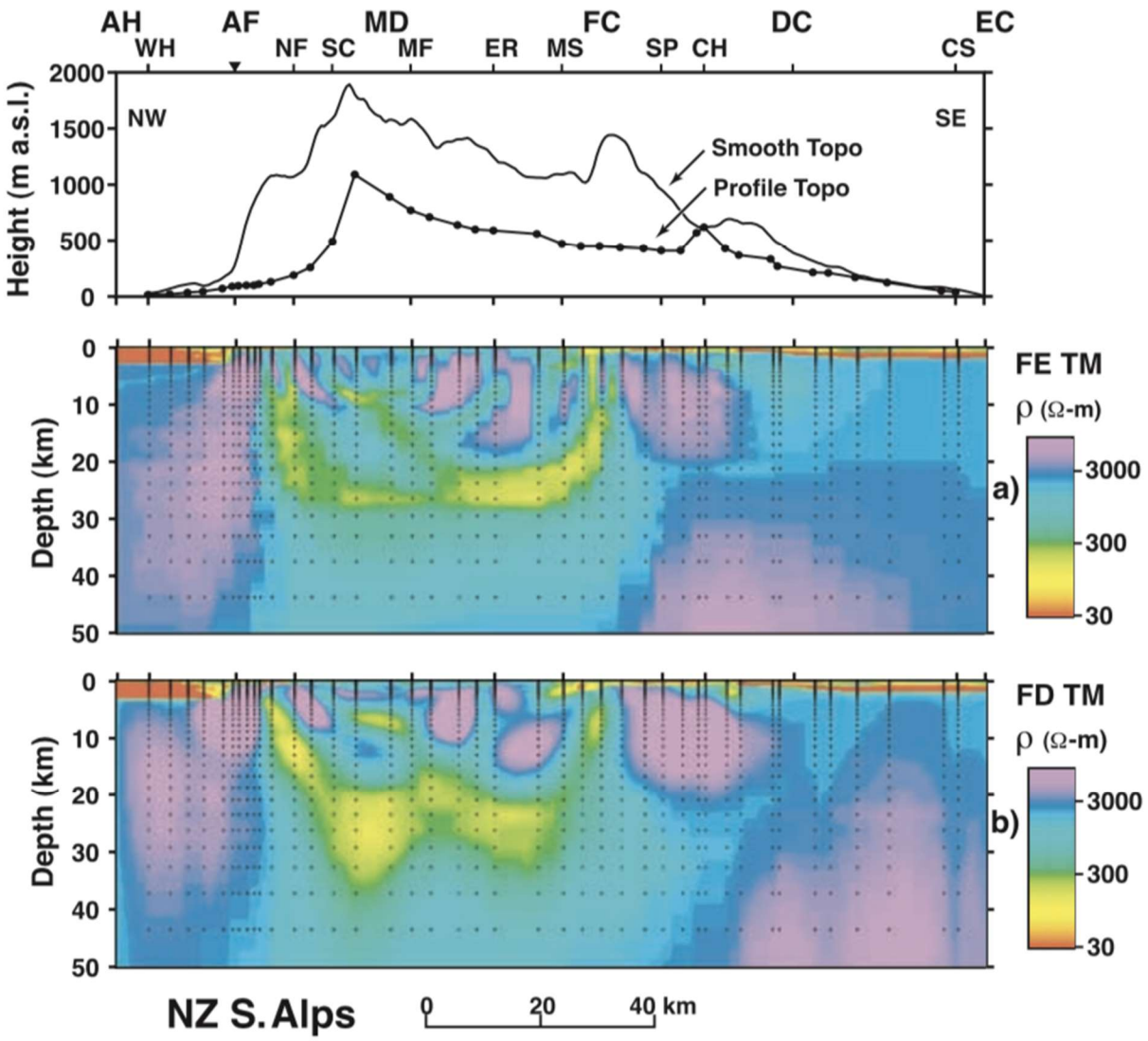

Figure 4.4: Resistivity models derived from the MT data from the New Zealand South Island Transect. The top panel is the topography across the transect. The middle panel is the inversion model based off a finite element algorithm. The bottom panel is an inversion model based off a finite difference algorithm (Wannamaker, et. al., 2002).

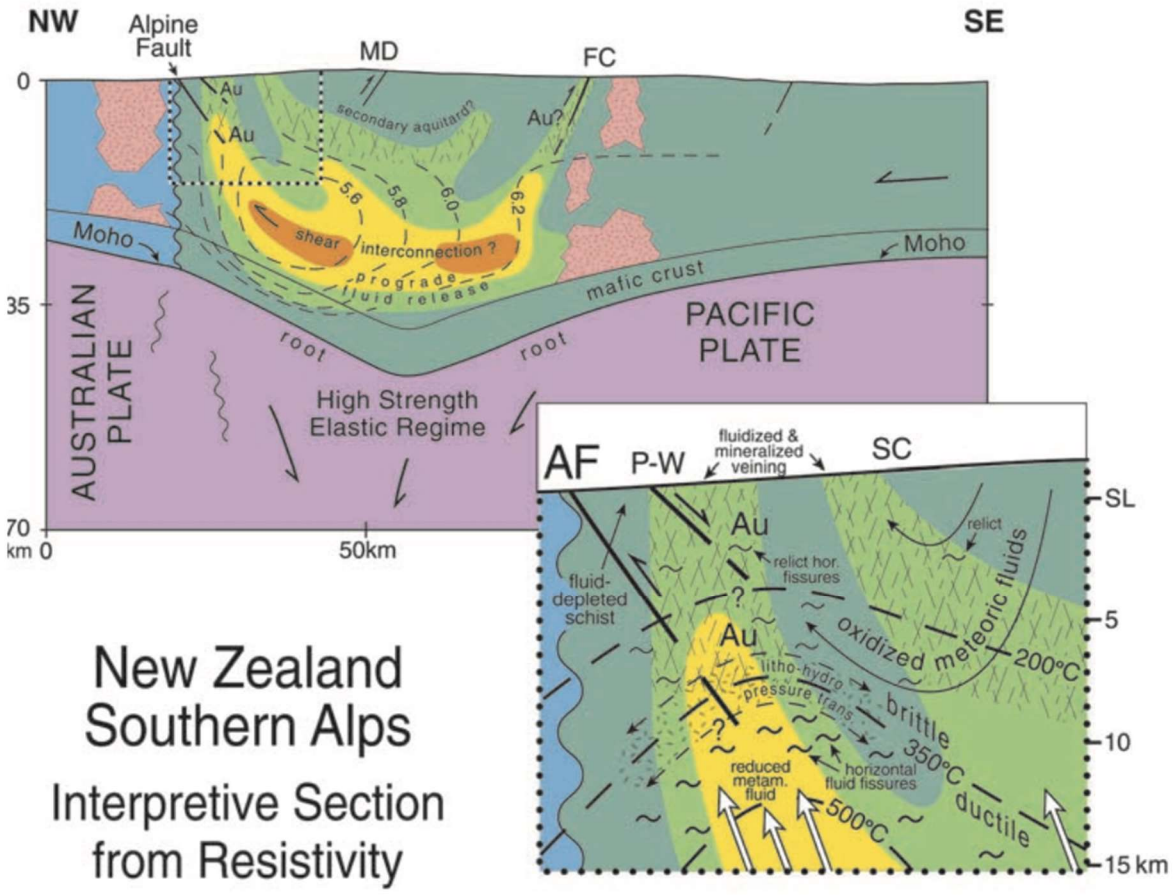

Figure 4.5: Geologic section interpreted from the resistivity section and other constraints. The solid shading represents low resistivity (high conductivity) (Wannamaker, et. al., 2002).

4.3 Teleseismic Receiver Function Methods

Another tool for inferring crustal and mantle structure is receiver functions, which are sensitive to both depth and velocity. H-k stacking of receiver functions was used by Spasojević and Clayton (2005) to determine crustal properties of the South Island. In this study, 42 stations were used with more than 700 receiver functions. Figure 4.6 outlines the receiver function quality. Good stations, in green, have a high coherence, good quality stack and many usable receiver functions. Poor stations in red, have fewer than five receiver functions where the conversion is at different times, resulting in a poor stack

(Spasojević and Clayton, 2005). There are many poor stations that lie right on the Alpine Fault, which is mostly likely due to a more complicated crustal structure below the station.

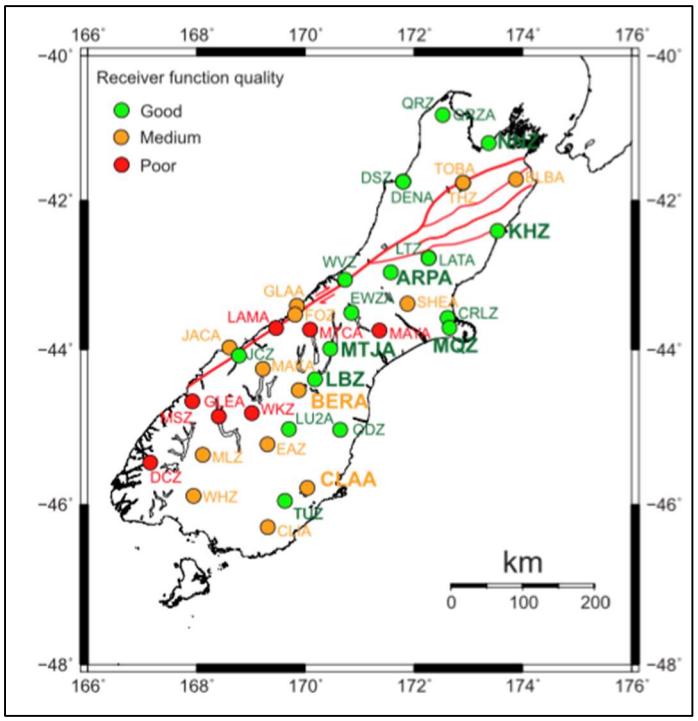

Figure 4.6. Receiver function quality of stations in case study: South Island, New Zealand (Spasojević and Clayton, 2005).

Crustal thickness estimates vary from 21 km to 56 km. The thinnest crust is located on the Pacific Plate, on the east coast of the South Island, around 25 km. Crustal thickness increases towards the centre of the island. The thickest crust is 56 km (denoted by the A in Figure 4.7), where the Alpine Fault splays into multiple major faults.

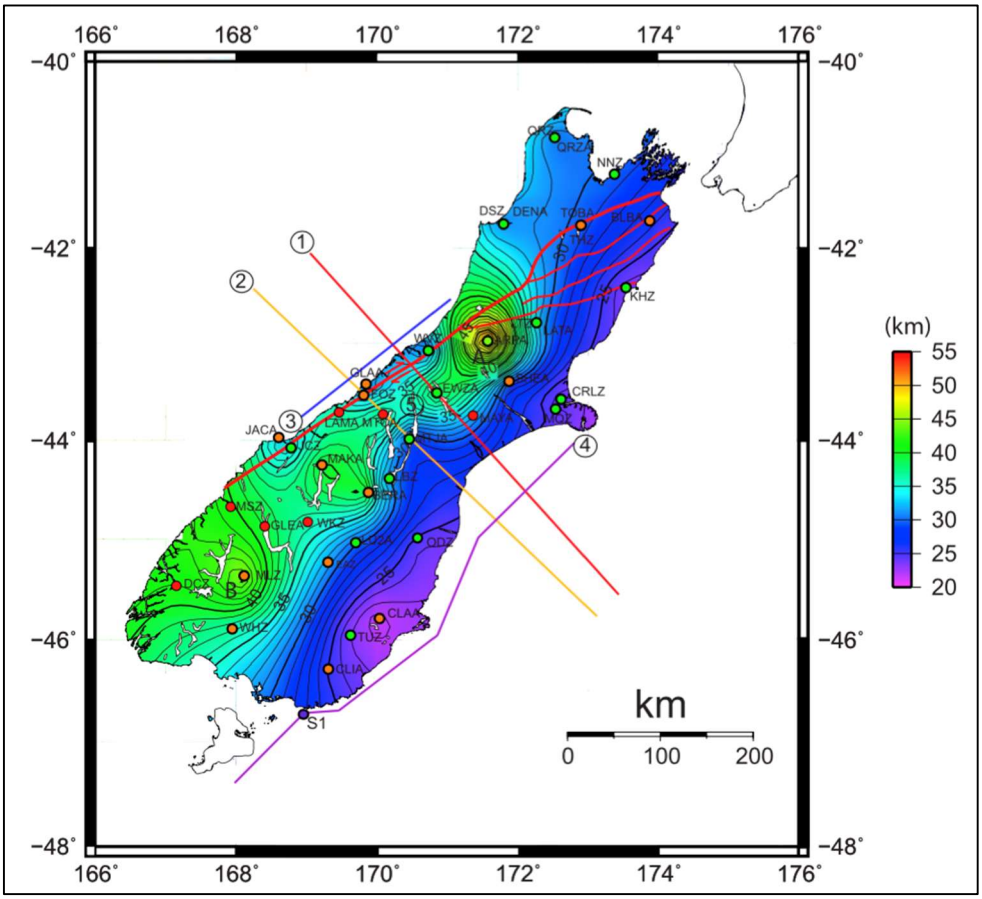

Figure 4.7. Crustal thickness with the stations' colour coded by station quality (Spasojević and Clayton, 2005).

Spasojević and Clayton, 2005 suggest two possible theories for the thicker crust on the one side of the fault: i. tectonic underplating of oceanic crust created by the spreading of the Pacific and Australian plates. The crust has been split from the Australian plate, and over time has been extended over and underplated under the South Island. ii. Paleosubduction on the Gondwanaland margin in the South Island.

In this experiment the H-k stacking method will be employed, to validate against the Spasojević and Clayton, (2005) results and create a basis for using the transfer function method to improve on these results, especially in areas of poor receiver function quality. Both the H-k

stacking method and the transfer function method will be used with a similar set of stations and events. The results of both methods can be mapped and compared spatially with this published study. Where there are common stations, a more direct comparison can be completed.

4.4 Reflection and Refraction Studies

There has been significant work in the South Island, New Zealand that has contributed to results for crustal thickness and Vp/Vs ratio. Methods include wide angle reflection, refraction and tomography. Wide angle reflection and refraction surveys are useful at determining velocity vs depth (but resolution is poor laterally) and reflection has a velocity/depth trade-off (but resolution is higher laterally) (Lowrie, 2007). In addition, seismic tomography is mostly used for generating velocity models of the subsurface.

Inversions of seismic refraction data allow constraints on deep structure of the South Island. A seismic refraction study done by Van Avendonk *et al.,* (2004), generated seismic velocity models with a multi-layer crust covering the Pacific and Australian plates. This study included data from the 1996 South Island Geophysical Transect (SIGHT) active source seismic survey, which comprised of two transects across the South Island as shown in Figure 4.8. Tomographic inversion was performed using crustal and upper mantle refractions, along with wide-angle reflection travel times recorded along Transect 1.

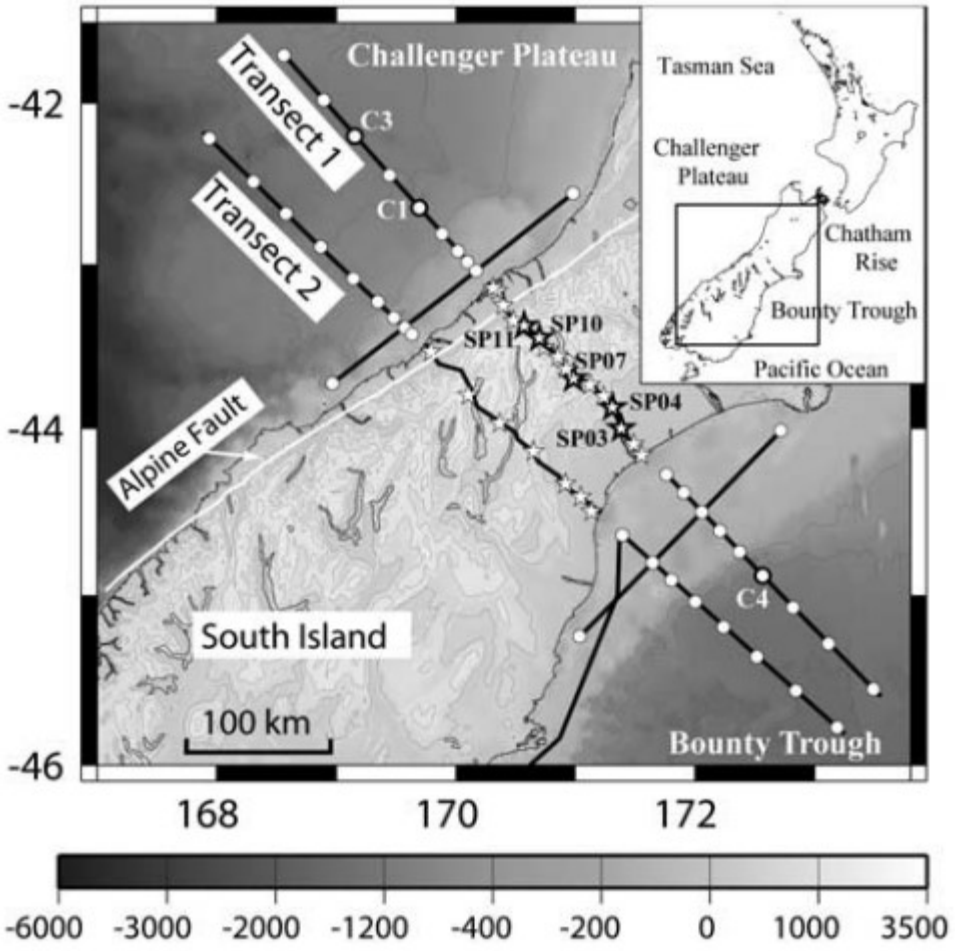

Figure 4.8: SIGHT refraction surveyed completed over two transects spanning 150 km across central New Zealand. A tomographic inversion completed by Van Avendonk et al., (2004) generated a crustal model over Transect 1.

The final seismic velocity model is shown in Figure 4.9. In summary, the model included multiple layers described below (Van Avendonk *et al.,* 2004):

1. Upper crust is 15-30 km thick with seismic velocities of 5.7 – 6.2 km/s.
2. Lower crustal thickness and seismic velocity ranging between 2 – 6 km and 6.5 – 7.1 km/s respectively.
3. Mantle velocities varying between 8 – 8.6 km/s.

This model will help assign necessary constraints on the deep structure of South Island, New Zealand and more specifically, a comparison to the structure on this transect can be completed.

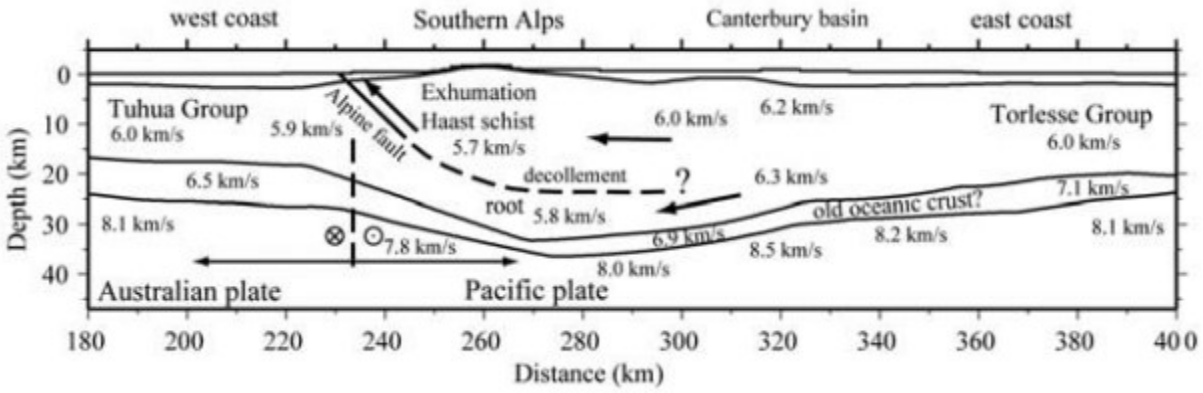

Figure 4.9: Seismic velocity model across Transect 1 from tomographic inversion completed by Van Avendonk et al., (2004).

Eberhart-Phillips and Bannister, (2010) have developed 3-D seismic velocity models for most of New Zealand using local earthquake data collected by the GeoNet seismograph network (Figure 4.10). The method used in this study is travel-time tomography for both P and S waves.

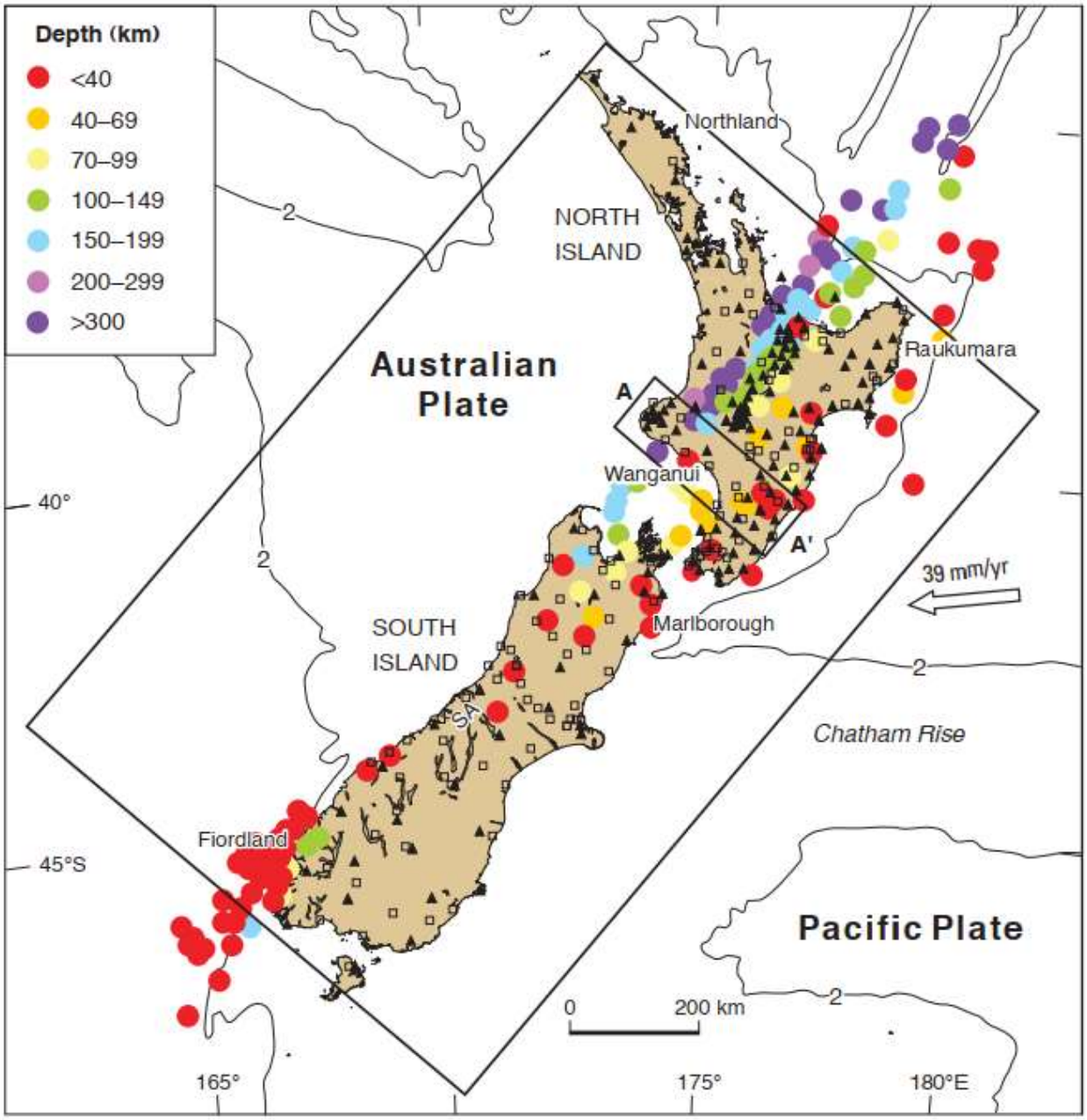

Figure 4.10: Earthquakes with M >5 during 2001-2009 (coloured by depth) are denoted as circles and stations are denoted as triangles (GeoNet seismograph stations) and squares (GeoNet strong-motion stations) (Eberhart-Phillips and Bannister, 2010).

Vp and Vp/Vs models are presented for different depth slices, as presented in Figure 4.11 at 38 and 65 km (Eberhart-Phillips and Bannister, 2010). For example, low Vp and high Vp/Vs can be seen in the 65 km depth slice from the Hikurangi slab in the North Island (Eberhart-Phillips and Bannister, 2010). In the South Island, the high velocity mantle appears to be bounded at this

depth slice and deepens toward the Fjordland subduction interface. Seismic tomography and other studies will be helpful to determine upper and lower bounds of Vp/Vs ratios that are reasonable for the South Island (Eberhart-Phillips and Bannister, 2010).

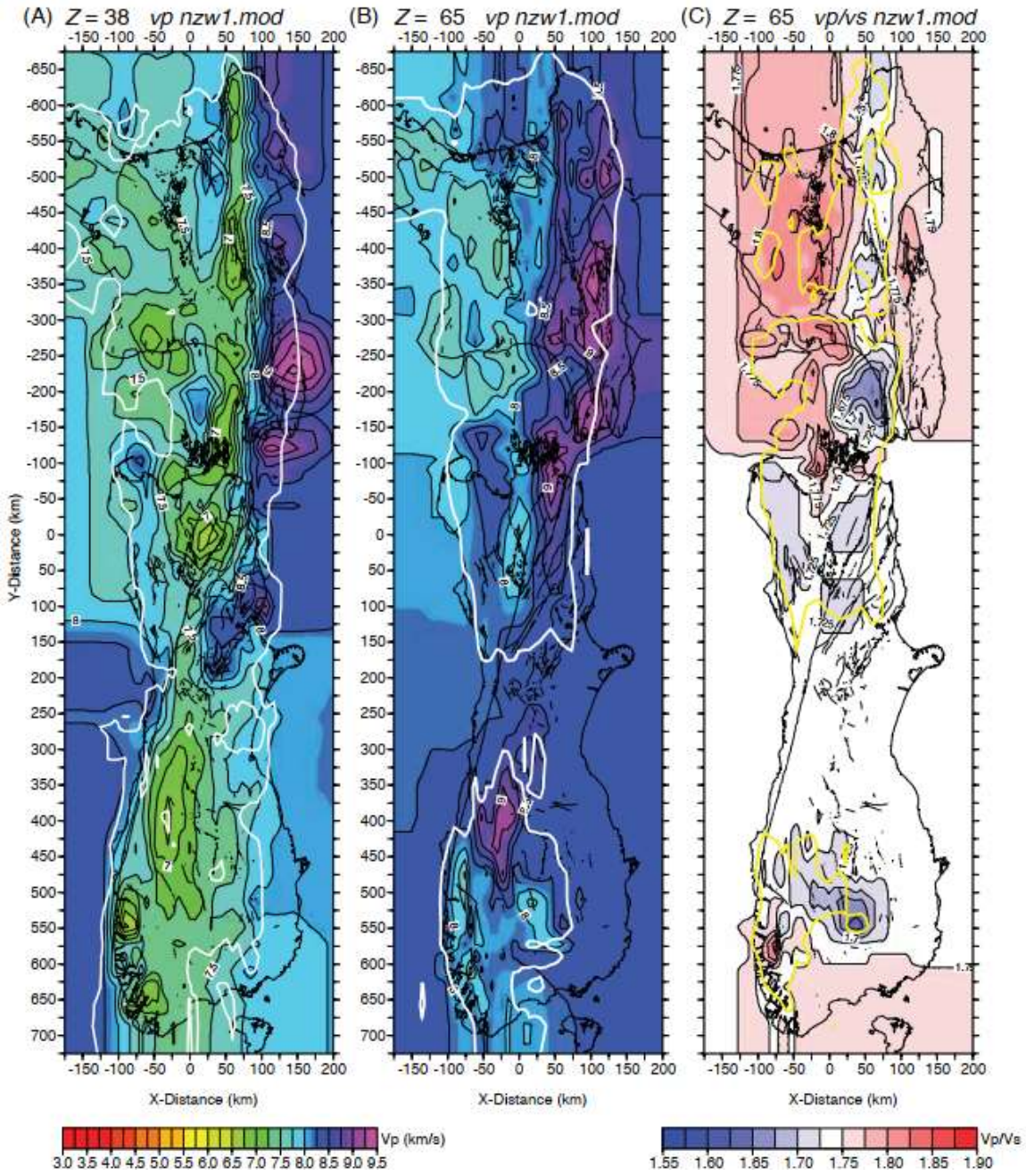

Figure 4.11: LEFT: P wave velocity at 38 km depth slice. MIDDLE: P wave velocity at 65 km depth slice. RIGHT: Vp/Vs ratio at 65 km depth slice (Eberhart-Phillips and Bannister, 2010).

4.5 Compilation of Seismic Methods

The definition of the Moho is difficult in New Zealand, as the mantle velocities can vary significantly due to subduction, some areas are underplated, and the plate interfaces cause ambiguity between overriding and subducting plates (Salmon *et al.,* 2013). Using multiple seismic methods works as a good strategy to help overcome difficulties in defining the Moho. A compilation of seismological data (receiver functions, wide angle reflection, tomography and traditional marine reflection) has been presented by Salmon *et al.,* (2013) for depth to Moho beneath New Zealand in Figure 4.12. Three areas of thickened crust can be seen. Firstly, between the North and South Islands in the Wanganui Basin. Secondly, along the centre of the South Island in the Southern Alps. Thirdly, in the southwest corner of the Puysegur subduction zone in the Fjordland. The Wanganui Basin is in an area where the boundaries of the plates transition from oblique subduction to multiple-strand strike slip faulting. The thicker crust seen in the basin can be characterized by the deep basin and the downward deformation of the topography due to the combined effect of subduction pull and convergence accommodation. The Fjordland is at the edge of the transition from subduction to oblique strike slip, and shows a deep Moho at approximately 40 km. Here the topography is higher than the basin and the position of the Moho in this region is uncertain due to the plate interface. In the Southern Alps, the depth to Moho reaches 42 km, which is 17 km greater than the depth to Moho at the coast. The highest elevations are in the centre of the Southern Alps, and the crustal root is nearly twice as large to support the elevation. The thickest crust of 48 km in the South Island is found in the Wanaka region. The Wanaka region is 100 km south of the centre of the Southern Alps (Salmon, *et al.,* 2013).

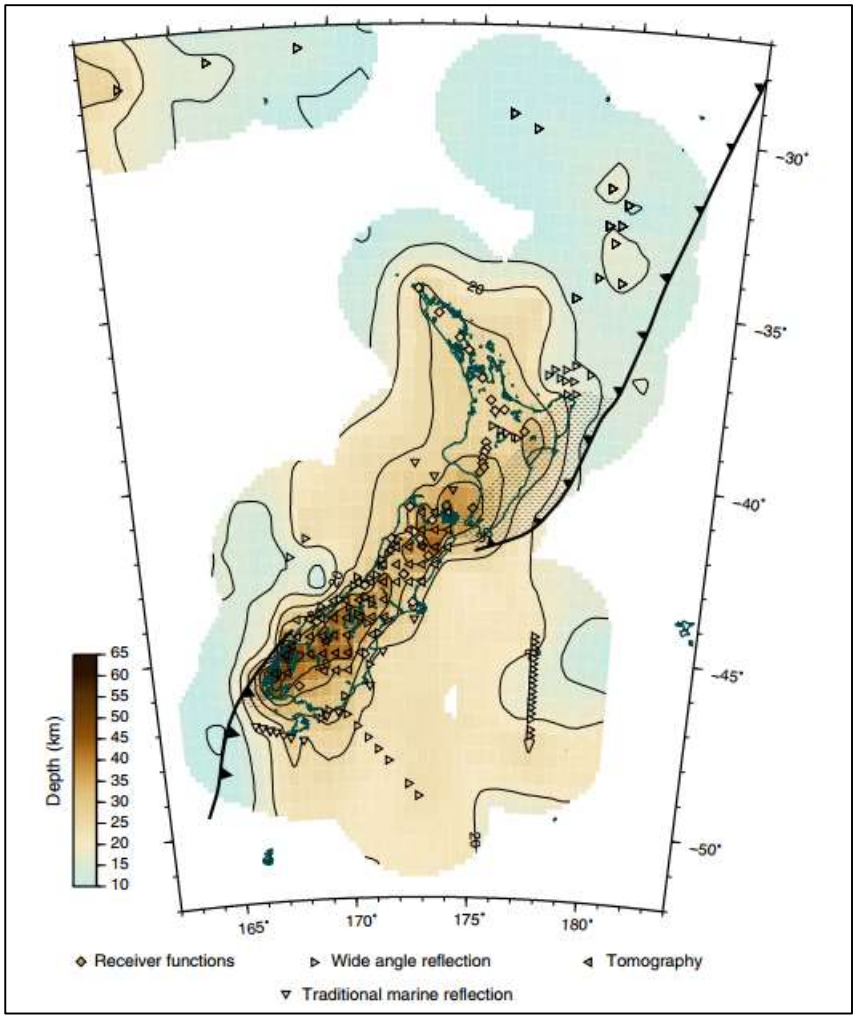

Figure 4.12. Depth to Moho over New Zealand from various seismic methods. Icons are color coded for Moho depth and contoured with subduction zones superimposed (Salmon, et al., 2013).

5 Data Selection and Inspection

5.1 Data Selection

The data for this experiment were retrieved for 32 broadband three-component seismometers from the New Zealand National Seismograph Network (Petersen *et. al.,* 2011). Table 5.1 lists the total number of stations and their respective locations. Events of magnitude M > 6, recorded from 1990 to 2015 were chosen. To be considered as teleseismic, events located between 30 – 100° from the centre of the array were used. Any closer or farther and the P wave becomes complicated or absent due to interactions within the upper mantle, and the core's shadow zone respectively. The 27 seismometers and 2469 events are outlined in Figure 5.1.

Preprocessing of the data included using a script to download the SAC traces from the GNS Science archives which were then subsequently sorted into directories based on the date the earthquake was recorded. After the data were sorted into their respective event folders, a Unix shell script was run to determine if broadband data were present for each station and event. If broadband data were available, the traces were copied to new files with event information added to the headers such as date, time, event location, back azimuth, ray parameters, and predicted travel times. The ray parameters and predicted travel times were calculated using the TauP Toolkit and the IASP91 earth model (Crotwell *et.al*., 1999; Kennett, 1991). Each north-south, east-west, and vertical seismic trace was trimmed to a 120 s window, 30 s before and 150 s after the predicted arrival times. The north-south and east-west traces were then rotated about the vertical axis to radial and transverse traces respectively, so that the radial traces are parallel to the back azimuth and the transverse traces are perpendicular to the back azimuth. Only the radial and vertical traces were used in this study.

Table 5.1. Station ID, locations and date of installation.

Station ID	Longitude	Latitude	Date
SYZ	169.14	-46.54	06-05-05
PYZ	166.68	-46.17	07-05-01
TUZ	169.63	-45.95	91-04-04
WHZ	167.95	-45.89	93-03-22
OPZ	170.6	-45.88	08-06-26
DCZ	167.15	-45.46	91-05-28
MLZ	168.12	-45.37	96-03-09
EAZ	169.31	-45.23	04-11-01
ODZ	170.64	-45.04	90-08-31
WKZ	169.02	-44.83	04-06-03
MSZ	167.93	-44.67	66-03-03
LBZ	170.18	-44.39	04-06-04
CVZ	171.01	-44.38	13-06-01
JCZ	168.79	-44.07	04-06-23
RPZ	171.05	-43.71	01-06-06
MQZ	172.65	-43.71	89-10-13
FOZ	169.82	-43.53	04-10-13
OXZ	172.04	-43.33	09-03-14
WVZ	170.74	-43.07	90-05-16
GVZ	173.03	-42.97	13-01-26
LTZ	172.27	-42.78	89-10-12
INZ	171.44	-42.72	11-01-26
KHZ	173.54	-42.42	88-12-08
THZ	172.91	-41.76	89-12-02
DSZ	171.8	-41.74	90-02-18
NNZ	173.38	-41.22	03-08-12
QRZ	172.53	-40.83	90-04-26

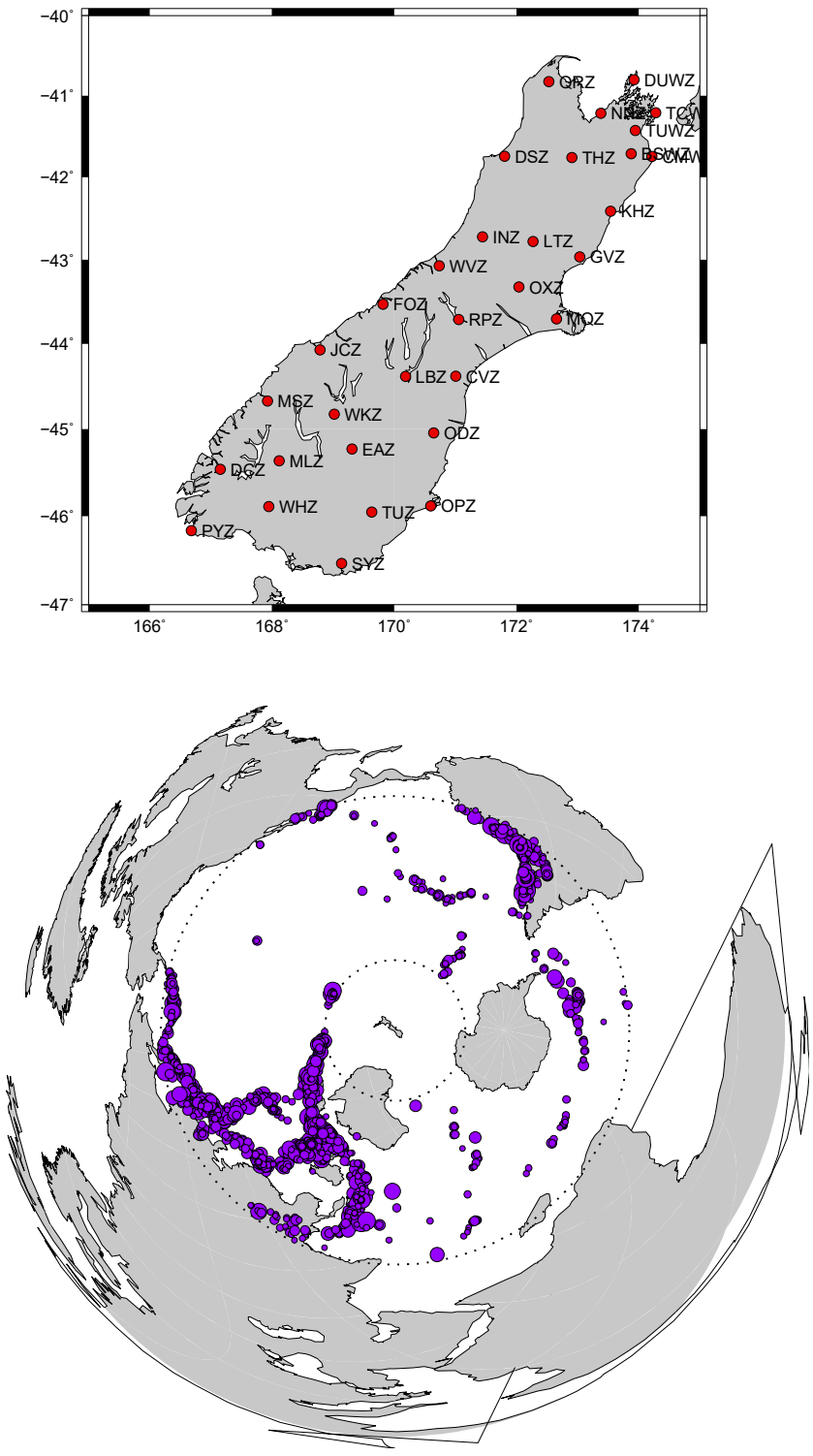

Figure 5.1. Top: Map of all 32 broadband three-component seismometers. KHZ is located in the northeast and DCZ is located in the southwest of the island. Bottom: All earthquakes used between 30 – 100° from the centre of array.

5.2 Data Inspection

The data analysis process was completed in two phases, the data quality control phase and the receiver function quality control phase. Before the radial and vertical traces were used in computations, the data quality control phase was performed. The traces were first passed through a Butterworth filter with a passband range of 0.3 – 3 Hz and displayed for a time band relative to the expected P arrival (-15 – 45 s). The radial traces were then examined to ensure that the P arrival was prominent and the signal to noise ratio was acceptable (Figure 5.2). Vertical traces were examined to guarantee that the source time function could be approximated adequately (the trace was examined to see whether the P arrival was a relatively short pulse). Traces that were too noisy or for which travel times could not be identified clearly were marked as 'BAD' and were not used in the receiver function analysis.

The traces that were not marked as 'BAD' in the preceding phase, went forward into the receiver function quality control phase. The radial and vertical components that were considered 'acceptable' were used in the deconvolution algorithm (Equation 2.8), using a damping factor of 0.01. Subsequent to deconvolution the data were passed through another Butterworth filer with a passband range of 0.02 – 2 Hz. The resulting receiver functions from the deconvolution process were then displayed in a time band relative to the expected P arrival (-15 – 45 s). The receiver functions that had the P travel time centered or close to zero and a Ps arrival (Moho conversion) at approximately 5 s, proceeded to be used in the H-k stacking method (Figure 5.3). The ones that did not meet those criteria were also marked as 'BAD' and were left unused.

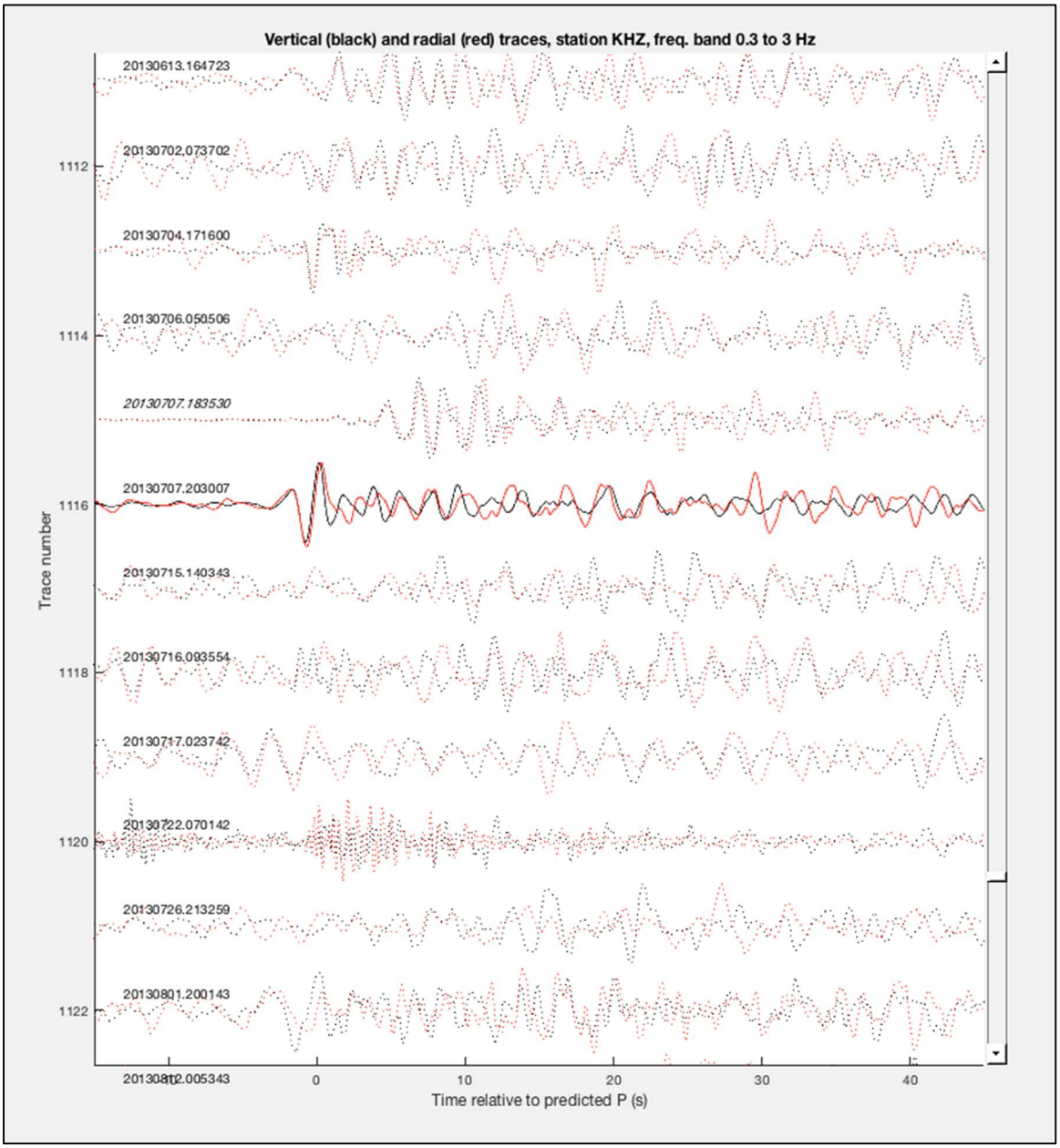

Figure 5.2. Data quality control phase for station KHZ vertical and radial components (black and red respectively). Traces that are displayed as solid traces have acceptable signal to noise ratio and the dotted traces are treated as "BAD", and therefore not used in receiver function analysis.

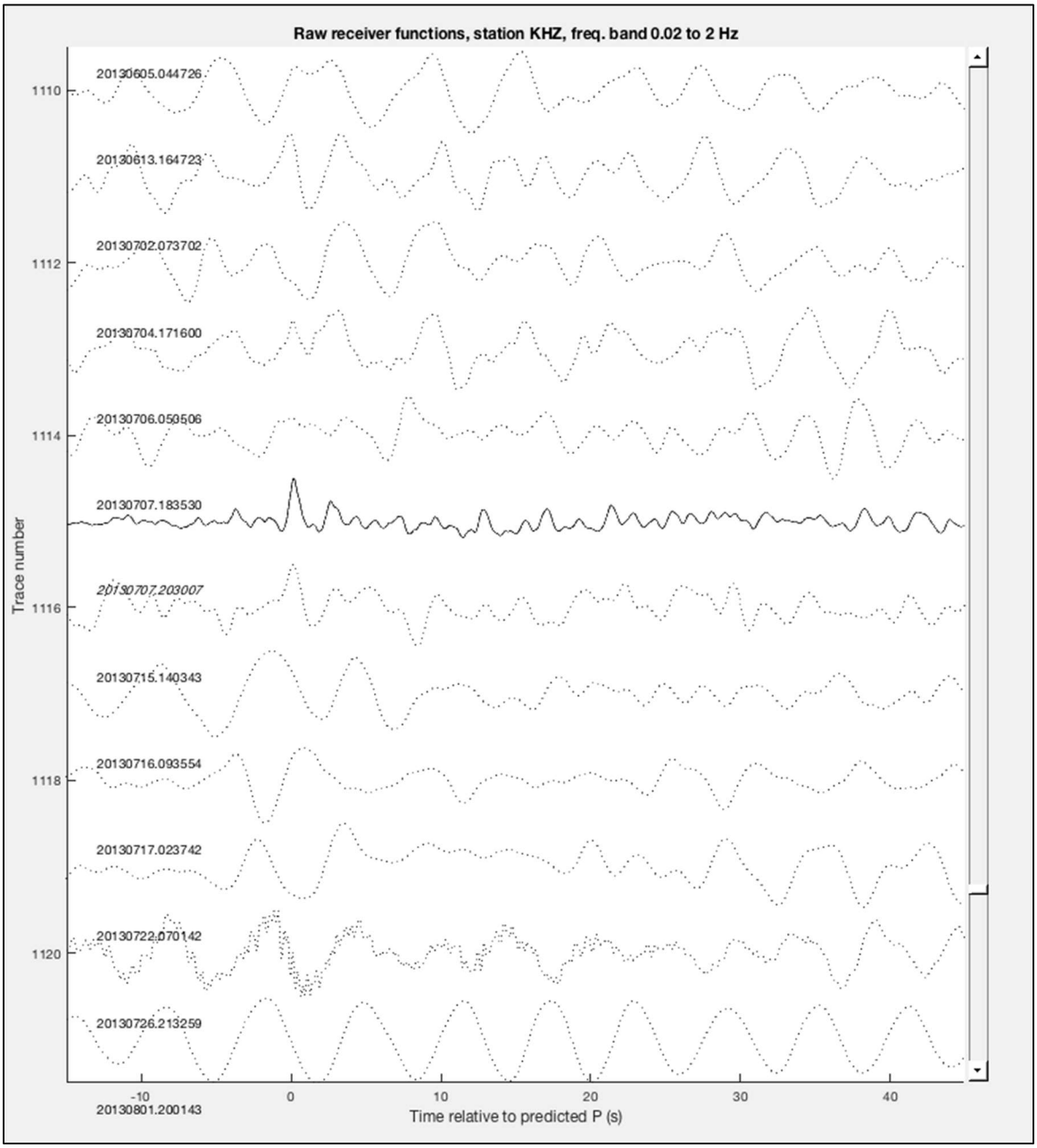

Figure 5.3. Receiver function quality control phase for station KHZ. The receiver function for a given even that has the P travel time centered close to zero and Ps travel time close to 5 s will be used in the nth-root stacking method. However, the receiver functions indicated by dotted and faded lines will be marked as "BAD" and not used in receiver function analysis.

6 Results

6.1 H-K stacking

Traces that passed the quality control phases were input into a receiver function deconvolution algorithm, followed by a Zhu and Kanamori (2000) H-k style-stacking algorithm. The source time function of each earthquake is obtained by extracting the P wave from the vertical component. It is then used to deconvolve the waveforms using Equation 2.8 with a damping factor of 0.001. The receiver functions are put through a Butterworth filter with a passband range of 0.2 – 2 Hz and then stacked using Equation 2.12, with $w_1 = 0.5$, $w_2 = 0.25$, and $w_3 = 0.25$. These values are chosen to balance the contributions from each phase. The highest weighting is given to the Ps conversion because it has a higher signal to noise ratio than the other two phases. All stacking is completed assuming an average crustal P velocity of 6.3 km/s.

In total, 27 estimations of crustal thickness and Vp/Vs were completed. The results for the crustal thicknesses and the Vp/Vs ratios are listed in Table 6.1. Crustal thickness and Vp/Vs values range from 20-54.4 km and 1.55-1.85 with an average of 31.5 km and 1.7, respectively. These results were then plotted and contoured as shown in Figure 6.1. Thicker crust is seen near the Westland Basin along the southwestern end of the Alpine Fault and near the southwest side of the island (see Chapter 3 for geological map). Thinner crust is seen in the Canterbury basin and adjacent to the thicker crust on the southwest side of the island. Higher values of Vp/Vs ratio are seen near the Westland Basin along the centre of the Alpine Fault and in the northwestern end of the Canterbury basin. Lower values of Vp/Vs ratio are observed along the southwestern end of the Alpine Fault and the Otago Schist.

Table 6.1: H-k stacking results over the South Island, New Zealand.

Station	Longitude	Latitude	Thickness (km)	Vp/Vs	Number of Receiver Functions
SYZ	169.14	-46.54	20.6	1.65	51
PYZ	166.68	-46.17	54.4	1.67	33
TUZ	169.63	-45.95	22.8	1.71	153
WHZ	167.95	-45.89	42.8	1.67	29
OPZ	170.6	-45.88	39	1.56	84
DCZ	167.15	-45.46	20	1.59	106
MLZ	168.12	-45.37	44.6	1.72	62
EAZ	169.31	-45.23	34.2	1.57	85
ODZ	170.64	-45.04	28.4	1.63	90
WKZ	169.02	-44.83	36	1.73	17
MSZ	167.93	-44.67	26.6	1.55	38
LBZ	170.18	-44.39	38	1.57	64
CVZ	171.01	-44.38	26.4	1.72	13
JCZ	168.79	-44.07	43.4	1.58	67
RPZ	171.05	-43.71	25.2	1.67	45
MQZ	172.65	-43.71	25.8	1.73	131
FOZ	169.82	-43.53	50	1.83	52
OXZ	172.04	-43.33	23.6	1.84	40
WVZ	170.74	-43.07	20	1.82	45
GVZ	173.03	-42.97	20.8	1.85	37
LTZ	172.27	-42.78	32.4	1.83	43
INZ	171.44	-42.72	32.2	1.78	24
KHZ	173.54	-42.42	21.6	1.69	50
THZ	172.91	-41.76	22.6	1.68	93
DSZ	171.8	-41.74	39.2	1.63	54
NNZ	173.38	-41.22	29.2	1.85	149
QRZ	172.53	-40.83	30.6	1.71	71

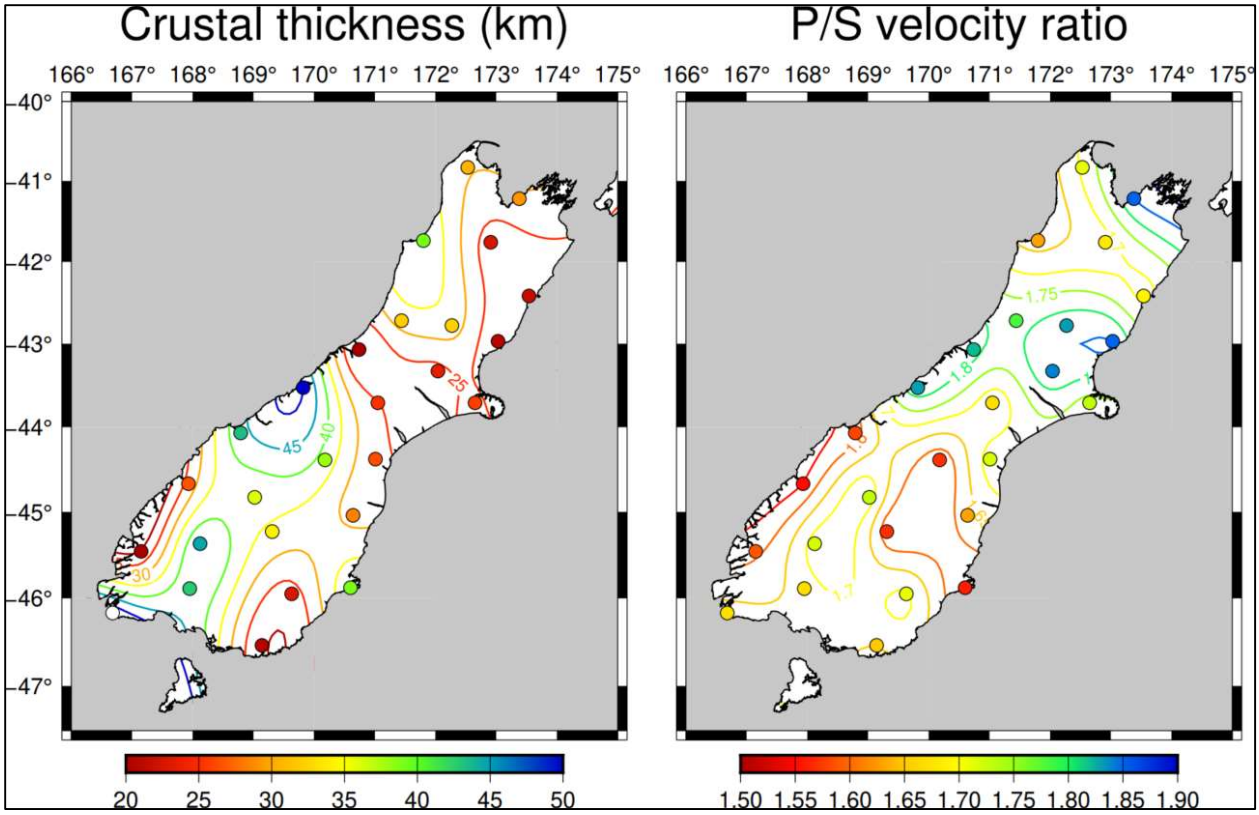

Figure 6.1: Crustal thickness and Vp/Vs variation across the South Island, New Zealand from H-k stacking of receiver function using simultaneous deconvolution.

Zhu and Kanamori (2000) suggest that measurements calculated directly from stacking receiver functions are more robust than estimates obtained just using the Ps and PpPs conversions. The later phase, which takes a longer ray path through the crust than the primary conversion and has an extra reflection on the surface, is much more sensitive to lateral structural variations. Dipping Moho or surface topography is a good example of this, where a small dip angle (5°) can change the arrival time of the PpPs phase by 3 s depending on if the incoming wave in propagating in the updip or downdip directions. The effects of lateral variations are significantly reduced from the Zhu and Kanamori (2000) style algorithm using receiver functions from different directions and distances.

As an example, estimations of crustal thickness and Vp/Vs values were completed for stations KHZ and DCZ (determined to be good and poor stations respectively, based on receiver function quality from Spasojević and Clayton, 2005). KHZ is located in the northeast of the island. Stacking of 50 receiver functions at station KHZ gives a crustal thickness of 21.6 km with a Vp/Vs ratio of 1.69 (Figure 6.2). DCZ is located in the southwest of the island, with a slightly later Ps conversion resulting in a lower crustal thickness value. Stacking of 106 receiver functions at station DCZ yields a crustal thickness of 20 km with a Vp/Vs ratio of 1.59 (Figure 6.3). The results from both stations have multiple local maxima, therefore causing some uncertainty with the estimates of Vp/Vs. This could be due to other coherent phases after the Moho Ps in the receiver functions used for station KHZ and DCZ. The source could be Ps conversions from upper mantle discontinuities, or they may be multiples of intracrustal conversions (Zhu and Kanamori, 2000). In general, these phases have a different moveout with ray parameter then those from the Moho PpPs and PpSs so that the energy will not stack out coherently. A consequence of these phases is that they often smear the S(H, k) maximum and cause other maxima to occur. In the case of multiple peaks on S(H, k), information on crustal thickness and Vp/Vs ratio from nearby stations may be used to resolve this ambiguity (Zhu and Kanamori, 2000).

Spasojević and Clayton (2005) performed the H-k stacking method using similar parameters on station KHZ and DCZ, therefore the results can be compared directly (Figure 6.4). 39 receiver functions were stacked to result in a crustal thickness of 23.4 km and a Vp/Vs of 1.733 for KHZ. Unfortunately, according to Spasojević and Clayton, 2005's criterion, only 1 receiver function was usable for DCZ. Therefore, no crustal thicknesses were calculated for this station. However, according to the crustal thickness contour map shown in the previous section

(Figure 4.4), DCZ is located in an area of increased thickness (approximately 40 km from surrounding stations). The variation in calculations is most likely due to uncertainty resulting from multiple maxima shown in Figure 6.2 and Figure 6.3.

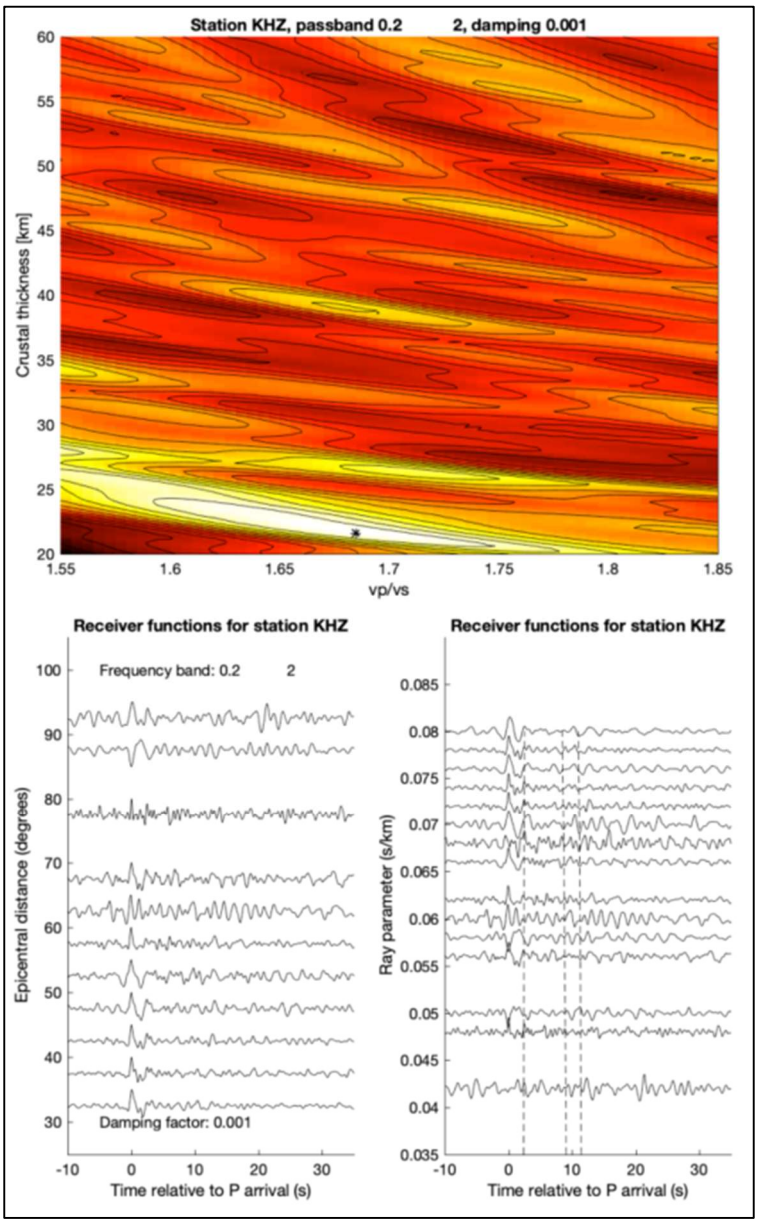

Figure 6.2. The S(H,k) for station KHZ. The H-k stacking method estimates a crustal thickness of 21.6 km with a Vp/Vs ratio of 1.69. The top panel shows the convergence towards the most likely solution where a maximum of S(H,k) is reached. The bottom panel is the final stacked receiver functions, based on ray parameter or epicentral distance.

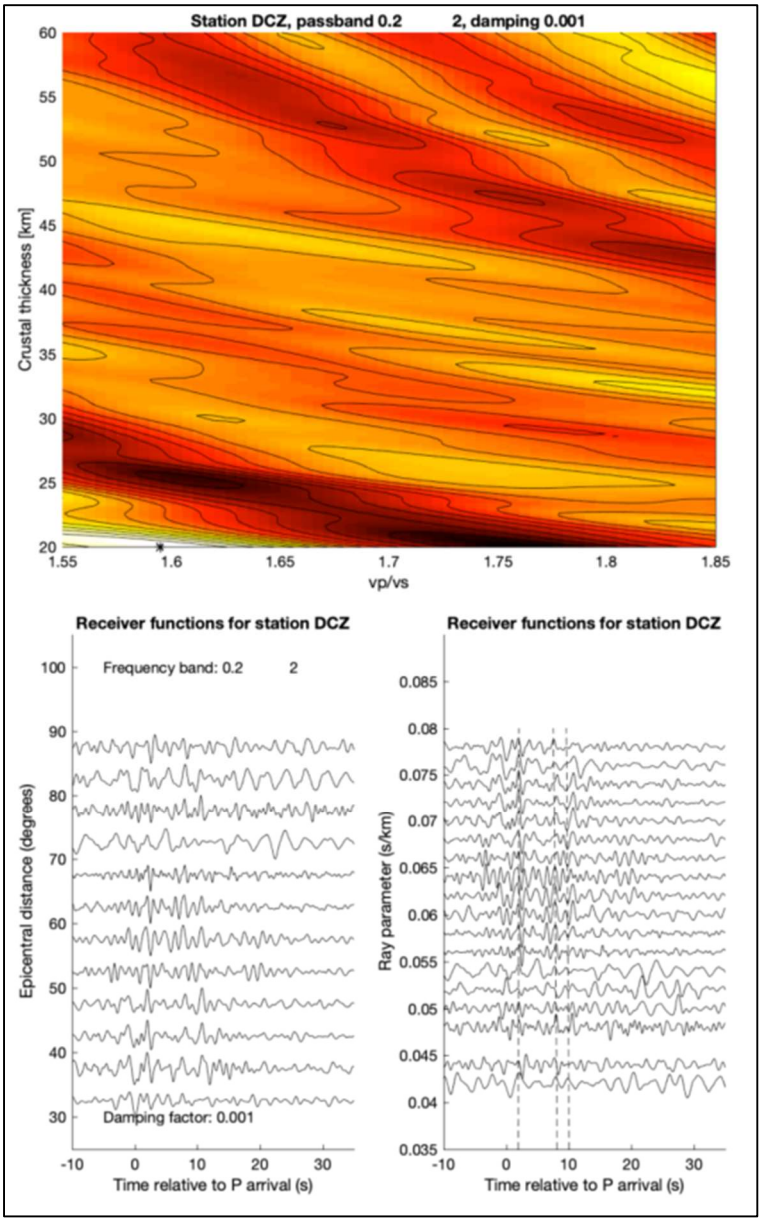

Figure 6.3. The S(H,k) for station DCZ. The H-k stacking method estimates a crustal thickness of 20 km with a Vp/Vs ratio of 1.59. The top panel shows the convergence towards the most likely solution where a maximum of S(H,k) is reached. The bottom panel is the stacked receiver functions, based on ray parameter or epicentral distance.

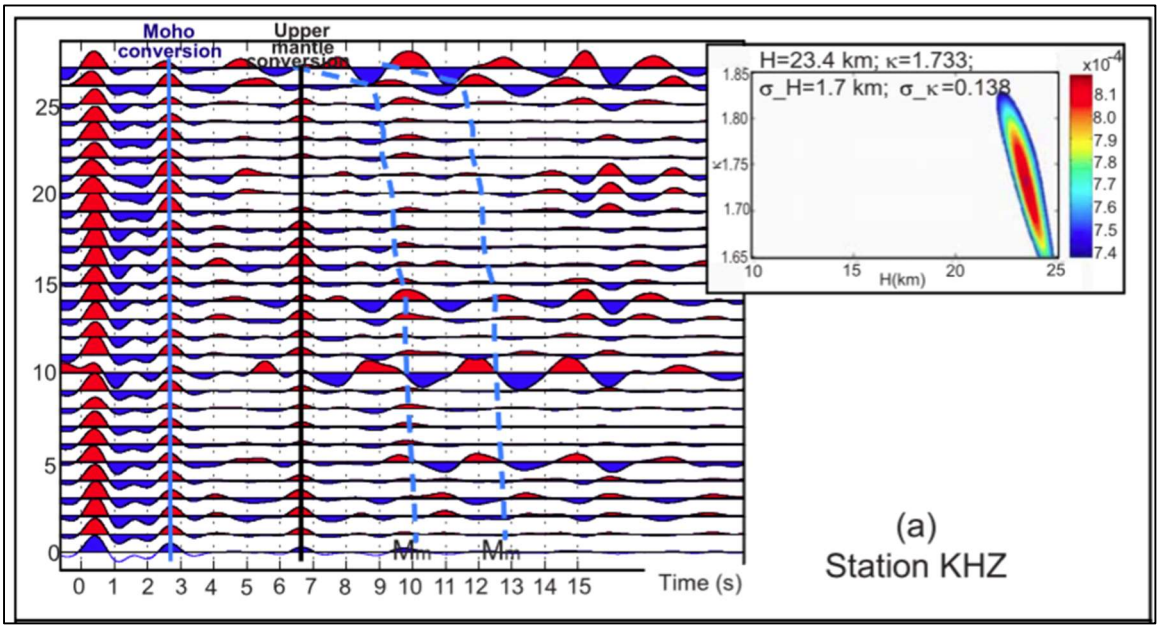

Figure 6.4. Results of H-k stacking at station KHZ from Spasojević and Clayton, 2005.

In general, the results for stations KHZ and DCZ calculated from this study are considered to be of low quality. This poor resolution is most likely due to low signal to noise ratio and complicated site responses. New Zealand is naturally a seismically noisy environment and the geology of the crust cannot be treated as a one layer structure. In addition, during the quality control phase, most of the events analyzed showed the P arrival appearing slightly off from time zero. This is indicative of a sedimentary layer being present under the station (Lowe and Cassidy, 1995). Using the transfer function approach will be more suitable for noisy study areas and will be able to account for any sedimentary layer present.

6.2 Transfer-function (grid search)

In addition to the H-k stacking method, the transfer function method using a grid search was conducted with the following parameters for the one-layer and two-layer models as provided in Table 6.2. These parameters are similar to Spasojević and Clayton (2005) to see if the results were comparable.

Table 6.2: Parameters for one-layer and two-layer models used in the transfer function grid search.

One-layer catalogue parameters

Parameter	*Range*	*Increment*
Thickness	20-55 km	0.5 km
Vp/Vs	1.6-1.9	0.02
Ray parameter	0-0.1 s/km	0.002 s/km

Two-layer catalogue parameters

Parameter	*Range*	*Increment*
Sedimentary layer thickness	100, 500, 1000, 1500, 2000, 2500 m	N/A
Crustal thickness	20-55 km	0.5 km
Vp/Vs	1.6-1.9	0.02
Ray parameter	0-0.1 s/km	0.002 s/km

Fixed parameters

Parameter	*Constant*
Sedimentary P velocity	2600 m/s
Sedimentary S velocity	1300 m/s
Sedimentary density	2.2 g/cm
Crustal P velocity	6300 m/s
Crustal density	2.5 g/cm
Mantle P velocity	8040 m/s
Mantle S velocity	4480 m/s
Mantle density	3.6 g/cm

Figure 6.5 shows the results for KHZ. One-layer models and two-layer models were used to calculate the theoretical radial components. As mentioned previously, the model with the lowest misfit between the theoretical radial component and the real radial component is our solution. As an alternative metric, the correlation coefficient was examined between the true and predicted radial traces; the correlation metric will be less sensitive to amplitude variations, and so may perform better when the radial amplitude is altered by near-surface conditions.

For the one-layer model, a crustal thickness of 34.5 +/- 1.25 km and a Vp/Vs of 1.9 +/- 0.05 was

calculated. As shown in the grid on the left there are multiple low misfits. For the two-layer model, a crustal thickness of 29 +/- 1.25 km, sedimentary thickness of 2.5 km and a Vp/Vs of 1.9 +/- 0.01. The two-layer model seems to also have two low misfit results. In addition, these crustal thicknesses are generally higher than the results from the H-k stacking method.

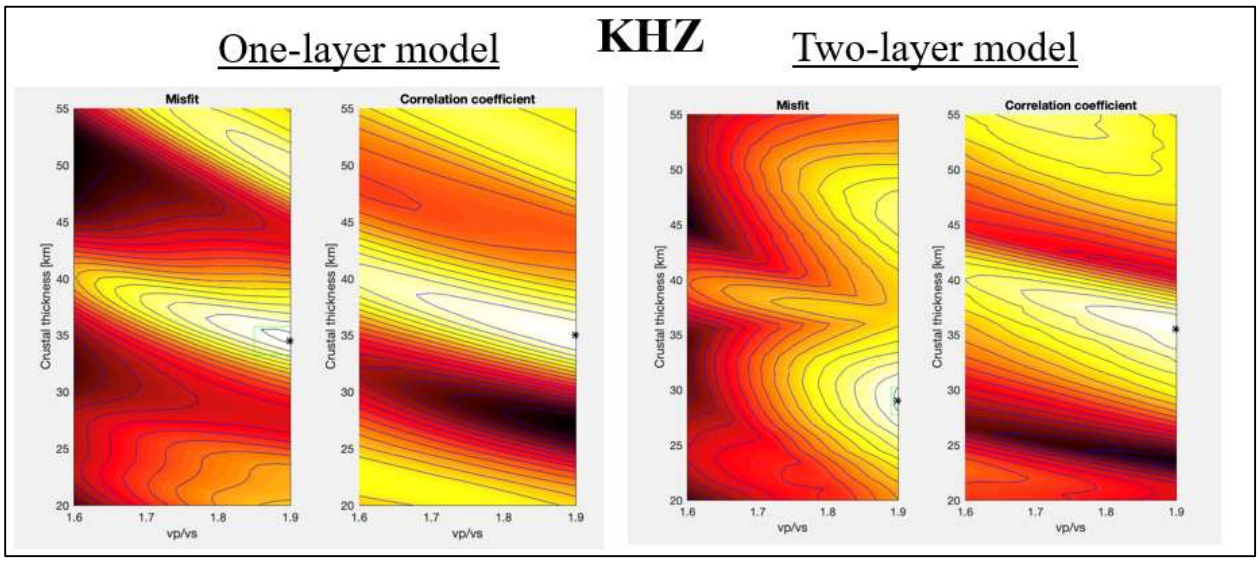

Figure 6.5: LEFT: One-layer model using the transfer function grid search procedure for station KHZ. RIGHT: Two-layer model using the transfer function grid search procedure for station KHZ.

Figure 6.6 shows the results for DCZ. For the one-layer model, a crustal thickness of 20 +/- 0.75 km and a Vp/Vs of 1.9 +/- 0.03 was calculated. For the two-layer model, the lowest misfit result was a crustal thickness of 20 +/- 0.25 km, and sedimentary thickness of 0.1 km and a Vp/Vs of 1.9 +/- 0.05. For station DCZ, the sedimentary thickness is low, and a one-layer model is most likely still usable. The Vp/Vs ratio for both station KHZ and DCZ is 1.9. This is an interesting result and suggests the model bounds might need to be changed.

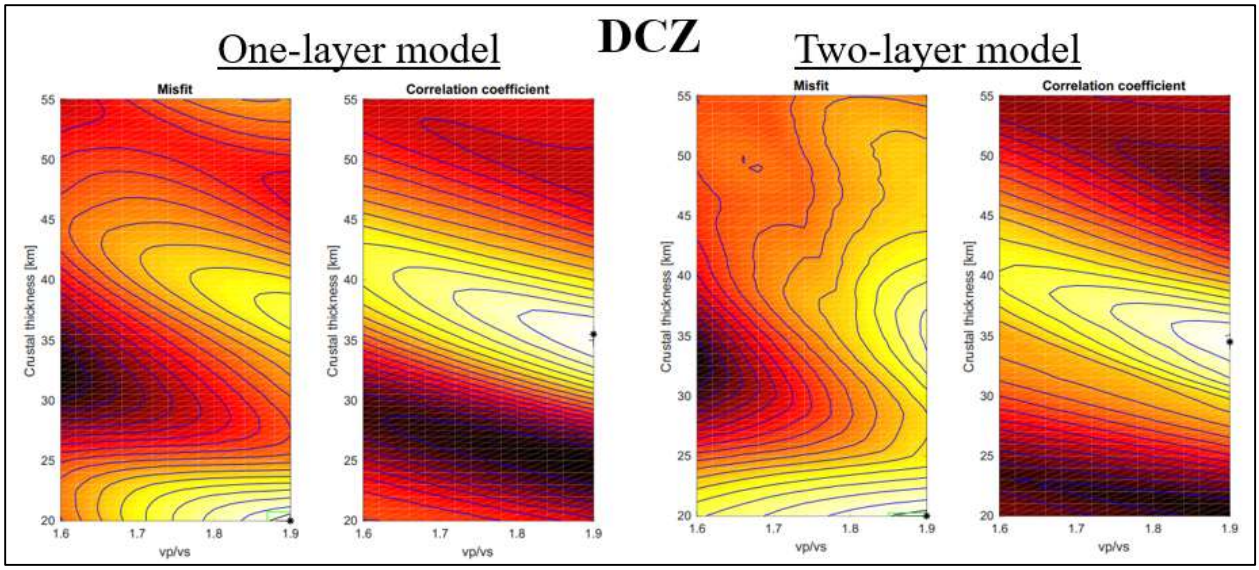

Figure 6.6: LEFT: One-layer model using the transfer function grid search procedure for station KHZ. RIGHT: Two-layer model using the transfer function grid search procedure for station DCZ.

The tabulated results for one-layer models and two-layer models at all stations are displayed in Table 6.3 and Table 6.4 respectively. The plotted results for the one-layer and two-layer models for all stations are shown in Figure 6.7 and Figure 6.8 respectively. When observing the results for both models in tabulated format and plotted spatially we can see that the one-layer model does not show much variation in crustal thickness and has little agreement with the results from the H-k stacking. The two-layer model allows room for a more variation and seems to fit a bit better, but it still seems like a more complex model is necessary due to the lack of variation in crustal thickness seen in Figure 6.8. In addition, the Vp/Vs ratio is not being resolved at all using a grid search procedure.

Table 6.3: Tabulated results for the transfer function grid search procedure using a one-layer model for all stations.

Station	Longitude	Latitude	Thickness (km)	Vp/Vs	Thickness Error (km)	Vp/Vs Error	Number of traces used
SYZ	169.14	-46.54	36.5	1.9	0.75	0.01	51
PYZ	166.68	-46.17	36	1.9	0.75	0.01	33
TUZ	169.63	-45.95	34.5	1.9	0.75	0.01	153
WHZ	167.95	-45.89	35.5	1.9	0.75	0.01	29
OPZ	170.6	-45.88	36	1.9	0.25	0.01	84
DCZ	167.15	-45.46	25.5	1.9	1.25	0.01	106
MLZ	168.12	-45.37	37.5	1.9	0.75	0.01	62
EAZ	169.31	-45.23	35	1.9	0.75	0.01	85
ODZ	170.64	-45.04	34.5	1.9	0.75	0.01	90
WKZ	169.02	-44.83	40.5	1.9	2.25	0.05	17
MSZ	167.93	-44.67	35	1.9	0.75	0.01	38
LBZ	170.18	-44.39	35	1.9	0.75	0.01	64
CVZ	171.01	-44.38	35.5	1.9	1.25	0.07	13
JCZ	168.79	-44.07	38	1.9	0.75	0.01	67
RPZ	171.05	-43.71	26.5	1.9	0.75	0.01	45
MQZ	172.65	-43.71	34.5	1.9	0.25	0.01	131
FOZ	169.82	-43.53	36	1.9	0.75	0.01	52
OXZ	172.04	-43.33	36	1.9	0.75	0.01	40
WVZ	170.74	-43.07	36	1.9	0.75	0.01	45
GVZ	173.03	-42.97	34.5	1.86	1.25	0.07	37
LTZ	172.27	-42.78	36	1.9	0.25	0.01	43
INZ	171.44	-42.72	36.5	1.9	0.75	0.01	24
KHZ	173.54	-42.42	34.5	1.9	1.25	0.05	50
THZ	172.91	-41.76	34.5	1.9	0.25	0.01	93
DSZ	171.8	-41.74	35.5	1.9	0.75	0.01	54
NNZ	173.38	-41.22	36.5	1.9	0.75	0.01	149
QRZ	172.53	-40.83	34	1.9	0.75	0.01	71

Table 6.4: Tabulated results for the transfer function grid search procedure using a two-layer model for all stations.

Station	Longitude	Latitude	Thickness (km)	Vp/Vs	Sediment Thickness (km)	Thickness Error (km)	Vp/Vs Error	Number of traces used
SYZ	169.14	-46.54	31.5	1.9	2.5	1.25	0.01	51
PYZ	166.68	-46.17	34.5	1.9	0.1	0.75	0.01	33
TUZ	169.63	-45.95	30	1.9	2.5	0.75	0.01	153
WHZ	167.95	-45.89	35	1.88	0.1	0.75	0.03	29
OPZ	170.6	-45.88	35.5	1.9	0.1	0.75	0.01	84
DCZ	167.15	-45.46	21.5	1.9	1.5	0.75	0.01	106
MLZ	168.12	-45.37	30.5	1.9	2.5	0.75	0.01	62
EAZ	169.31	-45.23	34.5	1.9	0.1	0.25	0.01	85
ODZ	170.64	-45.04	34	1.9	0.1	0.25	0.01	90
WKZ	169.02	-44.83	35.5	1.9	2.5	2.75	0.03	17
MSZ	167.93	-44.67	34.5	1.9	0.1	0.25	0.01	38
LBZ	170.18	-44.39	30	1.9	2.5	0.75	0.01	64
CVZ	171.01	-44.38	35.5	1.9	0.1	1.75	0.07	13
JCZ	168.79	-44.07	36	1.9	0.1	0.75	0.01	67
RPZ	171.05	-43.71	46.5	1.9	2.5	0.75	0.03	45
MQZ	172.65	-43.71	30	1.9	2.5	0.75	0.01	131
FOZ	169.82	-43.53	36	1.86	0.1	5.75	0.05	52
OXZ	172.04	-43.33	36	1.9	0.1	0.75	0.03	40
WVZ	170.74	-43.07	31	1.9	2.5	0.75	0.01	45
GVZ	173.03	-42.97	30	1.9	2.5	0.75	0.01	37
LTZ	172.27	-42.78	30	1.9	2.5	0.75	0.01	43
INZ	171.44	-42.72	35.5	1.9	0.1	0.75	0.05	24
KHZ	173.54	-42.42	29	1.9	1.25	1.25	0.01	50
THZ	172.91	-41.76	34.5	1.9	0.1	0.75	0.01	93
DSZ	171.8	-41.74	30	1.9	2.5	1.25	0.01	54
NNZ	173.38	-41.22	30.5	1.9	2.5	0.75	0.01	149
QRZ	172.53	-40.83	29.5	1.9	2.5	0.75	0.01	71

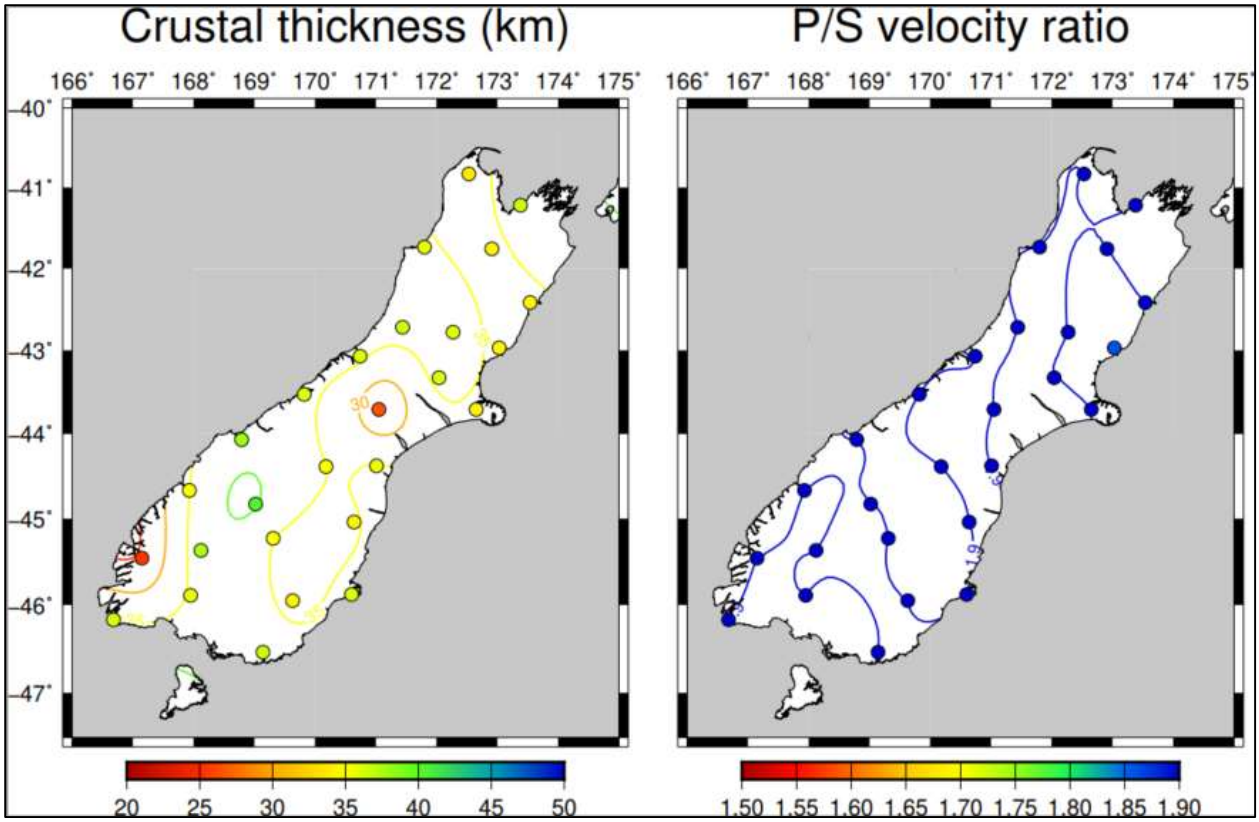

Figure 6.7: Crustal thickness and Vp/Vs variation across the South Island, New Zealand from the transfer function method using a grid search procedure for a one-layer model.

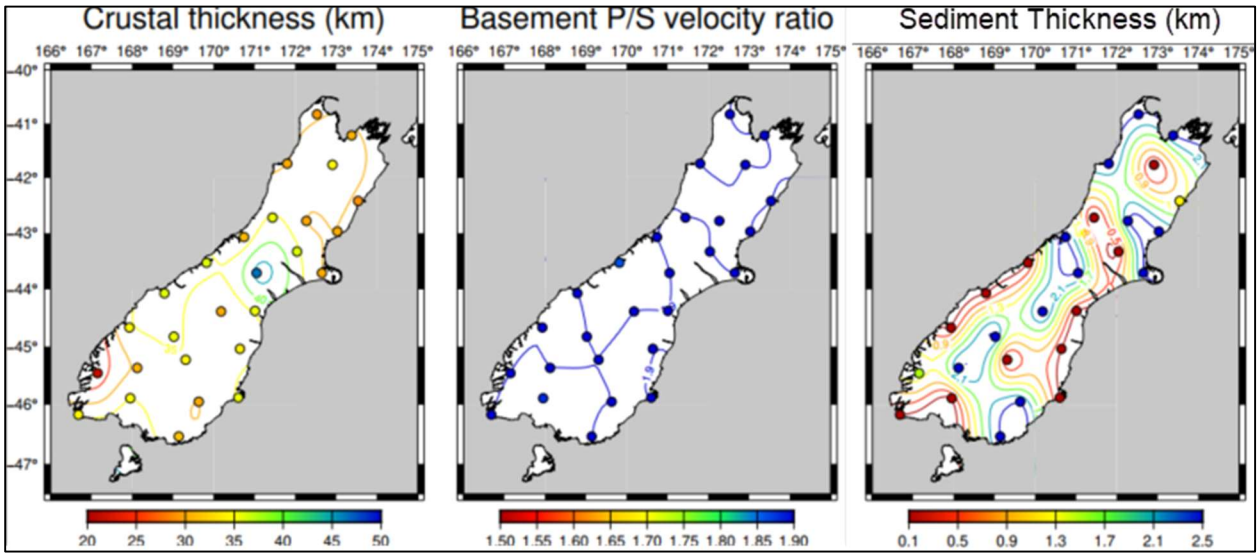

Figure 6.8: Sedimentary thickness, crustal thickness and Vp/Vs variation across the South Island, New Zealand from the transfer function method using a grid search procedure for a two-layer model.

6.3 Transfer-function (Monte Carlo style search)

To resolve the crustal thickness and Vp/Vs more robustly, a Monte Carlo style search was used, where 200 000 randomly generated models are used to calculate transfer functions for a three-layer model (sedimentary basin, upper crust and lower crust), using a starting model based on controlled source seismic data from Van Avendonk et. al. (2004). Table 6.5 contains the bounds for the models, generated from the final crustal model provided by Van Avendonk et. al. (2004).

Table 6.5: Parameter bounds for a three-layer model used in the transfer function Monte Carlo style search.

Three-layer starting model bounds

Parameter	*Range*
Sedimentary thickness	0.1-5 km
Sedimentary S velocity	1600-2000 m/s
Upper crustal thickness	15-50 km
Upper crustal S velocity	3100-4000 m/s
Lower crustal thickness	1-15 km
Lower crustal S velocity	3600-4100 m/s

Fixed parameters

Parameter	*Constant*
Sedimentary P velocity	3000 m/s
Sedimentary density	1.9 g/cm
Upper crustal P velocity	5900 m/s
Upper crustal density	2.5 g/cm
Lower crustal P velocity	6800 m/s
Lower crustal density	3 g/cm
Mantle P velocity	8000 m/s
Mantle S velocity	4440 m/s
Mantle density	3.6 g/cm

From the results in Figure 6.9 for station RPZ along the controlled-source reflection seismic transect 1 (Van Avendonk et. al., 2004), multiple interfaces may be present. This indicates that using a three-layer model is more appropriate than the one-layer and two-layer models used in the grid search procedure. In addition, results for layer thicknesses seem more robust than Vp/Vs ratio. The best model is has a sedimentary thickness of 3.2 km, upper crustal thickness of 19.2 km and a Vp/Vs of 1.89 and finally lower crustal thickness of 7.4 km. The best 2000 models for station KHZ are shown in Figure 6.10. To summarize these plots , the best model is has a sedimentary thickness of 3.4 km, upper crustal thickness of 16.5 km and a Vp/Vs of 1.89 and finally lower crustal thickness of 7.3 km. The sum of the thicknesses of these three layers is 27 km which is fairly close to the results of the H-k stacking method. However, it does seem that there are still some difficulties resolving the velocity ratios for these stations which is likely because the data are not sensitive to the Vp/Vs ratio and changing methods will not help resolve Vp/Vs. The Vp/Vs bounds were increased in different model iterations to 1.5-2.2 and 1.2-2.2 but extreme values for Vp/Vs that were infeasible for the entire crust were aquired.

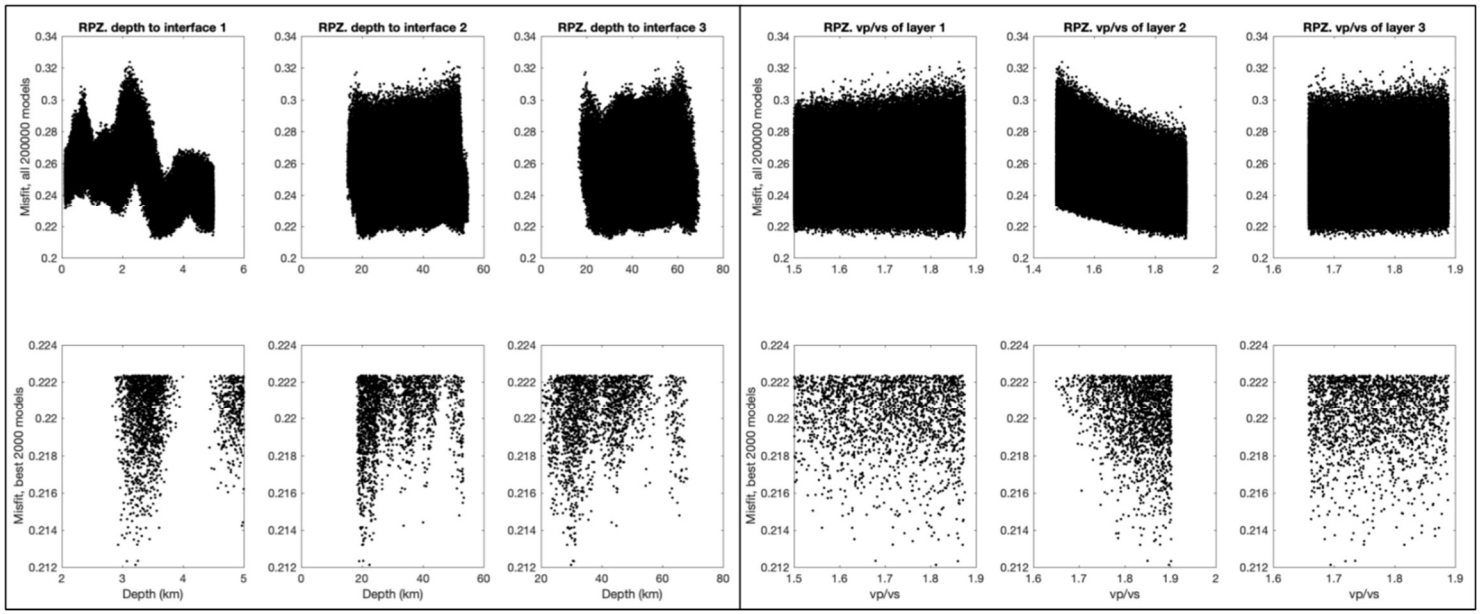

Figure 6.9: The best 2000 models for station RPZ. The best model has the following values: ***Layer 1*** *- Crustal thickness: 3.2 km;* ***Layer 2*** *- Crustal thickness: 19.2 km and Vp/Vs 1.89;* ***Layer 3*** *-Crustal thickness: 7.4 km; Misfit: 0.21.*

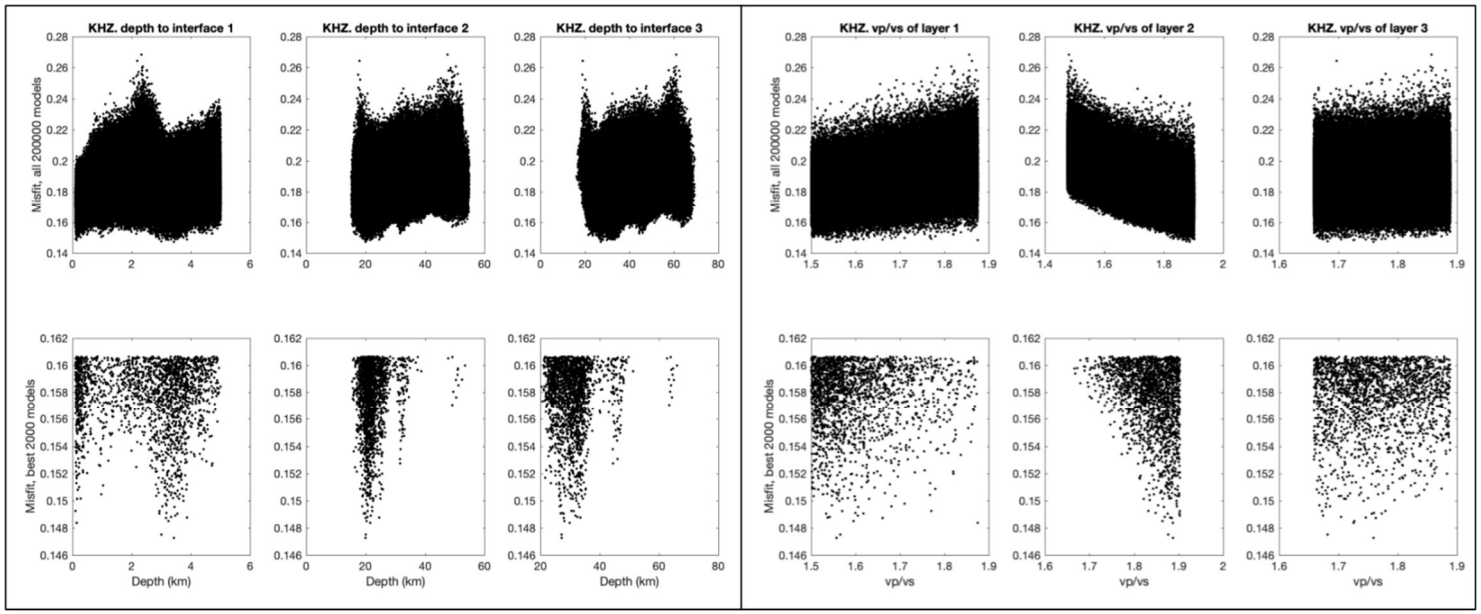

Figure 6.10: The best 2000 models for station KHZ. The best model has the following values: ***Layer 1*** *- Crustal thickness: 3.4 km;* ***Layer 2*** *- Crustal thickness: 16.5 km and Vp/Vs 1.89;* ***Layer 3*** *-Crustal thickness: 7.3 km; Misfit: 0.15.*

Final results from the transfer function approach using the Monte Carlo search were obtained at 27 stations and over 2500 events. This method revealed variations of crustal thickness (depth to Moho) and Vp/Vs ratio from 20.8 – 38.4 km and 1.55 – 1.9 respectively. These final results for the single best fitting model for each station have been plotted spatially and tabulated in Figure 6.11 and Table 6.6. The results show thinner crust toward the southeast and thicker crust toward the centre of the island. The highest values of crustal thickness are located southwest near the Alpine Fault and the lowest values of crustal thickness are seen near the Otago Schist, southeast of the Alpine Fault. In addition, the Vp/Vs ratio increases through the centre of the island and lowers towards the Alpine Fault and the southeast coastlines. Sedimentary thicknesses range from 0.1 – 4.4 km, with the thicker sedimentary layers located northeast, northwest and throughout the centre of the island. Thinner sedimentary layers are located in the southeast of the island and seem to be very localized. Lower crust or underplate thicknesses ranging from 4 - 15 km were resolved. Thickness increases throughout the centre of the island and is thinner toward the northwest and southeast.

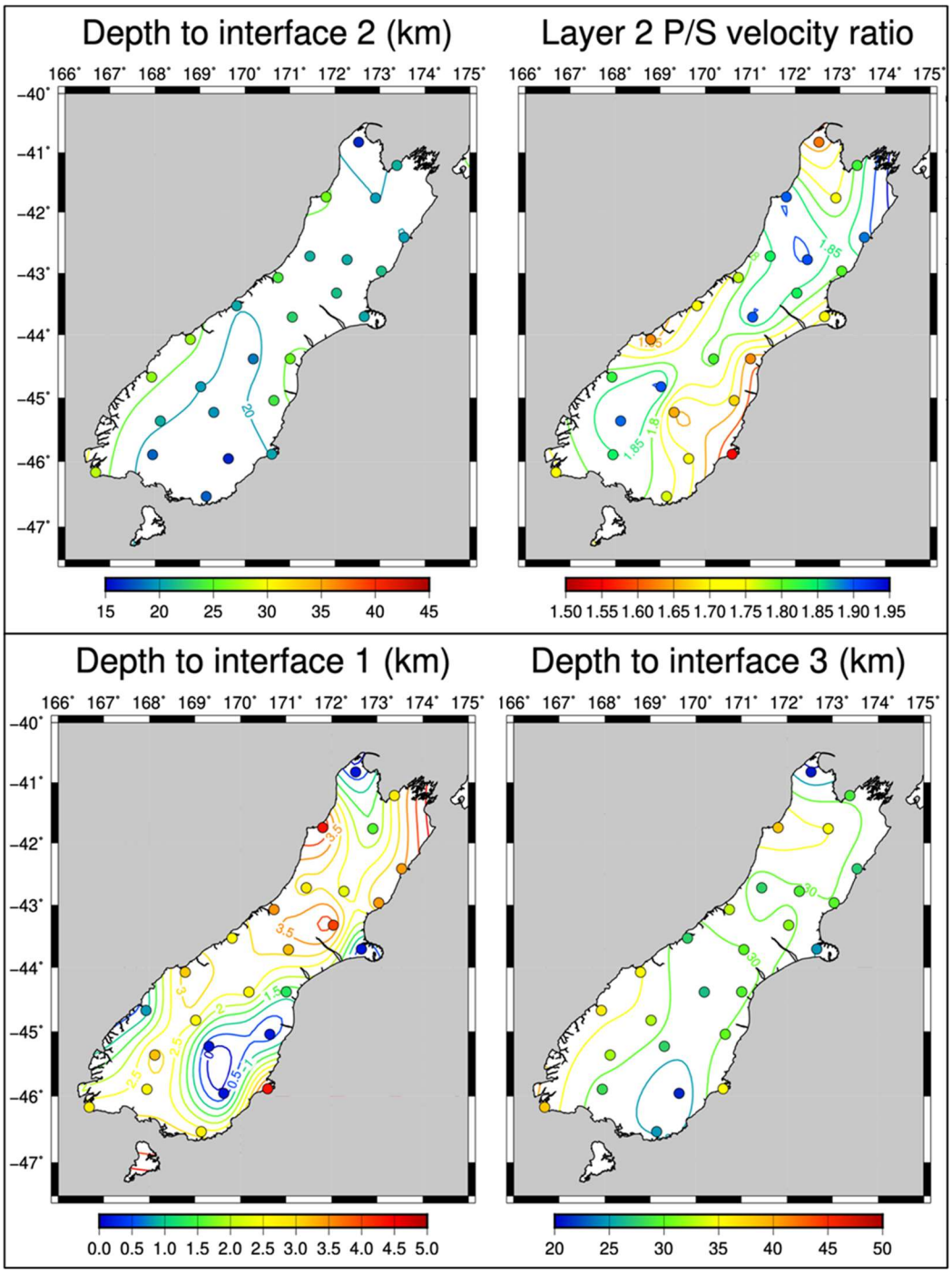

Figure 6.11: TOP: Upper crustal thickness and Vp/Vs across the South Island, New Zealand from the transfer function method using a Monte Carlo style algorithm for a three-layer model. BOTTOM: Sedimentary thickness and lower crustal thickness variation across the South Island, New Zealand from the transfer function method using a Monte Carlo style algorithm for a three-layer model.

Table 6.6: Tabulated results from the transfer function method using a Monte Carlo style algorithm for a three-layer model.

Station	Longitude	Latitude	Thickness1 (km)	Thickness2 (km)	Thickness3 (km)	Vp/Vs2	Misfit
SYZ	169.14	-46.54	2.7	15.2	6.9	1.76	0.15
PYZ	166.68	-46.17	2.8	25.1	10.4	1.74	0.16
TUZ	169.63	-45.95	0.1	16.0	5.1	1.71	0.12
WHZ	167.95	-45.89	2.7	15.4	10.2	1.85	0.11
OPZ	170.60	-45.88	4.4	15.9	14.8	1.55	0.21
MLZ	168.12	-45.37	3.2	17.5	11.5	1.89	0.14
EAZ	169.31	-45.23	0.1	19.5	8.1	1.65	0.16
ODZ	170.64	-45.04	0.2	23.5	6.5	1.68	0.14
WKZ	169.02	-44.83	2.6	17.4	12.6	1.90	0.22
MSZ	167.93	-44.67	0.8	25.8	9.6	1.82	0.16
LBZ	170.18	-44.39	2.6	16.1	7.7	1.81	0.13
CVZ	171.01	-44.38	1.3	24.2	4.0	1.63	0.18
JCZ	168.79	-44.07	3.1	23.8	8.5	1.63	0.16
RPZ	171.05	-43.71	3.2	19.2	7.5	1.90	0.21
MQZ	172.65	-43.71	0.2	20.2	4.3	1.70	0.13
FOZ	169.82	-43.53	2.6	17.8	7.1	1.71	0.13
OXZ	172.04	-43.33	4.0	17.4	9.9	1.84	0.16
WVZ	170.74	-43.07	3.5	20.4	9.1	1.77	0.13
GVZ	173.03	-42.97	3.4	18.1	8.1	1.80	0.20
LTZ	172.27	-42.78	2.3	18.3	8.7	1.90	0.15
INZ	171.44	-42.72	2.8	18.0	6.8	1.84	0.13
KHZ	173.54	-42.42	3.4	16.5	7.3	1.89	0.15
THZ	172.91	-41.76	1.6	18.4	15.0	1.75	0.13
DSZ	171.80	-41.74	4.4	21.3	12.7	1.90	0.12
NNZ	173.38	-41.22	2.8	18.1	8.1	1.82	0.14
QRZ	172.53	-40.83	0.2	16.1	4.6	1.62	0.10

7 Discussion

In the previous chapter we were introduced to the final results of the transfer function method and described how the crustal thickness and Vp/Vs ratio vary spatially. The results for the depth to each interface and the Vp/Vs ratio have been mapped with the geological boundaries from Beaumont *et al.,* (1996) superimposed. Figure 7.1 outlines the depth to interface 1 and the Vp/Vs of the first layer. This depth to interface 1 is interpreted to be the depth to the bottom of the sedimentary layer. The hotter colors represent thicker areas and lower Vp/Vs and the cooler colors represent thinner areas and higher Vp/Vs. Interface 1 is deeper towards the centre of the island and shallows to the southeast. There seems to be little to no sedimentary material present on top of the Otago Schist. Thick sediment is observed in the Canterbury Basin, except for under the Banks Peninsula Volcano, where station MQZ is located. The Vp/Vs is generally low across the entire island which makes some sense if we are treating this layer as the sedimentary layer (Lowrie, 2007).

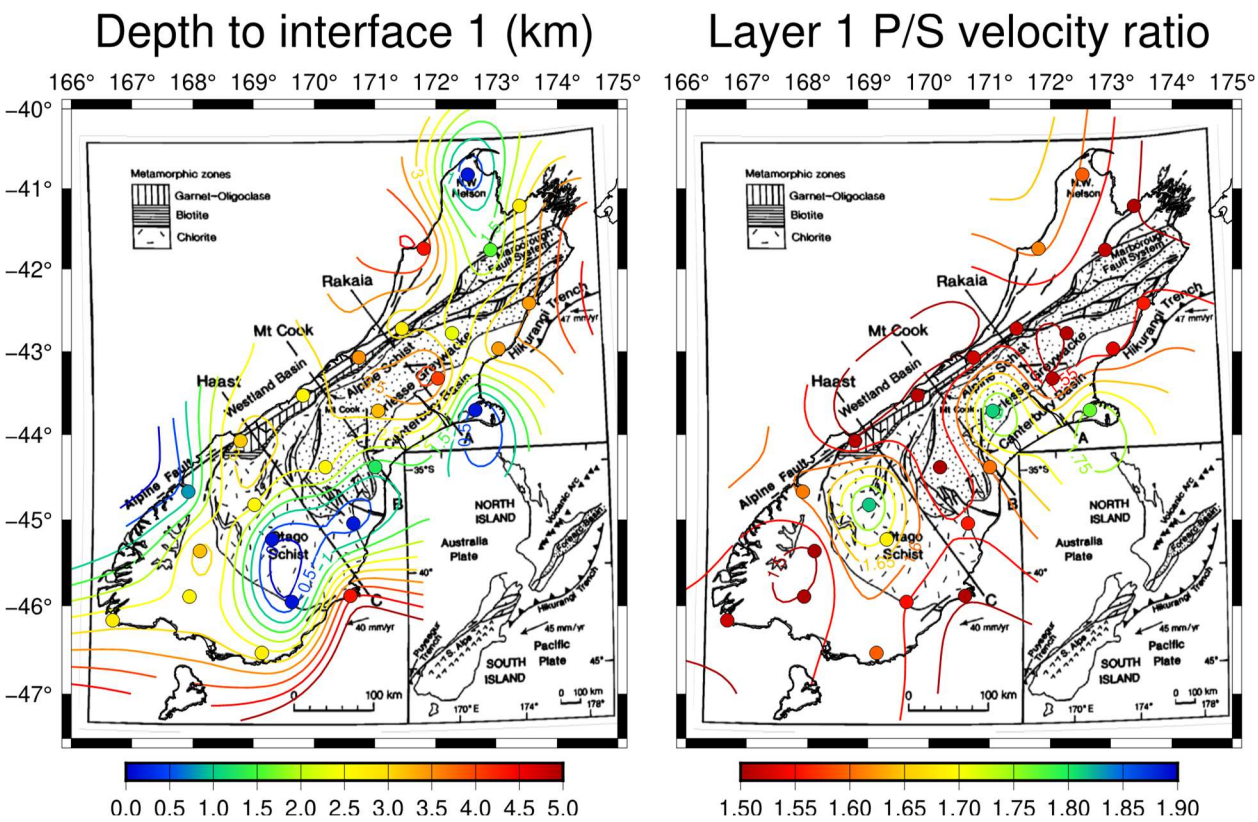

Figure 7.1: Left: Depth to interface 1 overlain on geological boundaries from Beaumont et.al., (1996). Right: Layer 1 Vp/Vs ratio overlain on geological boundaries from Beaumont et.al., (1996).

The depth to interface 2 is shown in Figure 7.2, and is more spatially coherent than interface 1. The upper crust thins out toward the south and thickens toward the center of the island. Areas of thicker upper crust could be from compression zones with sagging (Salmon, *et al.,* 2013). Station DCZ, located in the southwest, yielded an improbable high value (36 km) and was removed. This station had the highest misfit of all stations (0.223). The Vp/Vs results are also quite interesting. High values are present through the centre of the island, along the Southern Alps and lower values occur towards the northwest and southeast coastlines. The Vp/Vs calculated here is not influenced by the sedimentary layer or the lower crust.

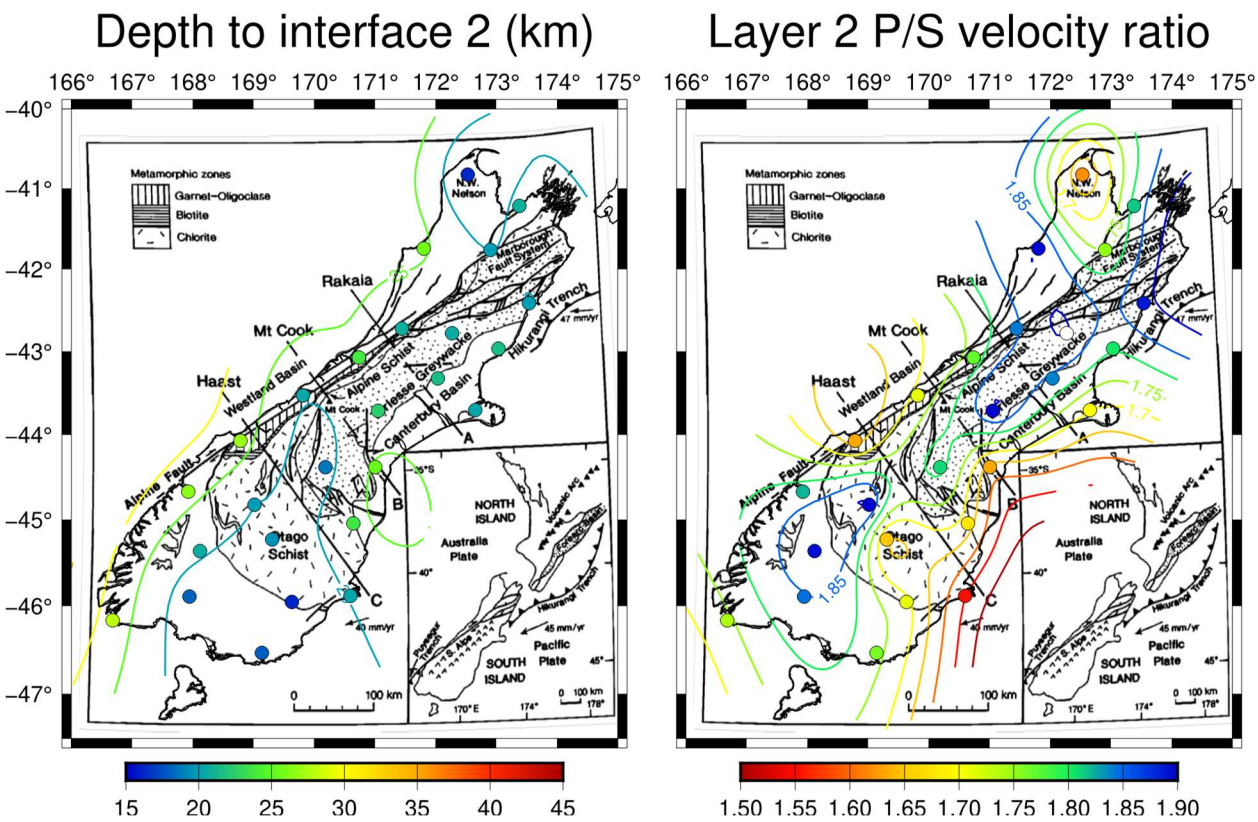

Figure 7.2: Left: Depth to interface 2 overlain on geological boundaries from Beaumont et.al., (1996). Right: Layer 2 Vp/Vs ratio overlain on geological boundaries from Beaumont et.al., (1996).

The depth to interface 3 is interpreted to be the depth to the Moho. Figure 7.3 shows that the Moho deepens as we move from the southeast coastline to the northwest coastline. The Vp/Vs map looks fairly coherent and shows moderate values in the centre of the island and higher values as we look northeast and southwest. The higher Vp/Vs vales correspond to the Otago Schist and the moderate values correspond to the Alpine Schist, Torlesse greywackes, Westland Basin, and Canterbury Basin.

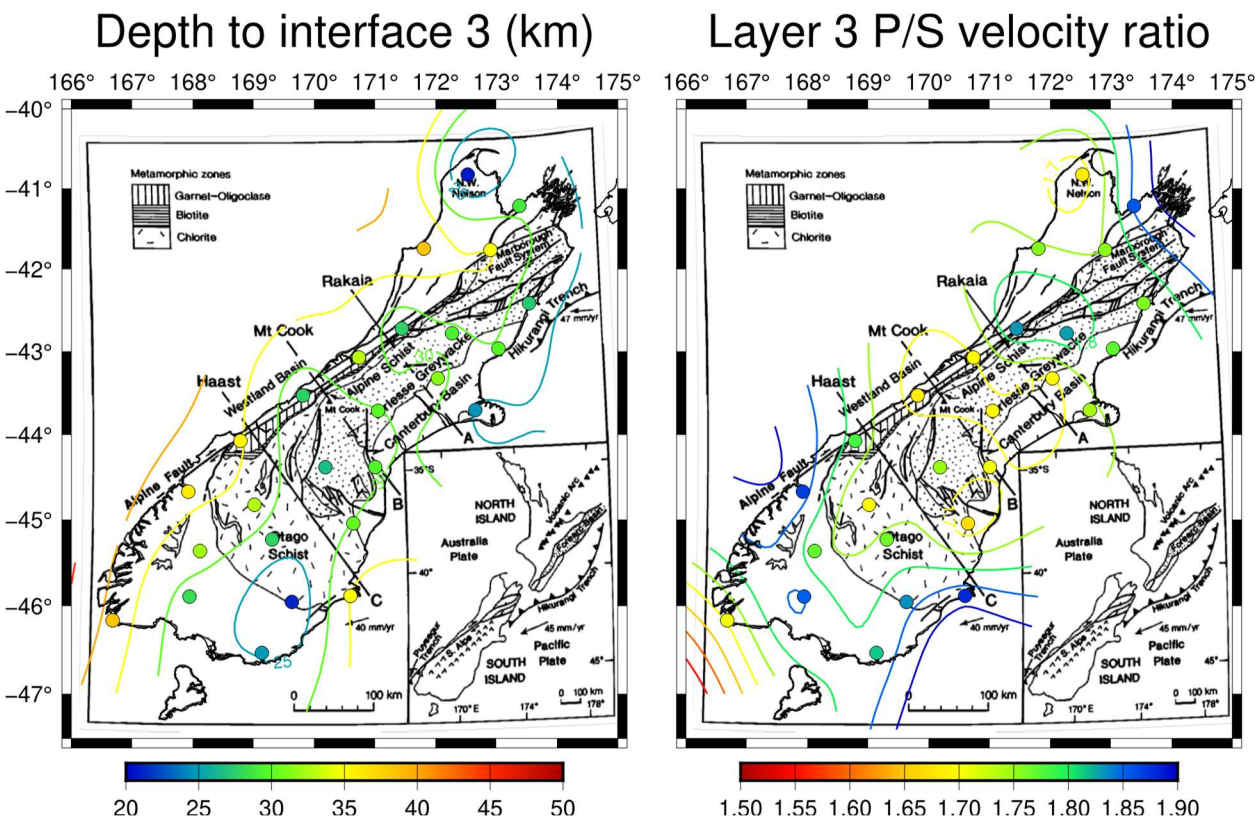

Figure 7.3: Left: Depth to interface 3 overlain on geological boundaries from Beaumont et.al., (1996). Right: Layer 3 Vp/Vs ratio overlain on geological boundaries from Beaumont et.al., (1996).

7.1 Comparison with Past Geophysics

Gravity

An airborne gravity survey was conducted over the entirety of New Zealand, with over 50,000 line kilometers of data collected by GNS Science, Victoria University of Wellington and Land Information New Zealand between August 2013 and June 2014. The data set provides 1 arc minute imagery of the Bouguer anomalies. These anomalies have been downward continued to the ground surface (McCubbine et al, 2017). The transfer function results have been superimposed on the Bouguer anomalies in Figures 7.4-7.6, where the warmer colours are positive Bouguer anomalies, and the cooler colours are negative Bouguer anomalies. Mafic igneous rocks more often result

in positive gravity anomalies, while the sedimentary basins with low density will result in negative anomalies.

Figure 7.4 shows the depth to interface 1 overlain on the Bouguer gravity raster image. Areas of thicker sediments are areas where we have negative Bouguer anomalies. Areas that we have thinner sediments are where we have positive Bouguer anomalies. This is encouraging as we would expect areas with more sediment to yield a gravity low and areas with less sediment to yield a gravity high. There does not seem to be much correlation between the gravity anomalies and the Vp/Vs ratio but is possible that the negative Bouguer anomalies have a minor correlation with higher Vp/Vs ratios.

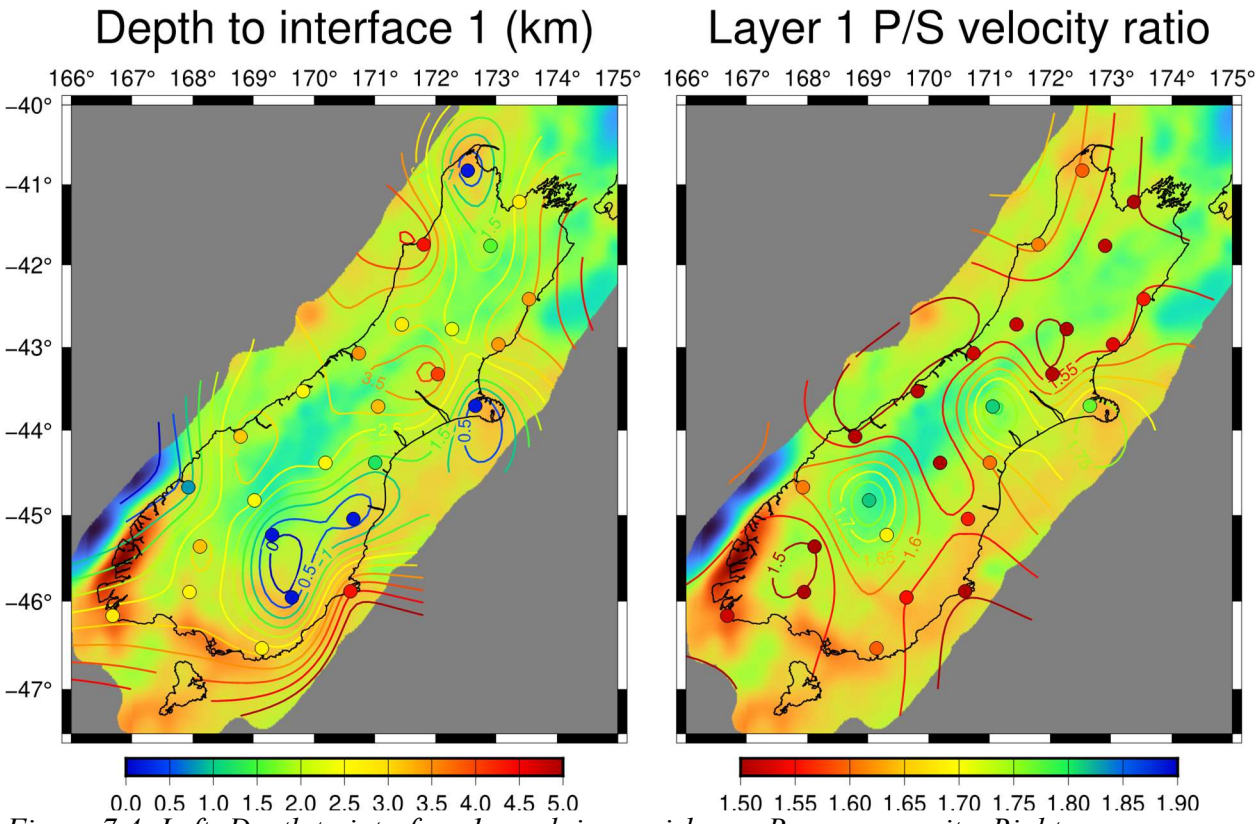

Figure 7.4: Left: Depth to interface 1 overlain on airborne Bouguer gravity. Right: Layer 1 Vp/Vs ratio overlain on airborne Bouguer gravity,

Figure 7.5 shows the depth to interface 2 overlain on the same Bouguer gravity map. Where the upper crust thins out toward the southeast and northwest, the gravity values increase. The thickness increases toward the centre of the island, while the gravity values decrease. A shallow interface 2 would indicate that lower crustal material is closer to the surface but correlates with gravity lows instead of highs. This is the opposite of what is expected if the lower crust is denser than the upper crust. The Vp/Vs results are also quite interesting. There seem to be high values through the centre of the island and lower values towards the northwest and southeast coastlines, which also correlates with low (less dense) and high (denser) gravity values respectively. Considering the depth to interface 2 has the wrong correlation with gravity, it is more likely that the gravity variation is related to compositional variations, as indicated by the Vp/Vs – high Vp/Vs correlated with low density.

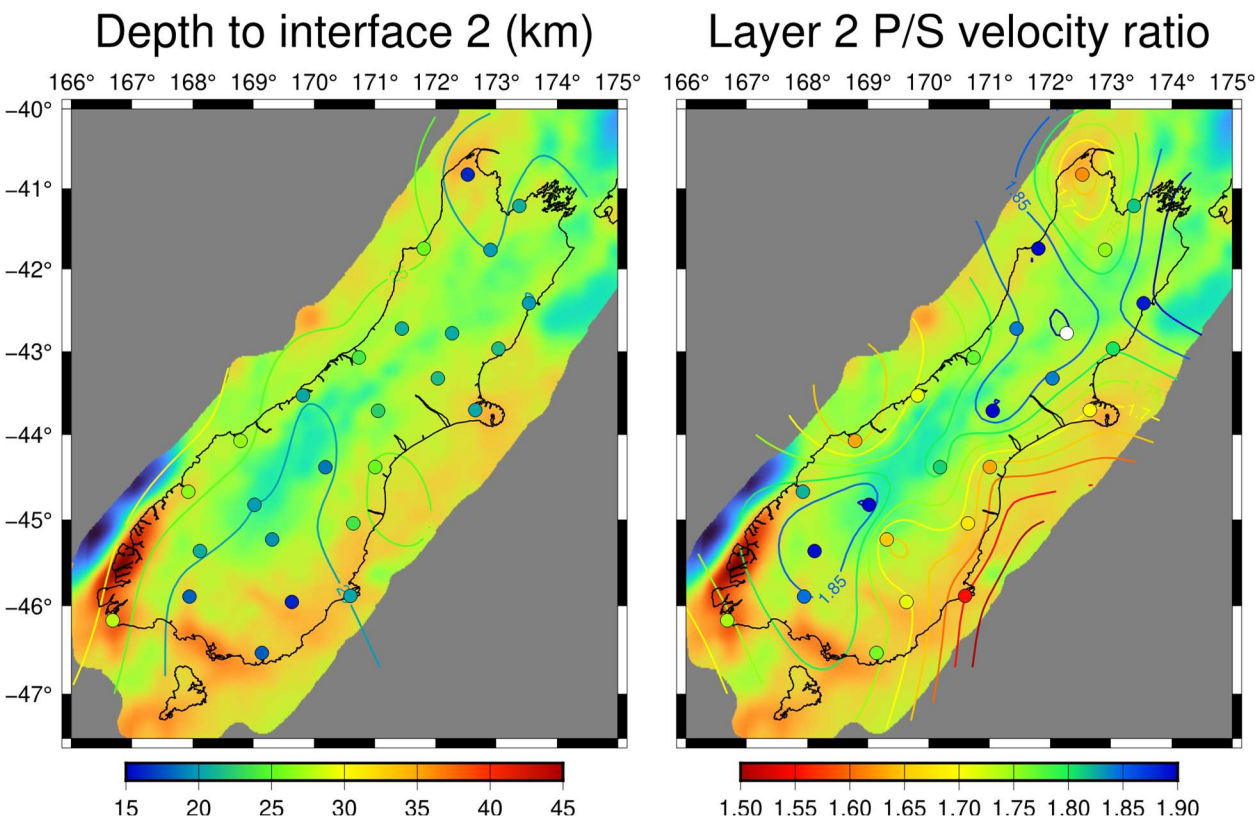

Figure 7.5: Left: Depth to interface 2 overlain on airborne Bouguer gravity. Right: Layer 2 Vp/Vs ratio overlain on airborne Bouguer gravity,

Figure 7.6 shows the depth to interface 3 and displays some correlation between the areas of thinner lower crust and positive Bouguer anomalies. The deeper Moho seems to correlate with positive Bouguer anomalies in the middle of the island where the depths are moderate (approximately 30 km). The Vp/Vs map shows moderate values in the centre of the island (corresponding to negative Bouguer anomalies) and higher values as we look northeast and southeast/west (positive Bouguer anomalies). This correlation is the opposite of what was seen for layer 2, where lower Vp/Vs was associated with gravity highs. A lower Vp/Vs should indicate lower mafic content which would also be less dense. The Vp/Vs sensitivity is much better for layer 2 than

layer 3 and other factors can affect Vp/Vs, especially in a complex environment like New Zealand.

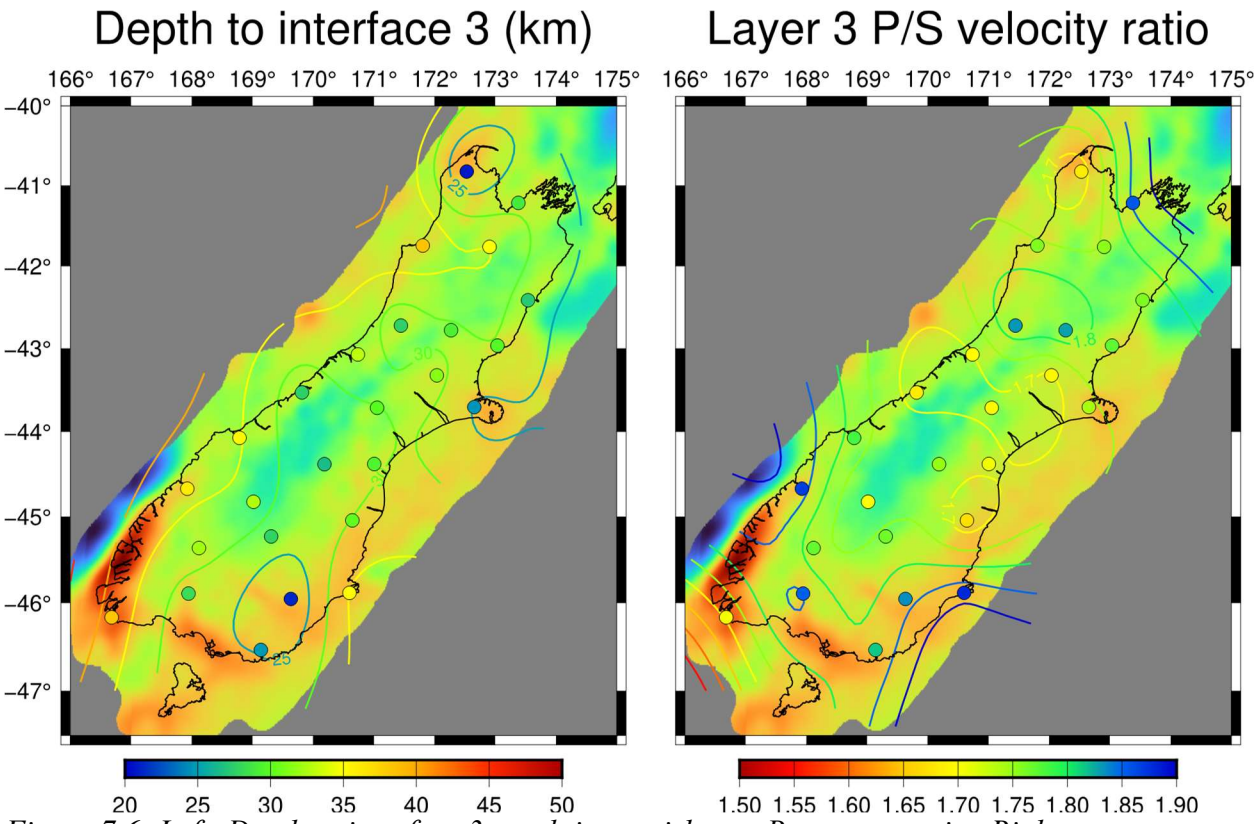

Figure 7.6: Left: Depth to interface 3 overlain on airborne Bouguer gravity. Right: Layer 3 Vp/Vs ratio overlain on airborne Bouguer gravity,

Magnetics

Regional magnetic data was downloaded using Oasis Montaj from the World Digital Magnetic Anomaly Map (Dyment, *et.al.,* 2003). The RTP (reduced to pole) data were downloaded and the results of the transfer function method were overlain on the magnetic data. Mafic rocks are more magnetic and are likely to be associated with magnetic highs unless remnant magnetism is present, and sedimentary rocks are not very magnetic.

Figure 7.7 shows the depth to interface 1 overlain on the RTP magnetics. The magnetic highs correspond to areas where no sediment is present. The lack of sediment means that the magnetic rocks are closer to surface and will increase the magnitude of the magnetic response. There does not seem to be much correlation between the magnetics and the Vp/Vs of the top layer. This is mostly likely due to the response of the magnetics being mostly attributable to the upper and lower crust.

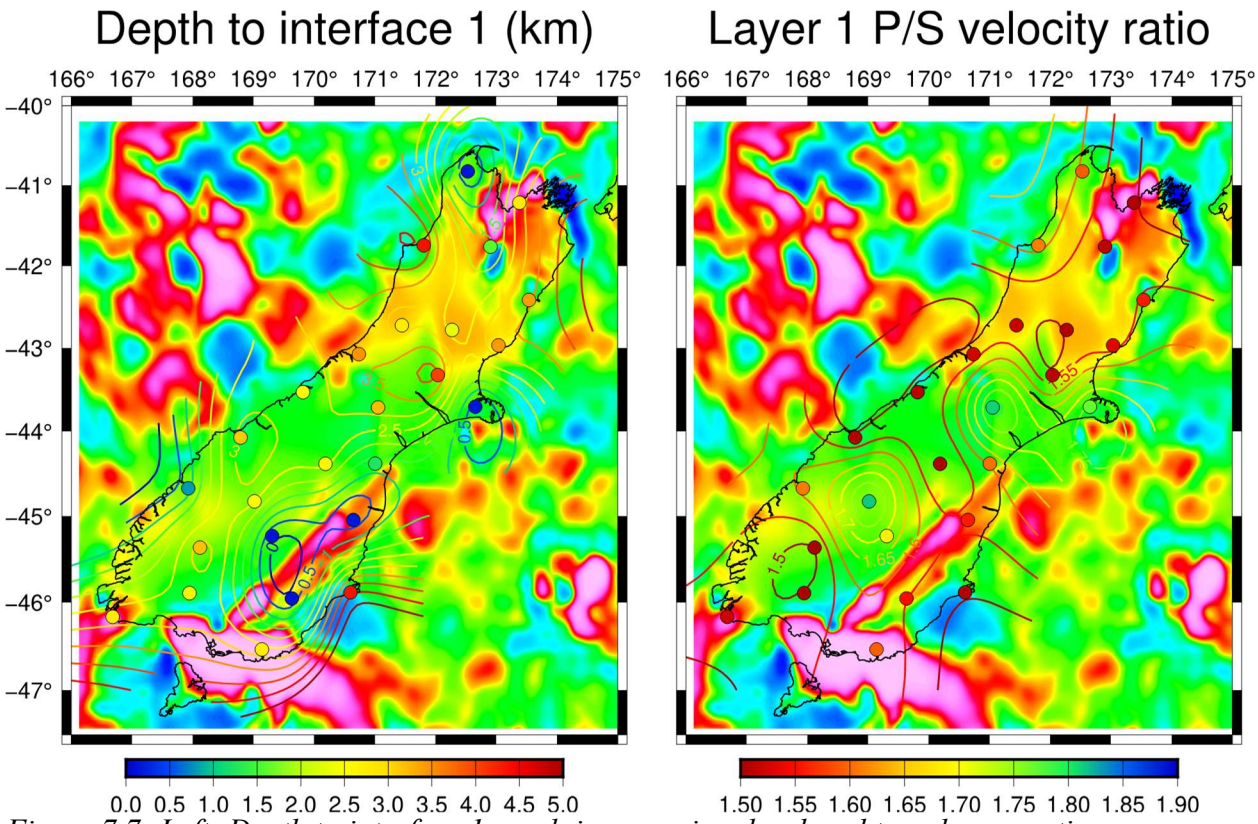

Figure 7.7: Left: Depth to interface 1 overlain on regional reduced to pole magnetics. Right: Layer 1 Vp/Vs ratio overlain on regional reduced to pole magnetics.

Figure 7.8 shows the depth to interface 2 overlain on the RTP magnetics. While there does not seem to be any spatial correlation with the depth, there does seem to be a correlation with the Vp/Vs ratio. The higher Vp/Vs ratio in the centre of the island coincides with a more moderate magnetic response, moderate Vp/Vs ratio values seem

to flank magnetic highs and the low Vp/Vs ratios lie within magnetic lows. Generally, a higher Vp/Vs ratio indicates more mafic material (more magnetic) is present, and a lower Vp/Vs ratio indicates more felsic material (less magnetic). The moderate magnetics associated with the high Vp/Vs along the centre of the island could be due to the overlying sediments reducing the effect of the underlying mafics. This is consistent with the magnetic highs corresponding with high Vp/Vs and sediment free zones (thin or absent layer 1) in the north and south of the island.

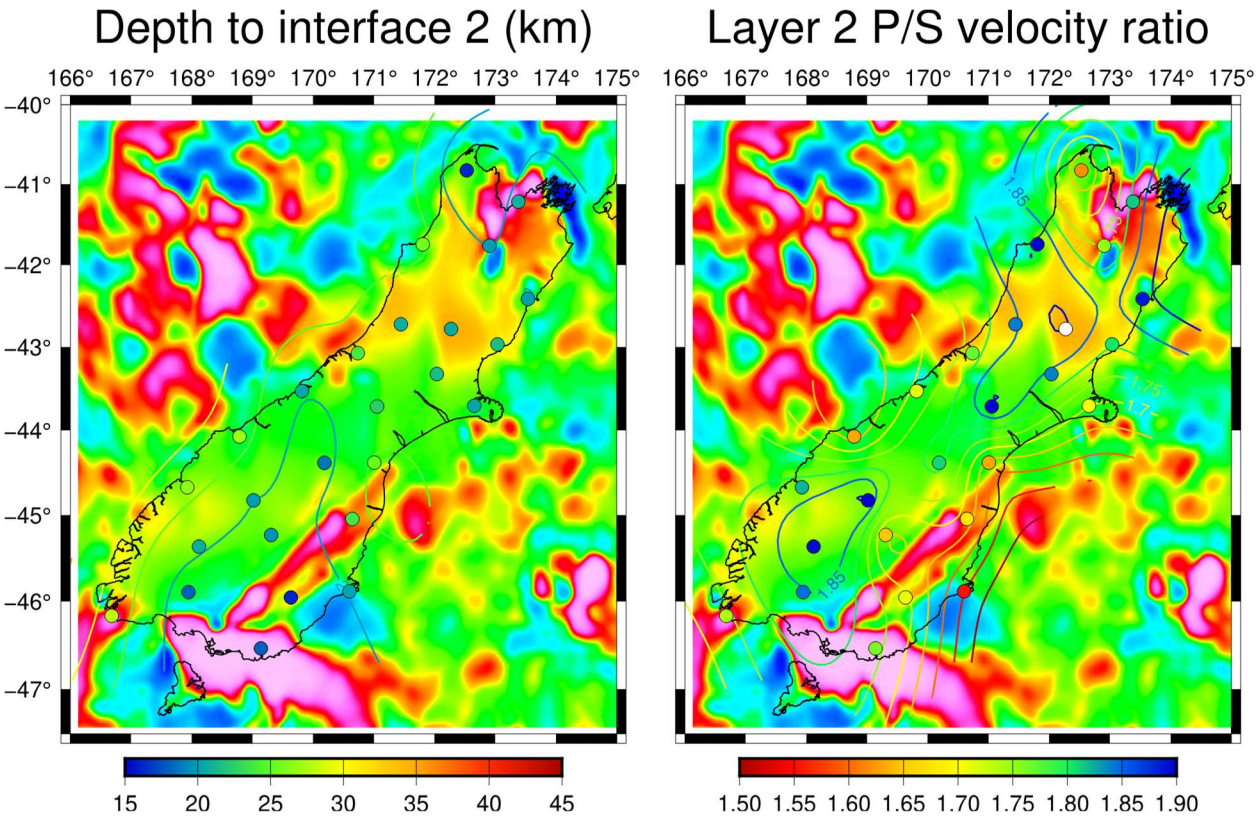

Figure 7.8: Left: Depth to interface 2 overlain on regional reduced to pole magnetics. Right: Layer 2 Vp/Vs ratio overlain on regional reduced to pole magnetics.

Figure 7.9 shows the depth to interface 3. Again, there does not seem to be any connection between the depth and the magnetic data. There is a much stronger correlation between the Vp/Vs ratio and the magnetics, but it should be kept in mind

that magnetics are mostly sensitive to the upper crust. The higher Vp/Vs ratio directly coincides within the magnetic highs and the lower Vp/Vs ratio lies within magnetic lows. This apparent correlation is most likely due to the Vp/Vs of layers 2 and 3 being anticorrelated (similar spatial pattern but the highs and lows are reversed).

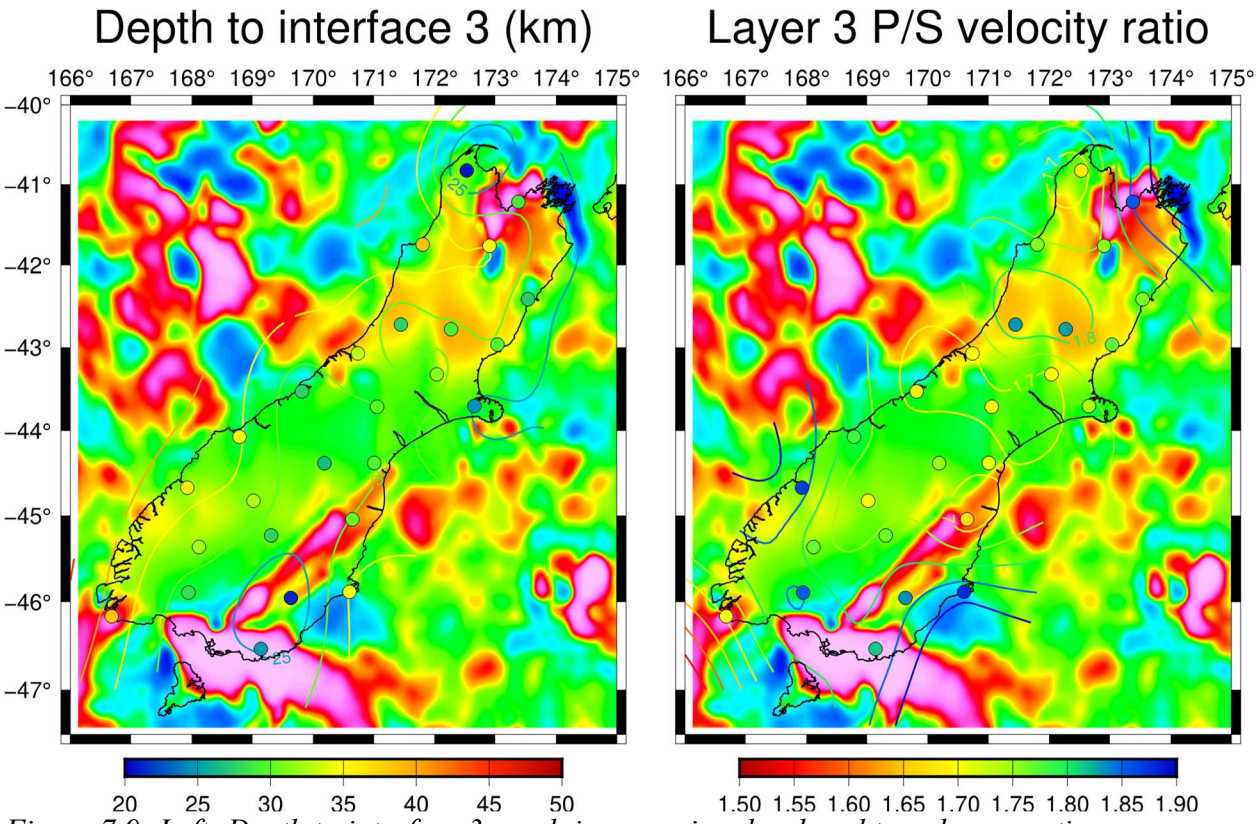

Figure 7.9: Left: Depth to interface 3 overlain on regional reduced to pole magnetics. Right: Layer 3 Vp/Vs ratio overlain on regional reduced to pole magnetics.

Seismic

We can do a direct comparison of structure over the SIGHT line (Van Avendonk et. al., 2004). RPZ is a station on the SIGHT transect 1 line, approximately 300 km down the line in Figure 7.10. After examining the thicknesses of each layer and the velocities at that location and comparing with the results for station RPZ shown in Table 7.1, the second and third interfaces are shallower. This may be due to dipping

structures and Moho topography present here. we can see a strong correlation for the thicknesses of each layer. The best model from the transfer function method for layer 1 is 3.2 km and the first layer off the profile is approximately 2.5 km. The best model for layer 2 is 19.2 km and the second layer off the seismic velocity model is approximately 22.5 km. The best model for layer 3 is 7.5 km and the third layer off the tomographic inversion is approximately 5 km. Layer 3 is represented by the old oceanic crust interpreted in the seismic velocity model, which would explain why the third layer is required to fit the data. Layer 1 would be the sediment layer, layer 2 is the felsic crust and layer 3 is the mafic layer at the base.

Table 7.1: Tabulated results for station RPZ from the transfer function method using a Monte Carlo style algorithm for a three-layer model. The model bounds used for these results were derived from Van Avendonk et. al., (2004).

Station	Longitude	Latitude	Thickness1 (km)	Thickness2 (km)	Thickness3 (km)	Vp/Vs2	Misfit
RPZ	171.05	-43.71	3.2	19.2	7.5	1.90	0.21

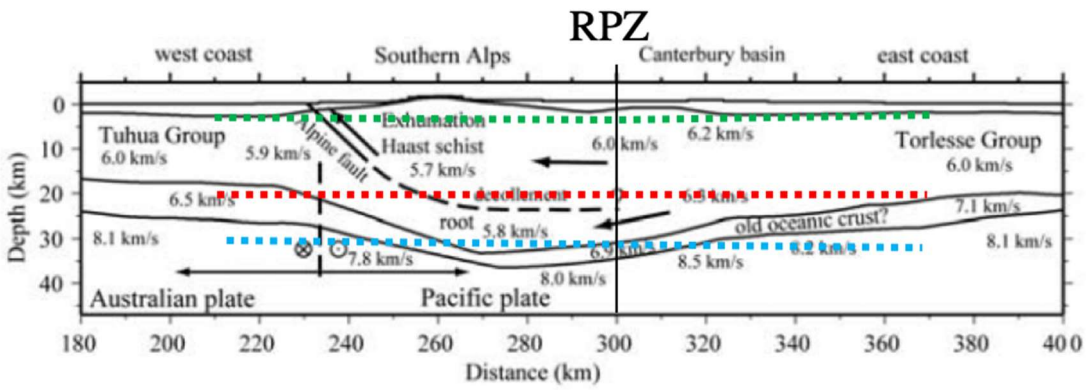

Figure 7.10: Seismic velocity model across Transect 1 from tomography inversion completed by Van Avendonk et al., (2004). The drawn in dashed green, red and blue lines are the depth to interface 1, 2 and 3 respectively. Station RPZ is approximately 300 km down the line. The results are shallower than the model shown here, which is possibly due to dipping interfaces and rapid Moho depth variations near the station. The results match fairly well if you average the Van Avendonk et al., (2004) results laterally and then compare with the sketch. In addition, the second interface seems to line up well with where the Alpine Fault flattens out approximately 260 km.

7.2 Single Station Modelling

Instead of using a single set of model bounds for every station across the South Island, model bounds can be assigned to each station separately since the structure can change drastically over just a few kilometers, if constraints from other studies are available. For this example of single station modelling, Kleffman *et. al., (*1998*)*, was used to determine the model bounds for station ODZ. A velocity-depth model shown in Figure 7.11 was completed by Kleffman *et. al., (*1998*)* and used to generate the following model bounds in Table 7.2. These P and S wave velocities are all generally higher than the velocities derived using Van Avendonk et. al., (2004). The 2000 best models for station ODZ are shown in Figure 7.12 and the best model is listed in Table 7.3 along with the original results. The original results have a negligible difference in the depth to interface 1 (~30 m), the single station model has a higher depth to interface 2 (~2 km increase) and the single station model has a higher depth to interface 3 (~1 km increase). In addition, the velocity ratio for the single station model is a bit lower (~0.04). These results are quite comparable to the 2D velocity-depth model and show that the models can be further refined by doing single station modelling if additional information is known in the vicinity of a station, instead of using one set of model bounds for all stations. This example indicates that the trade-offs cannot be completely resolved using teleseismic data, and therefore the depth to Moho is sensitive to starting assumptions. This may also explain why the depth to Moho results are shallower in my results compared to other studies.

Table 7.2: Parameter bounds for a three-layer model used in the transfer function Monte Carlo style search. These model bounds were derived from Kleffman et. al., (*1998*).

Three-layer starting model bounds

Parameter	*Range*
Sedimentary thickness	0.1-5 km
Sedimentary S velocity	2300-3000 m/s
Upper crustal thickness	20-60 km
Upper crustal S velocity	3400-4300 m/s
Lower crustal thickness	2-30 km
Lower crustal S velocity	4200-4800 m/s

Fixed parameters

Parameter	*Constant*
Sedimentary P velocity	4950 m/s
Sedimentary density	1.9 g/cm
Upper crustal P velocity	6200 m/s
Upper crustal density	2.5 g/cm
Lower crustal P velocity	8000 m/s
Lower crustal density	3 g/cm
Mantle P velocity	8700 m/s
Mantle S velocity	4830 m/s
Mantle density	3.6 g/cm

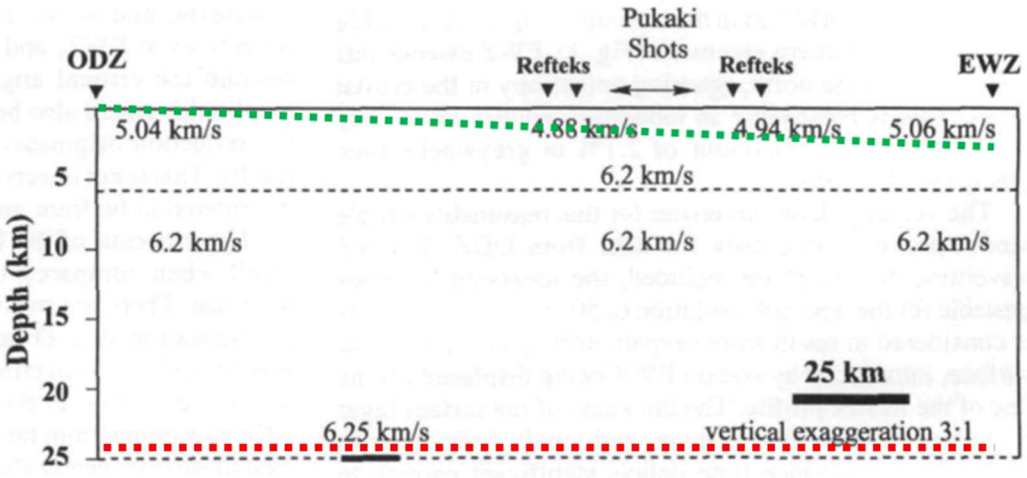

Figure 7.11: A 2D velocity-depth model between station ODZ and EWZ was derived from an inversion of the first arrival data. This model is used to create model bounds

for the single station transfer function modelling (Kleffman et. al., 1998). The drawn in green and red lines are the depth to interface 1 and 2 respectively.

Table 7.3: Tabulated results for station ODZ from the transfer function method using a Monte Carlo style algorithm for a three-layer model. The first row uses the model bounds derived from Kleffman et. al., (*1998*) *and the second row is the original results.*

Station	**Longitude**	**Latitude**	**Thickness1 (km)**	**Thickness2 (km)**	**Thickness3 (km)**	**Vp/Vs2**	**Misfit**
ODZ (single)	170.64	-45.04	0.1	25.6	7.4	1.64	0.13
ODZ (all)	170.64	-45.04	0.2	23.5	6.5	1.68	0.14

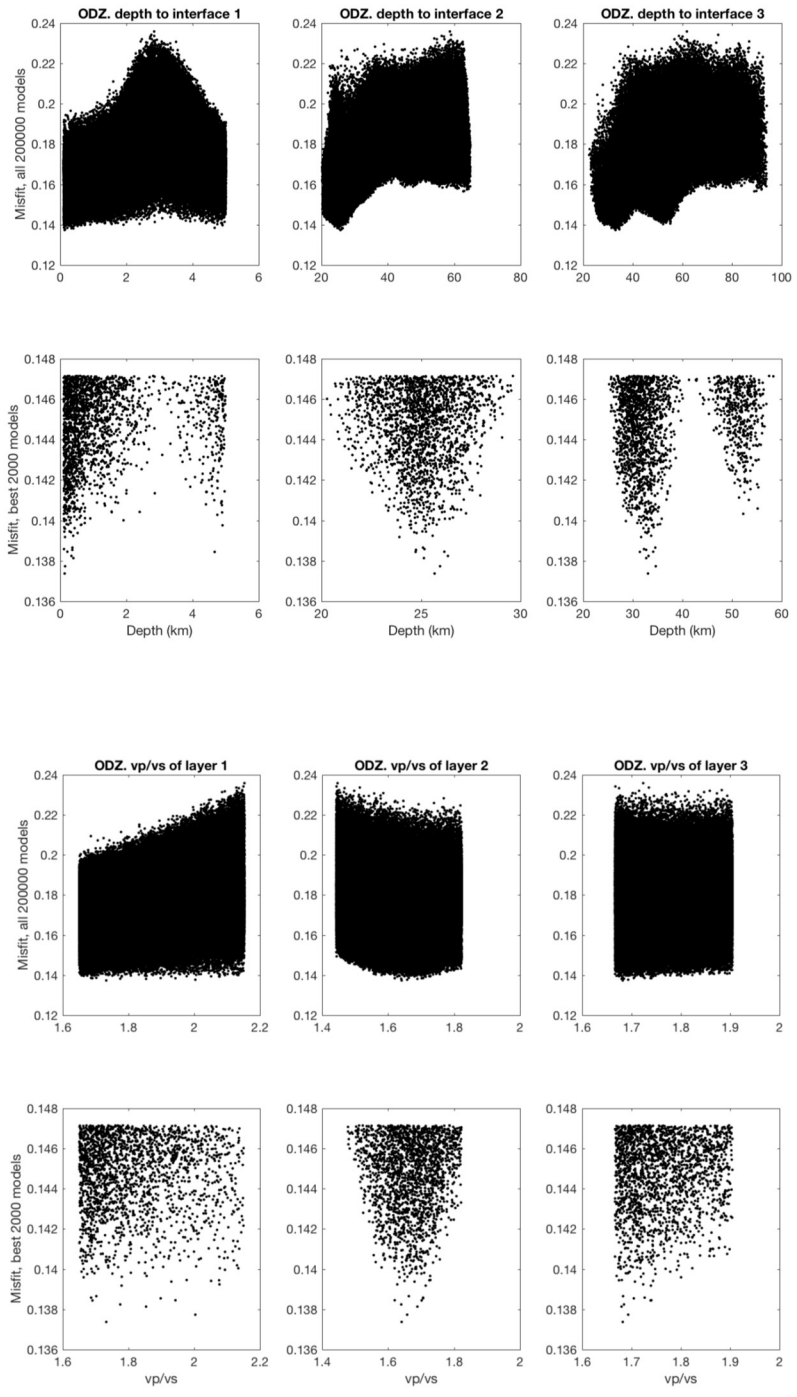

Figure 7.12: The best 2000 models for station ODZ. The best model has the following values: ***Layer 1*** *- Crustal thickness: 0.1 km;* ***Layer 2*** *- Crustal thickness: 25.5 km and Vp/Vs 1.64;* ***Layer 3*** *-Crustal thickness: 7.4 km; Misfit: 0.13.*

7.3 Summary of interpretations

Various interpretations were presented during the discussion in the sections above. Three layers were required to fit the data and these layers represent:

1. *Sediment layer* - This layer is illuminated fairly well even though it does not exactly correlate to the mapped basins. The areas that are sediment-free correspond to the Otago Schist and the Northwest Nelson. These areas also coincide with the highest magnetic values due to the lack of non-magnetic overburden. The material in the Southern Alps seems to have velocities that are expected for sedimentary rocks.
2. *Felsic crystalline crust* - The depths are spatially coherent and there is a clear signal in the Vp/Vs. The high trend in values along the centre of South Island, indicated a different lower crust composition or fluid content along the fault. This is correlated with a gravity low, which makes it hard to interpret as increased mafic content.
3. *Mafic layer* - The depth to Moho does not follow a simple pattern and the Vp/Vs follows a similar trend as layer 2 but with the highs and lows reversed. Vp/Vs is poorly recovered for this layer due to a lower sensitivity than layer 2. The crustal thickness variations across the island are fairly modest and the thickest crust is on the western edge. The scale of the cross-section in Figure 7.10, suggests that the Moho topography has a lot of short wavelength variation, therefore the lack of Moho contrast in some areas could be due to

not having enough stations or Moho topography violating the flat-layer assumption of the modelling.

Another one of the main focuses of the study was to determine if there was any variation in the crustal properties across the Alpine Fault. The results do not indicate a clear change at the Alpine Fault. However, they do indicate a clear Vp/Vs signal in the upper and mid-crust composition that follows the trend of the fault.

8 Conclusion

Crustal thickness mapping with controlled source seismic methods is expensive and difficult to cover a wide area on a continental scale. Teleseismic techniques allow mapping of depth to Moho on a large scale quickly (using archived data) and are cost effective. Through a comparison of teleseismic techniques, the transfer function approach yields significantly better results than the H-k stacking of receiver functions. In addition, avoiding deconvolution eliminates artefacts, which is important in areas where the receiver function response is noisy. This method allows the detection of sedimentary basins and resolving thickness and Vp/Vs ratio without the influence of the sedimentary layer.

In this experiment the transfer function approach was completed on 27 stations from South Island, New Zealand using over 2500 events and revealed variations of crustal thickness (depth to Moho) and Vp/Vs ratio from 20.8 – 38.4 km and 1.55 – 1.9 respectively. The results show thinner crust toward the southeast and thicker crust toward the centre of the island. In addition, the Vp/Vs ratio increases through the centre of the island and lowers towards the Alpine Fault and the southeast coastlines. Major compositional changes were not detected at the Alpine Fault, but the trends in Vp/Vs parallel to the fault are of interest. Layer thicknesses are resolved more robustly than velocity ratios. Only the crystalline basement's Vp/Vs ratio is recovered for most stations. Additional future work could include a joint inversion of receiver functions and surface waves to constrain Vs. In addition, in areas where more research has been conducted to refine the model bounds, single station modelling can be conducted to yield more robust results.

9 References

Ammon, C. J., Randall, G. E., & Zandt, G. (1990). On the nonuniqueness of receiver function inversions. *Journal of Geophysical Research: Solid Earth*, *95*(B10), 15303-15318.

Barka, A., Akyuz, H. S., Altunel, E. R. H. A. N., Sunal, G., Cakir, Z., Dikbas, A., & Page, W. (2002). The surface rupture and slip distribution of the 17 August 1999 Izmit earthquake (M 7.4), North Anatolian fault. *Bulletin of the Seismological Society of America*, *92*(1), 43-60.

Bayer, U., Scheck, M., Rabbel, W., Krawczyk, C. M., Götze, H. J., Stiller, M., & Kuder, J. (1999). An integrated study of the NE German Basin. Tectonophysics, 314(1), 285-307.

Beaumont, C., Kamp, P. J., Hamilton, J., & Fullsack, P. (1996). The continental collision zone, South Island, New Zealand: Comparison of geodynamical models and observations. *Journal of Geophysical Research: Solid Earth*, *101*(B2), 3333-3359.

Bostock, M. G. (1998). Mantle stratigraphy and evolution of the Slave province. *Journal of Geophysical Research: Solid Earth*, *103*(B9), 21183-21200.

Bourguignon, S. (2009). Lithospheric deformation at the South Island oblique collision, New Zealand.

Crotwell, H. P., T. J. Owens, and J. Ritsema (1999). The TauP Toolkit: Flexible seismic travel- time and ray-path utilities, Seismological Research Letters 70, 154–160.

Darbyshire, F. A., Eaton, D. W., Frederiksen, A. W., & Ertolahti, L. (2007). New insights into the lithosphere beneath the Superior Province from Rayleigh wave dispersion and receiver function analysis. Geophysical Journal International,169(3), 1043-1068.

Davey, F. J., Henyey, T., Holbrook, W. S., Okaya, D. A. S. T., Stern, T. A., Melhuish, A., & Christensen, N. (1998). Preliminary results from a geophysical study across a modern, continent-continent collisional plate boundary—the Southern Alps, New Zealand. *Tectonophysics*, *288*(1-4), 221-235.

Davy, R., Stern, T., & Townend, J. (2013). Gravity analysis of glaciotectonic processes, central alpine fault, South Island, New Zealand. *New Zealand Journal of Geology and Geophysics*, *56*(2), 100-108.

Dyment, J., Lesur, V., Hamoudi, M., Choi, Y., Thebault, E., Catalan, M. (2003), the WDMAM Task Force, the WDMAM Evaluators, and the WDMAM Data Providers, World Digital Magnetic Anomaly Map version 2.0, map available at http://www.wdmam.org

Eberhart-Phillips, D., & Reyners, M. (1997). Continental subduction and three-dimensional crustal structure: The northern South Island, New Zealand. *Journal of Geophysical Research: Solid Earth, 102(B6)*, 11843-11861.

Eberhart-Phillips, D., Reyners, M., Bannister, S., Chadwick, M., & Ellis, S. (2010). Establishing a versatile 3-D seismic velocity model for New Zealand. *Seismological Research Letters, 81(6),* 992-1000.

Frederiksen, A. Course Notes for GEOL 4870, Honours Thesis. University of Manitoba, 2014.

Frederiksen, A. W., & Delaney, C. (2015). Deriving crustal properties from the P Coda without deconvolution: the southwestern Superior Province, North America. Geophysical Journal International, 201(3), 1491-1506.

Frederiksen, A. W., Thompson, D. A., Rost, S., Cornwell, D. G., Gülen, L., Houseman, G. A., & Utkucu, M. (2015). Crustal thickness variations and isostatic disequilibrium across the North Anatolian Fault, western Turkey. Geophysical Research Letters, 42(3), 751-757.

Gülen, L., Pinar, A., Kalafat, D., Ozel, N., Horasan, G., Yilmazer, M., & Işikara, A. M. (2002). Surface fault breaks, aftershock distribution, and rupture process of the 17 August 1999 Izmit, Turkey, earthquake. *Bulletin of the Seismological Society of America*, *92*(1), 230-244.

Kahraman, M., Cornwell, D. G., Thompson, D. A., Rost, S., Houseman, G. A., Türkelli, N., & Gülen, L. (2015). Crustal-scale shear zones and heterogeneous structure beneath the North Anatolian Fault Zone, Turkey, revealed by a high-density seismometer array. *Earth and Planetary Science Letters*, *430*, 129-139.

Kennett, B.L.N. (Compiler and Editor). 1991. "IASPEI 1991 Seismological Tables." Bibliotech, Canberra, Australia, 167 pp.

Kleffmann, S., Davey, F., Melhuish, A., Okaya, D., Stern, T., & Sight Team. (1998). Crustal structure in the central South Island, New Zealand, from the Lake Pukaki seismic experiment. *New Zealand Journal of Geology and Geophysics*, *41*(1), 39-49.

Landes, M., O'Reilly, B. M., Readman, P. W., Shannon, P. M., & Prodehl, C. (2003). VARNET-96: three-dimensional upper crustal velocity structure of SW Ireland. Geophysical Journal International, 153(2), 424-442.

Ligorria, J. P., & Ammon, C. J. (1999). Iterative deconvolution and receiver-function estimation. *Bulletin of the seismological Society of America*, *89*(5), 1395-1400.

Lowe, C., & Cassidy, J. F. (1995). Geophysical evidence for crustal thickness variations between the Denali and Tintina fault systems in west-central Yukon. *Tectonics*, *14*(4), 909-917.

Lowrie, W. (2007): Fundamentals of Geophysics, Second Edition; Cambridge University Press, New York, 381 pages.

McCubbine, J. C., Stagpoole, V., Caratori Tontini, F., Amos, M., Smith, E., & Winefield, R. (2017). Gravity anomaly grids for the New Zealand region. New Zealand Journal of Geology and Geophysics, 60(4), 381-391.

Mohorovicic, A. (1909). Earthquake of 8 October 1909 (Potres od 8. X. 1909). Annual Report of Zagreb Meteorological Observatory; Yearly Report of the Zagreb Meteorological Observatory for the Year, 1-63.

Mortimer, N. (1993). Metamorphic zones, terranes, and Cenozoic faults in the Marlborough Schist, New Zealand. *New Zealand journal of geology and geophysics,36(3)*, 357-368.

Mortimer, N. (2000). Metamorphic discontinuities in orogenic belts: example of the garnet–biotite–albite zone in the Otago Schist, New Zealand. International journal of earth sciences, 89(2), 295-306.

Neves, F. A., & Singh, S. C. (1996). Sensitivity study of seismic reflection/refraction data. *Geophysical Journal International*, *126*(2), 470-476.

Petersen, T., Gledhill, K., Chadwick, M., Gale, N. H., & Ristau, J. (2011). The New Zealand national seismograph network. *Seismological Research Letters*, *82*(1), 9-20.

Prodehl, C., Kennett, B., Artemieva, I. M., & Thybo, H. (2013). 100 years of seismic research on the Moho. *Tectonophysics*, *609*, 9-44.

Reilly, W. I. (1972). New Zealand gravity map series. *New Zealand journal of geology and geophysics*, *15*(1), 3-15.

Rost, S., & Thomas, C. (2009). Improving seismic resolution through array processing techniques. Surveys in geophysics, 30(4-5), 271-299.

Salmon, M., Kennett, B. L. N., Stern, T., & Aitken, A. R. A. (2013). The Moho in Australia and New Zealand. *Tectonophysics*, 609, 288-298.

Spasojević, S., & Clayton, R. W. (2005). Crustal structure and apparent tectonic underplating from receiver function analysis in South Island, New Zealand. Journal of Geophysical Research: Solid Earth, 113(B4).

Steinhart, J.S., 1967. Mohorovičić-discontinuity. In: Runcorn, K. (Ed.), Int. Dictionary of Geophysics, 2, pp. 991–994.

Thybo, H., Artemieva, I. M., & Kennett, B. (2013). Moho: 100 years after Andrija Mohorovičić. *Tectonophysics*, *609*, 1-8.

Van Avendonk, H. J., Holbrook, W. S., Okaya, D., Austin, J. K., Davey, F., & Stern, T. (2004). Continental crust under compression: A seismic refraction study of South

Island Geophysical Transect I, South Island, New Zealand. *Journal of Geophysical Research: Solid Earth, 109(B6).*

Walcott, R. I. (1998). Modes of oblique compression: Late Cenozoic tectonics of the South Island of New Zealand. *Reviews of geophysics*, *36*(1), 1-26.

Wannamaker, P. E., Jiracek, G. R., Stodt, J. A., Caldwell, T. G., Gonzalez, V. M., McKnight, J. D., & Porter, A. D. (2002). Fluid generation and pathways beneath an active compressional orogen, the New Zealand Southern Alps, inferred from magnetotelluric data. *Journal of Geophysical Research: Solid Earth, 107(B6).*

Zhu, L., & Kanamori, H. (2000). Moho depth variation in southern California from teleseismic receiver functions. Journal of Geophysical Research: Solid Earth (1978– 2012), 105(B2), 2969-2980.

10 Appendix A: Transfer Function Analysis Results

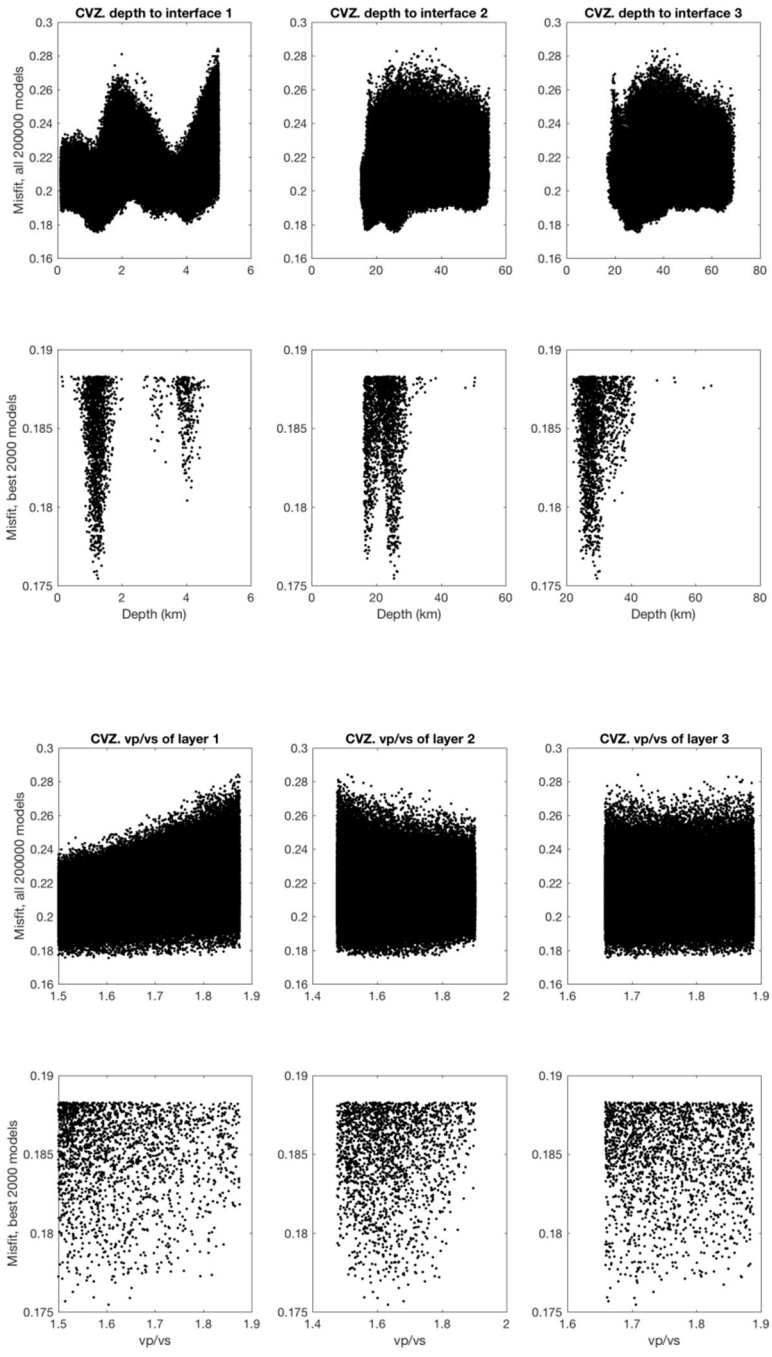

Figure 10.1: The best 2000 models for station CVZ. The best model has the following values: ***Layer 1*** *- Crustal thickness: 1.3 km;* ***Layer 2*** *- Crustal thickness: 24.2 km and Vp/Vs 1.63;* ***Layer 3*** *-Crustal thickness: 4.0 km; Misfit: 0.18.*

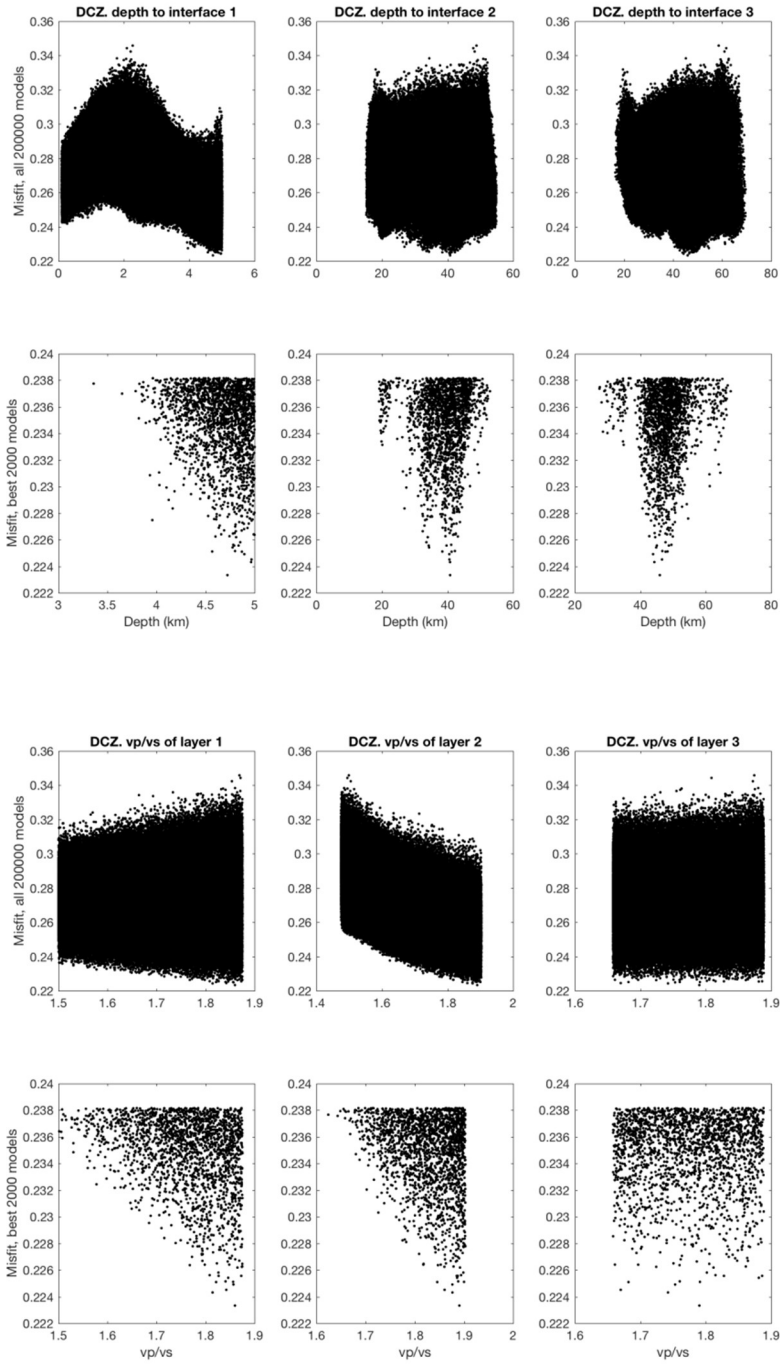

Figure 10.2: The best 2000 models for station DCZ. The best model has the following values: ***Layer 1*** *- Crustal thickness: 4.7 km;* ***Layer 2*** *- Crustal thickness: 36.1 km and Vp/Vs 1.89;* ***Layer 3*** *-Crustal thickness: 5.2 km; Misfit: 0.22.*

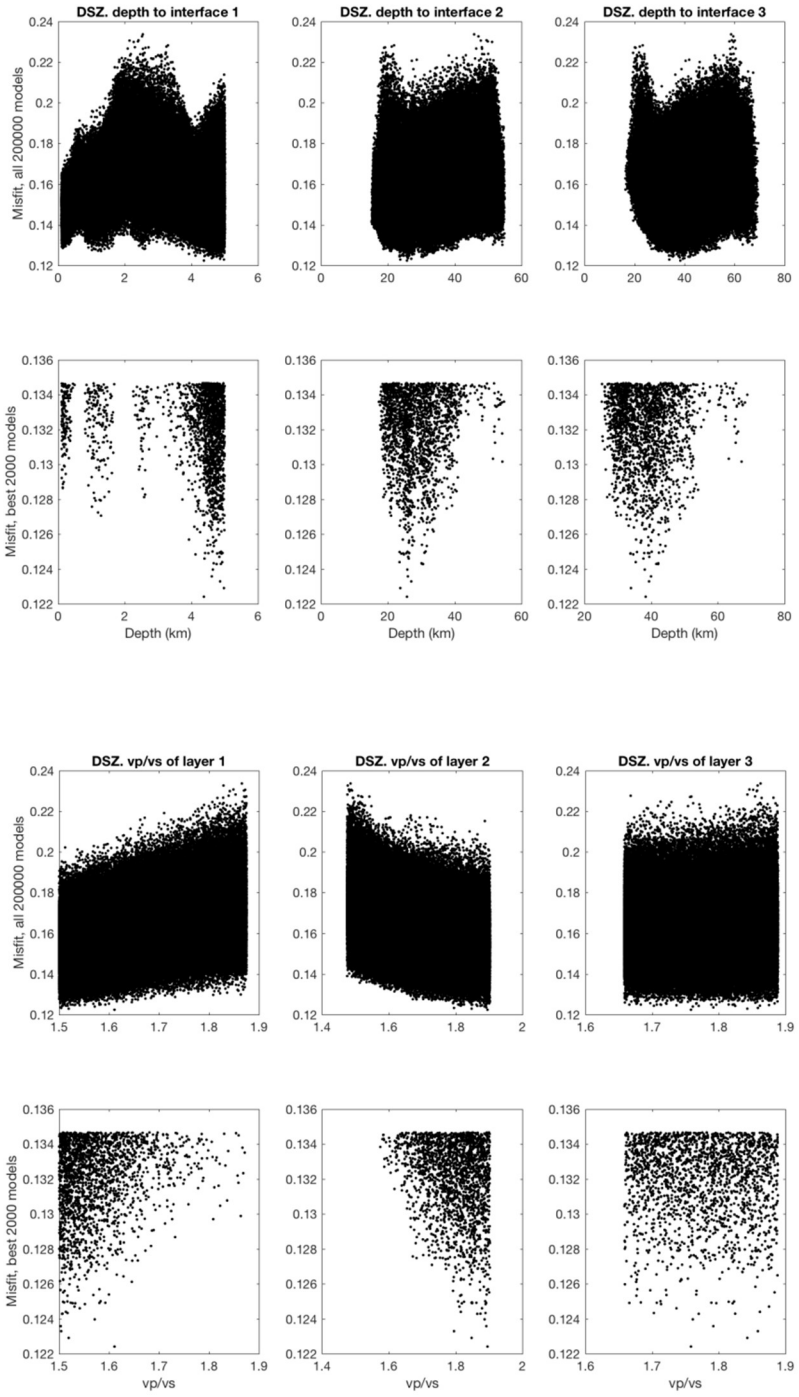

Figure 10.3: The best 2000 models for station DSZ. The best model has the following values: ***Layer 1*** *- Crustal thickness: 4.4 km;* ***Layer 2*** *- Crustal thickness: 21.3 km and Vp/Vs 1.90;* ***Layer 3*** *-Crustal thickness: 12.7 km; Misfit: 0.12.*

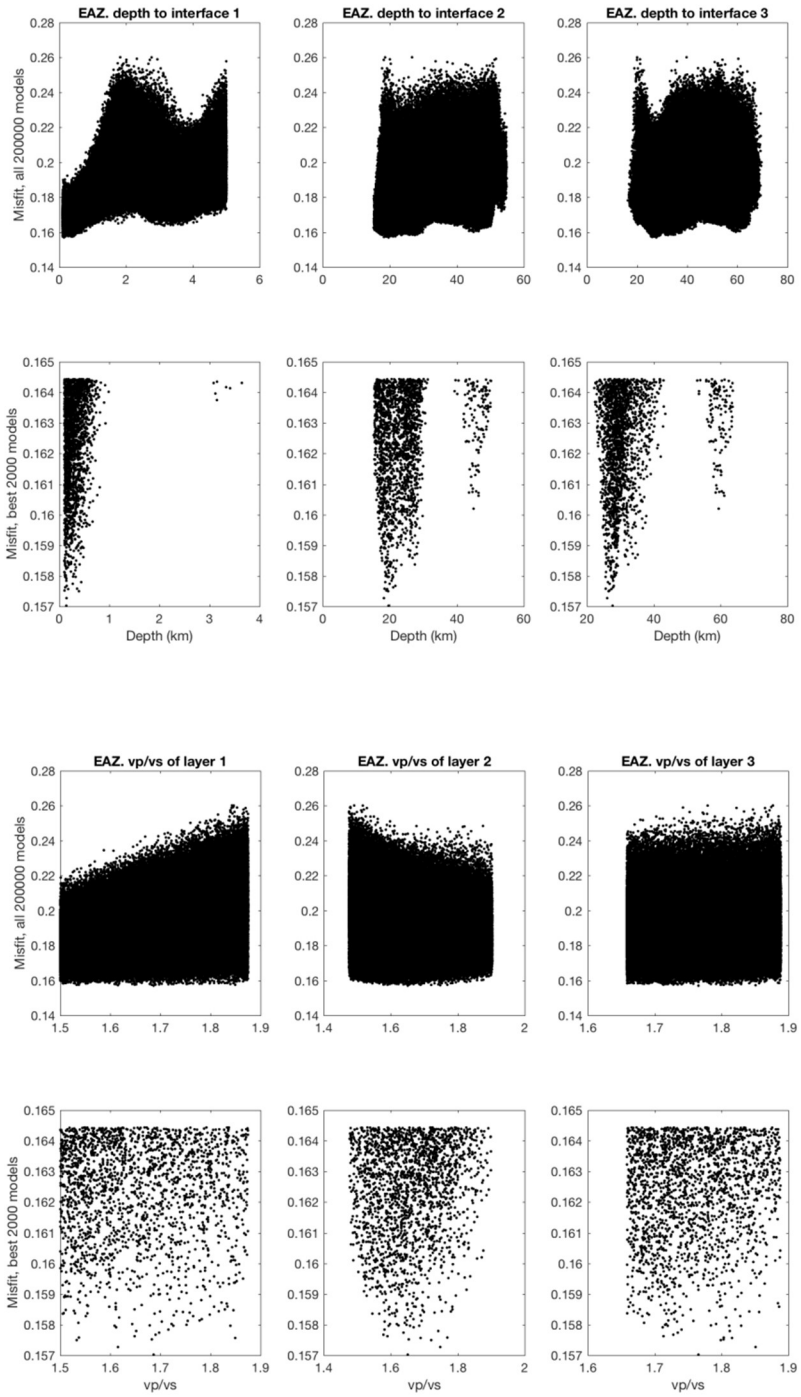

Figure 10.4: The best 2000 models for station EAZ. The best model has the following values: ***Layer 1*** *- Crustal thickness: 0.1 km;* ***Layer 2*** *- Crustal thickness: 19.5 km and Vp/Vs 1.65;* ***Layer 3*** *-Crustal thickness: 8.1 km; Misfit: 0.16.*

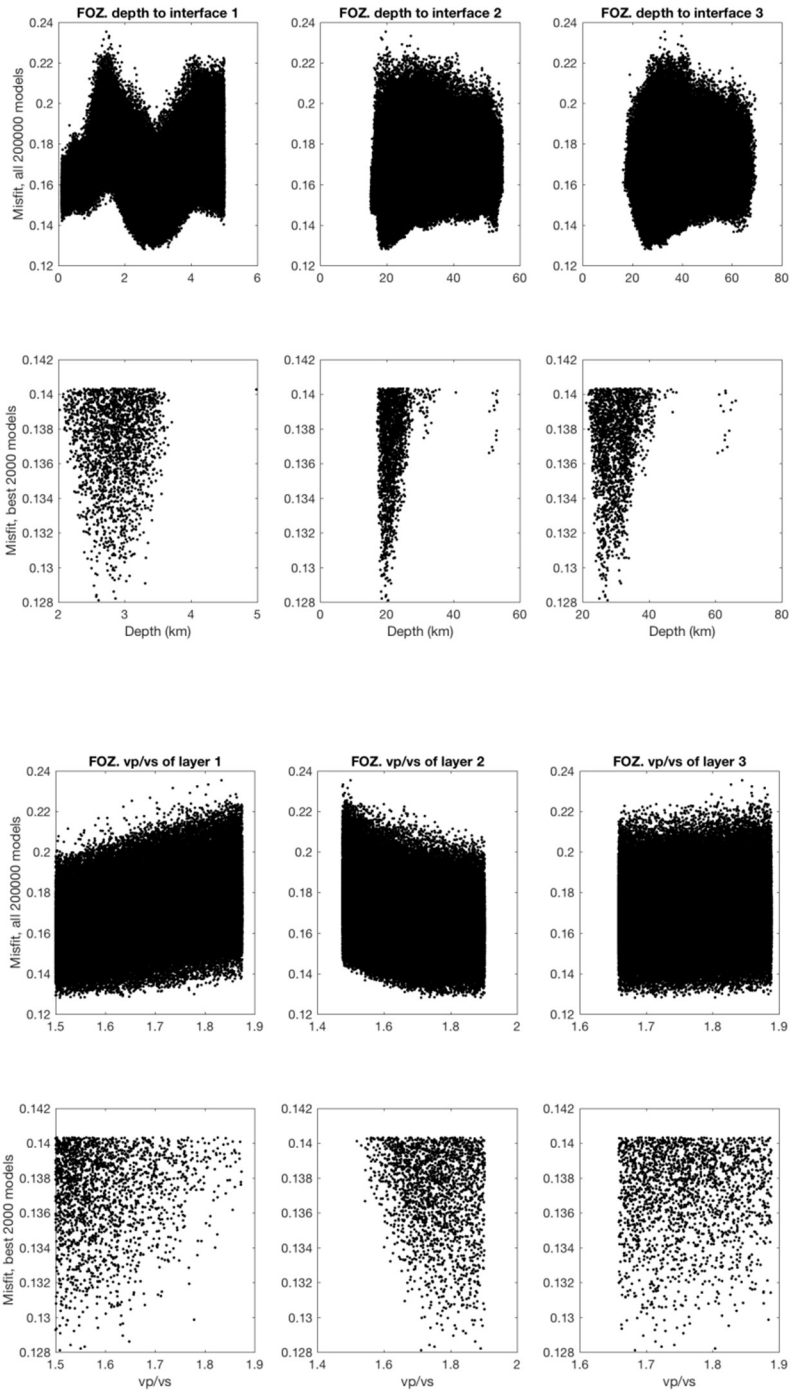

Figure 10.5: The best 2000 models for station FOZ. The best model has the following values: ***Layer 1*** *- Crustal thickness: 2.6 km;* ***Layer 2*** *- Crustal thickness: 17.8 km and Vp/Vs 1.71;* ***Layer 3*** *-Crustal thickness: 7.1 km; Misfit: 0.13.*

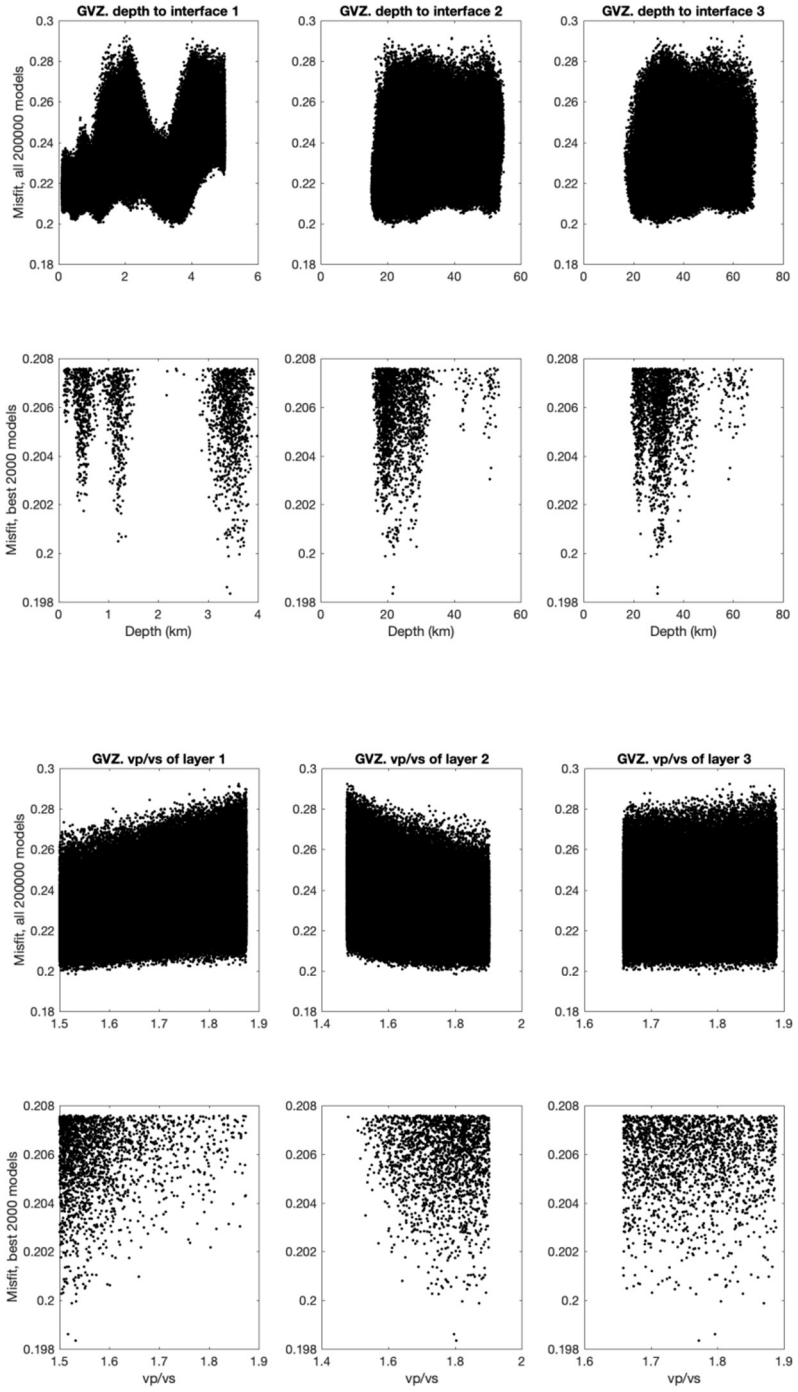

Figure 10.6: The best 2000 models for station GVZ. The best model has the following values: ***Layer 1*** *- Crustal thickness: 3.4 km;* ***Layer 2*** *- Crustal thickness: 18.1 km and Vp/Vs 1.80;* ***Layer 3*** *-Crustal thickness: 8.1 km; Misfit: 0.20.*

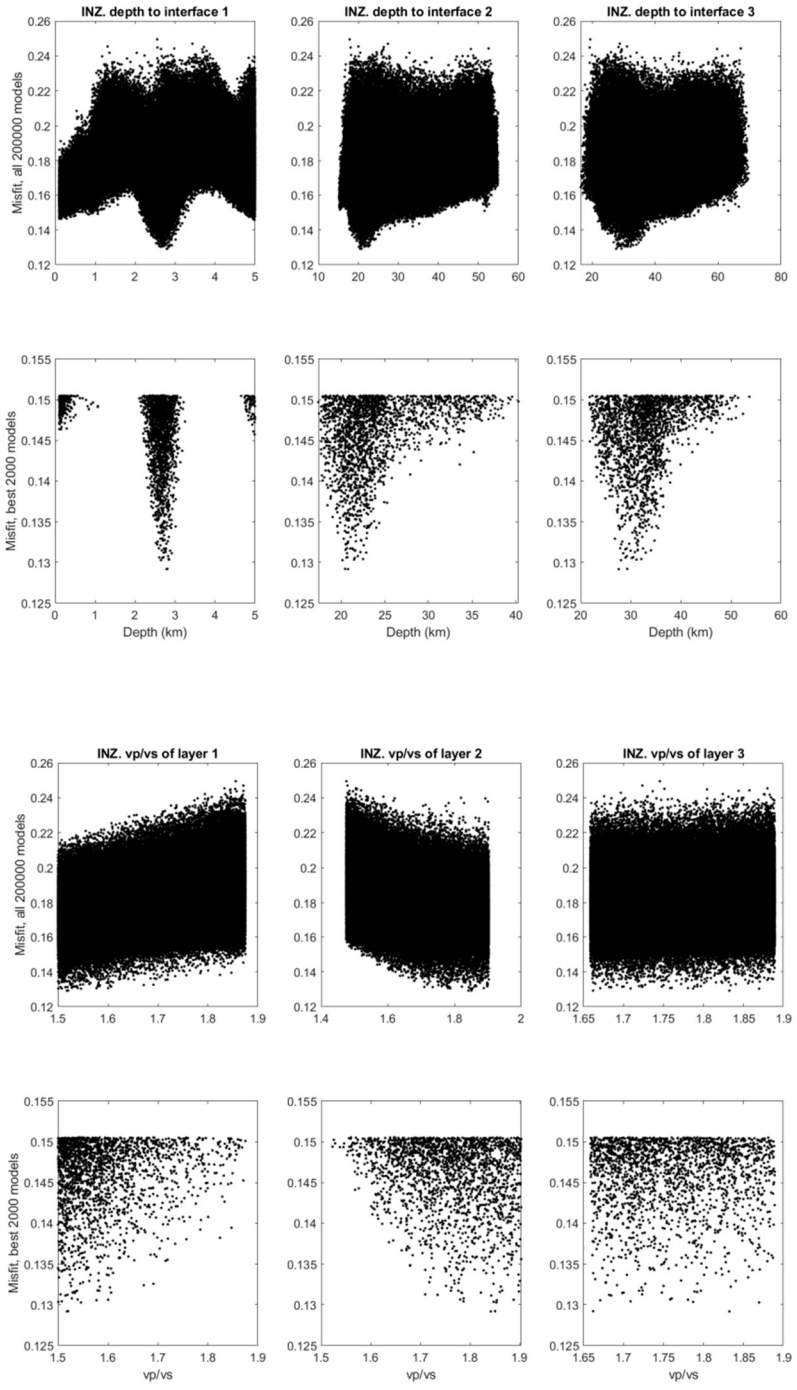

Figure 10.7: The best 2000 models for station INZ. The best model has the following values: ***Layer 1*** *- Crustal thickness: 2.8 km;* ***Layer 2*** *- Crustal thickness: 18.0 km and Vp/Vs 1.84;* ***Layer 3*** *-Crustal thickness: 6.8 km; Misfit: 0.13.*

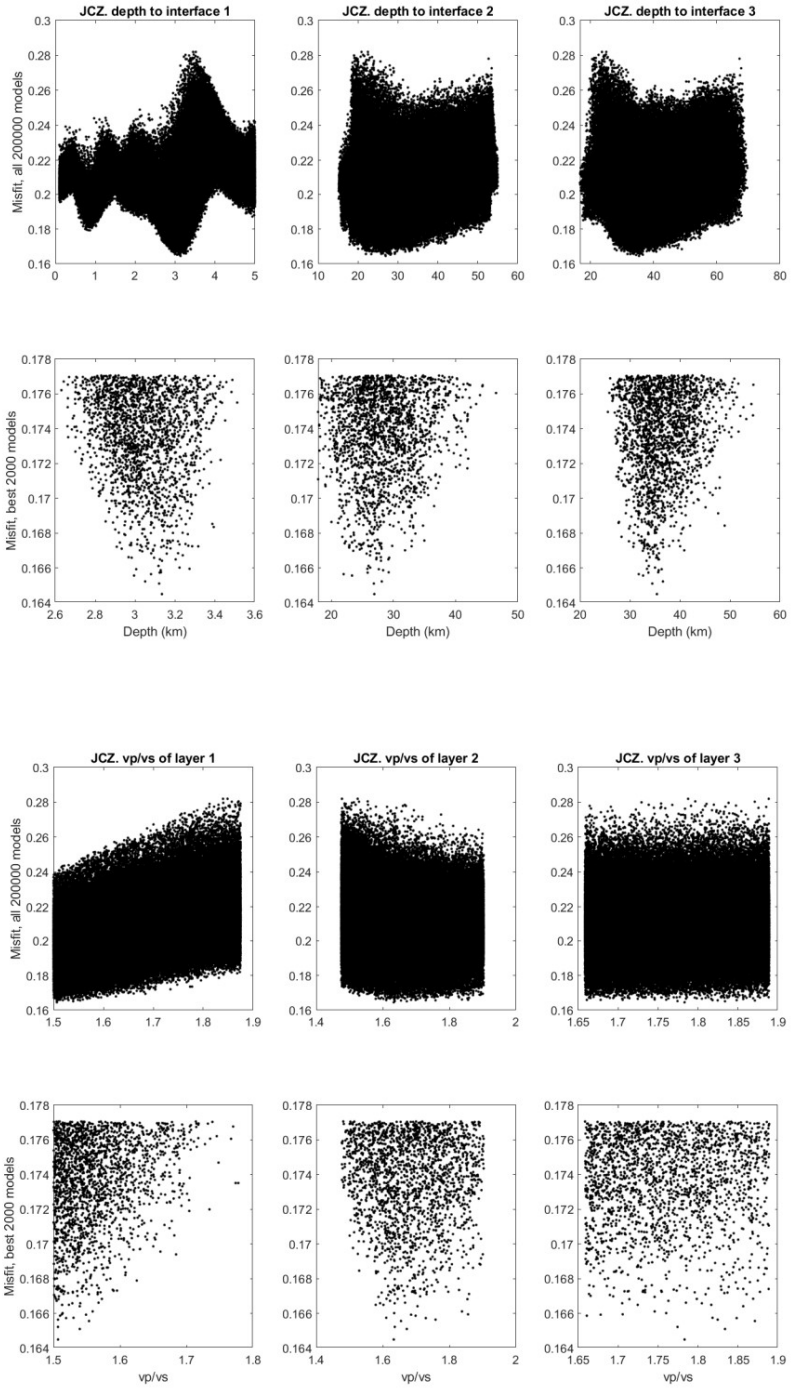

Figure 10.8: The best 2000 models for station JCZ. The best model has the following values: ***Layer 1*** *- Crustal thickness: 3.1 km;* ***Layer 2*** *- Crustal thickness: 23.8 km and Vp/Vs 1.63;* ***Layer 3*** *-Crustal thickness: 8.5 km; Misfit: 0.16.*

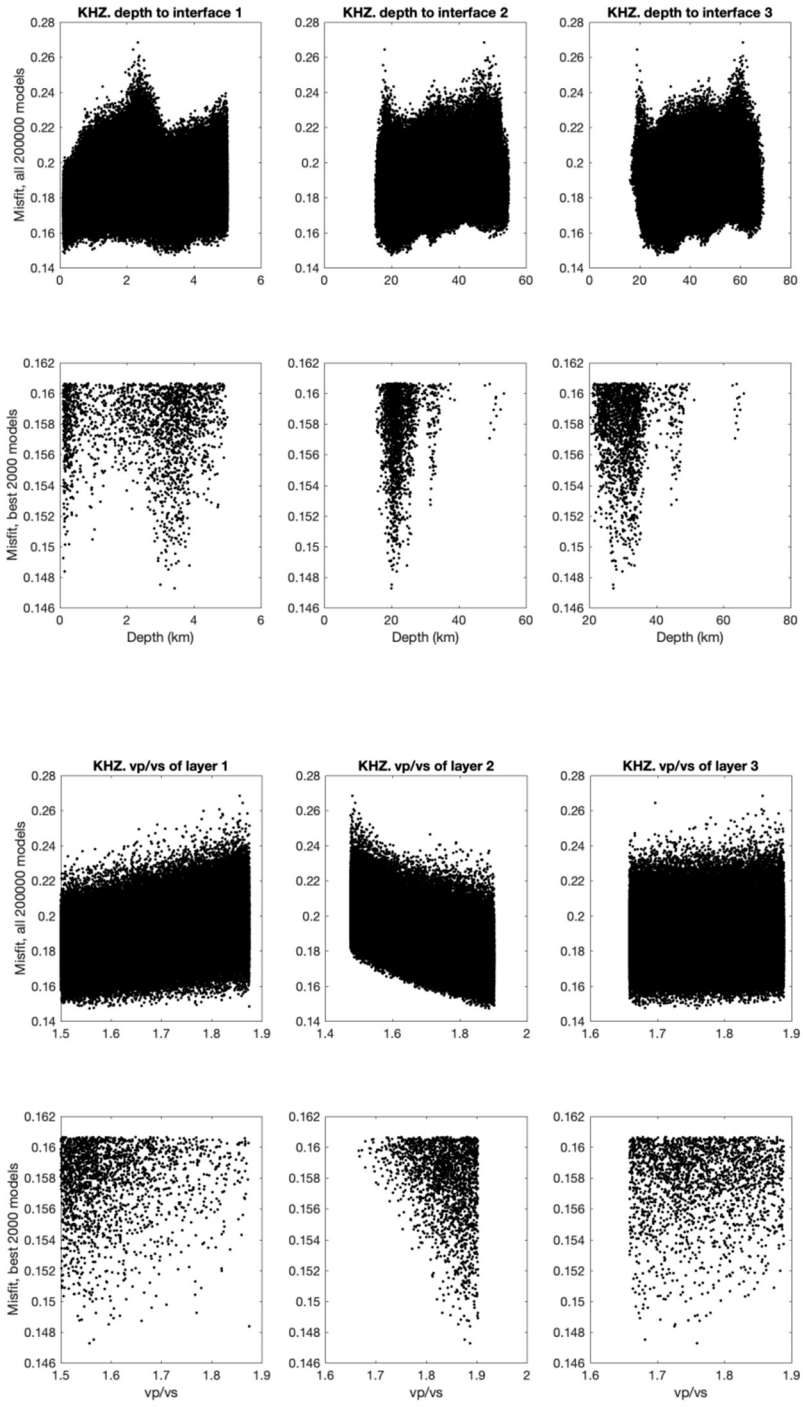

Figure 10.9: The best 2000 models for station KHZ. The best model has the following values: ***Layer 1*** *- Crustal thickness: 3.4 km;* ***Layer 2*** *- Crustal thickness: 16.5 km and Vp/Vs 1.89;* ***Layer 3*** *-Crustal thickness: 7.3 km; Misfit: 0.15.*

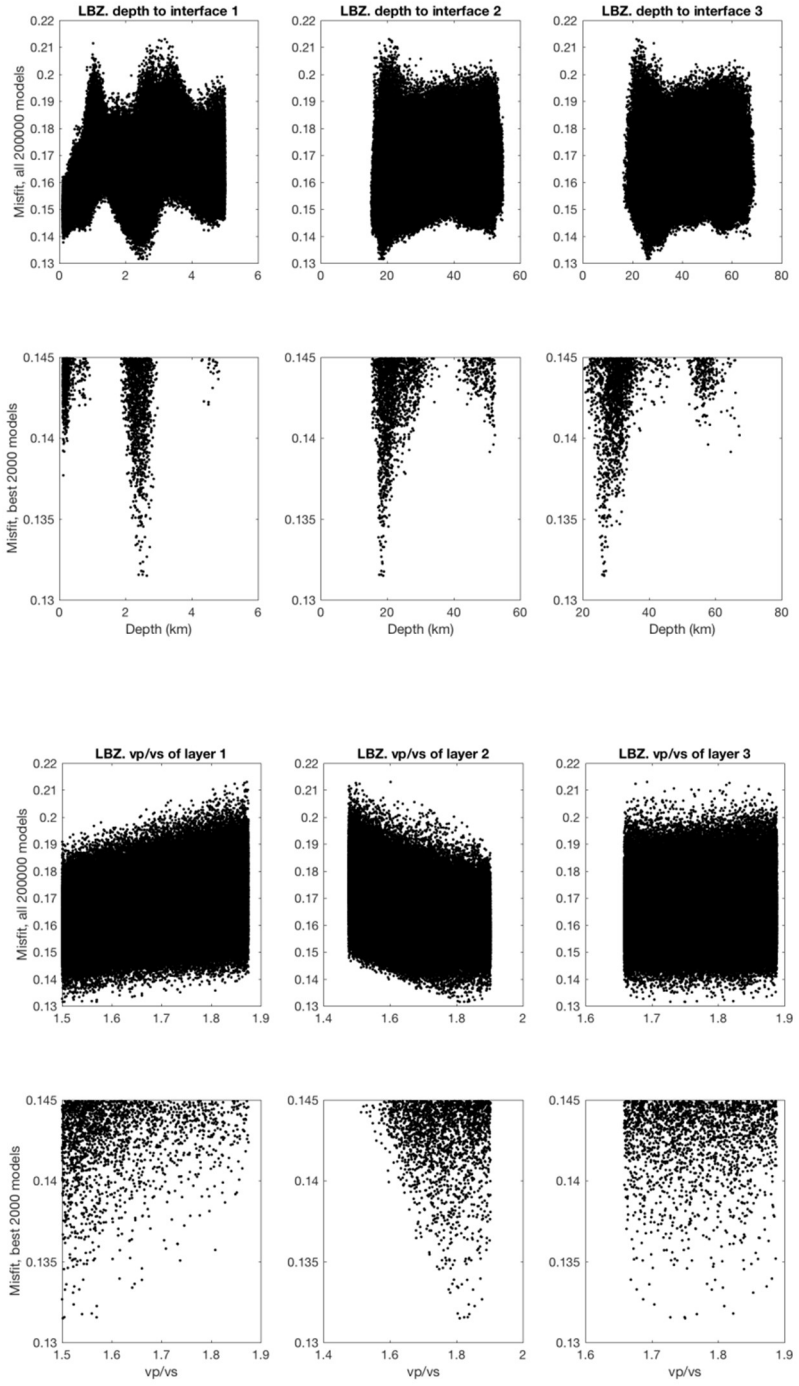

Figure 10.10: The best 2000 models for station LBZ. The best model has the following values: ***Layer 1*** *- Crustal thickness: 2.6 km;* ***Layer 2*** *- Crustal thickness: 16.1 km and Vp/Vs 1.81;* ***Layer 3*** *-Crustal thickness: 7.7 km; Misfit: 0.13.*

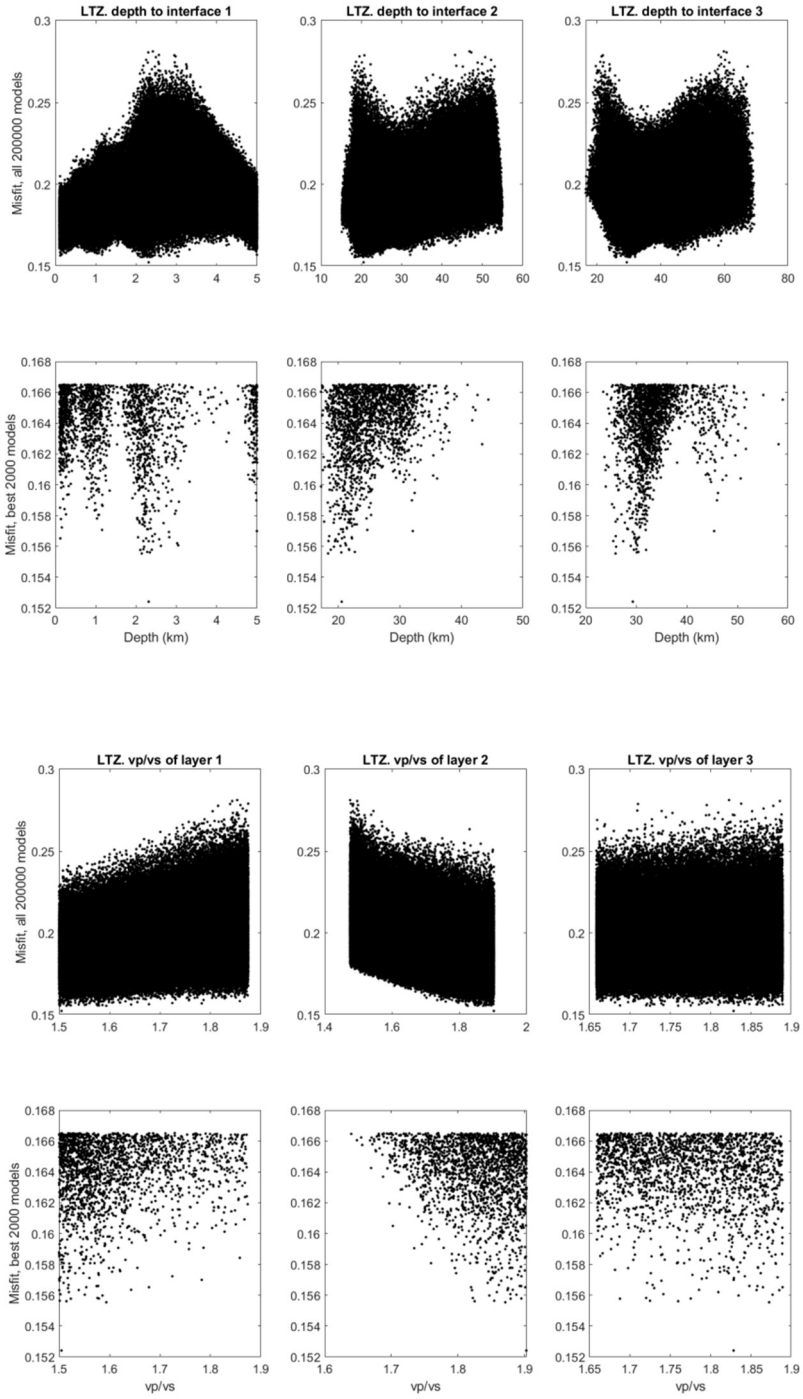

Figure 10.11: The best 2000 models for station LTZ. The best model has the following values: ***Layer 1*** *- Crustal thickness: 2.3 km;* ***Layer 2*** *- Crustal thickness: 18.3 km and Vp/Vs 1.90;* ***Layer 3*** *-Crustal thickness: 8.7 km; Misfit: 0.15.*

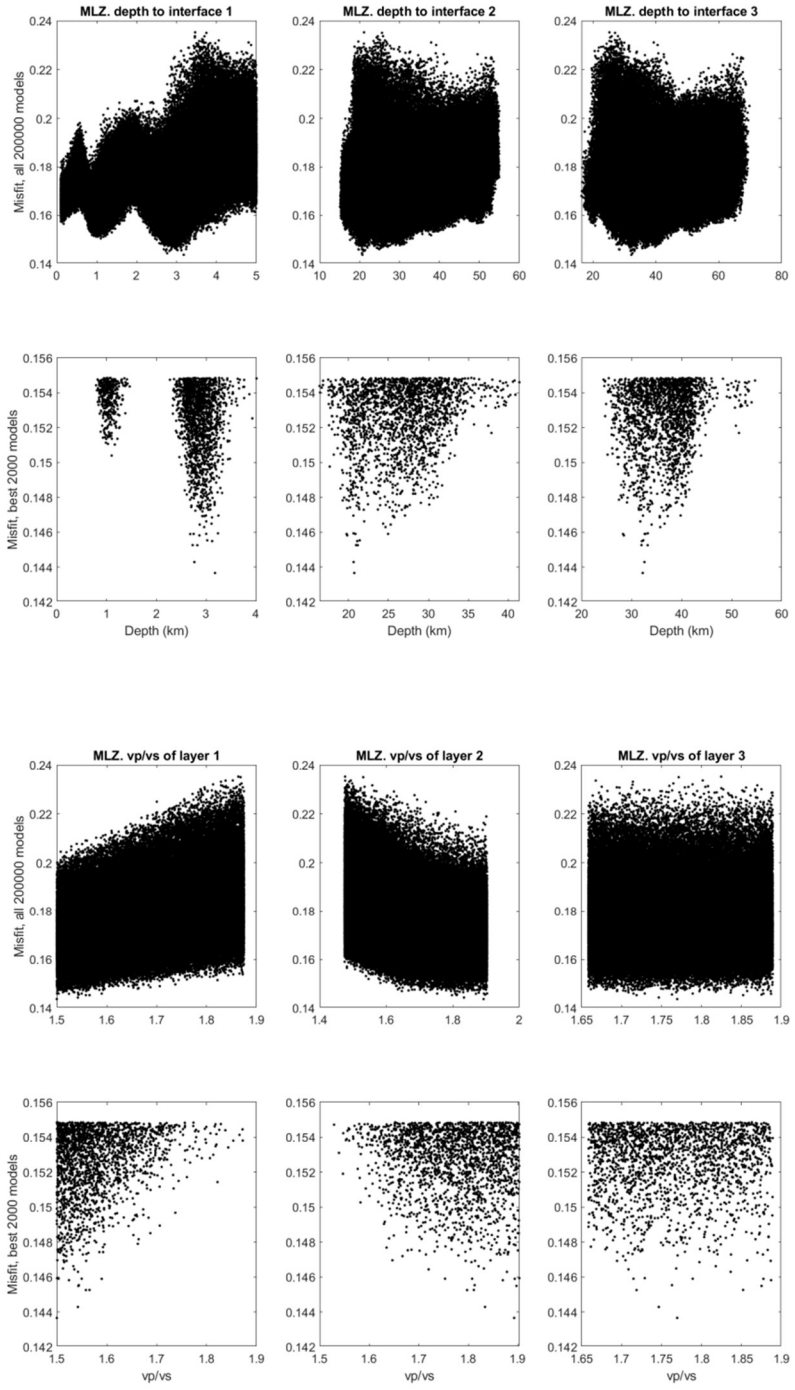

Figure 10.12: The best 2000 models for station MLZ. The best model has the following values: ***Layer 1*** *- Crustal thickness: 3.2 km;* ***Layer 2*** *- Crustal thickness: 17.5km and Vp/Vs 1.89;* ***Layer 3*** *-Crustal thickness: 11.5 km; Misfit: 0.14.*

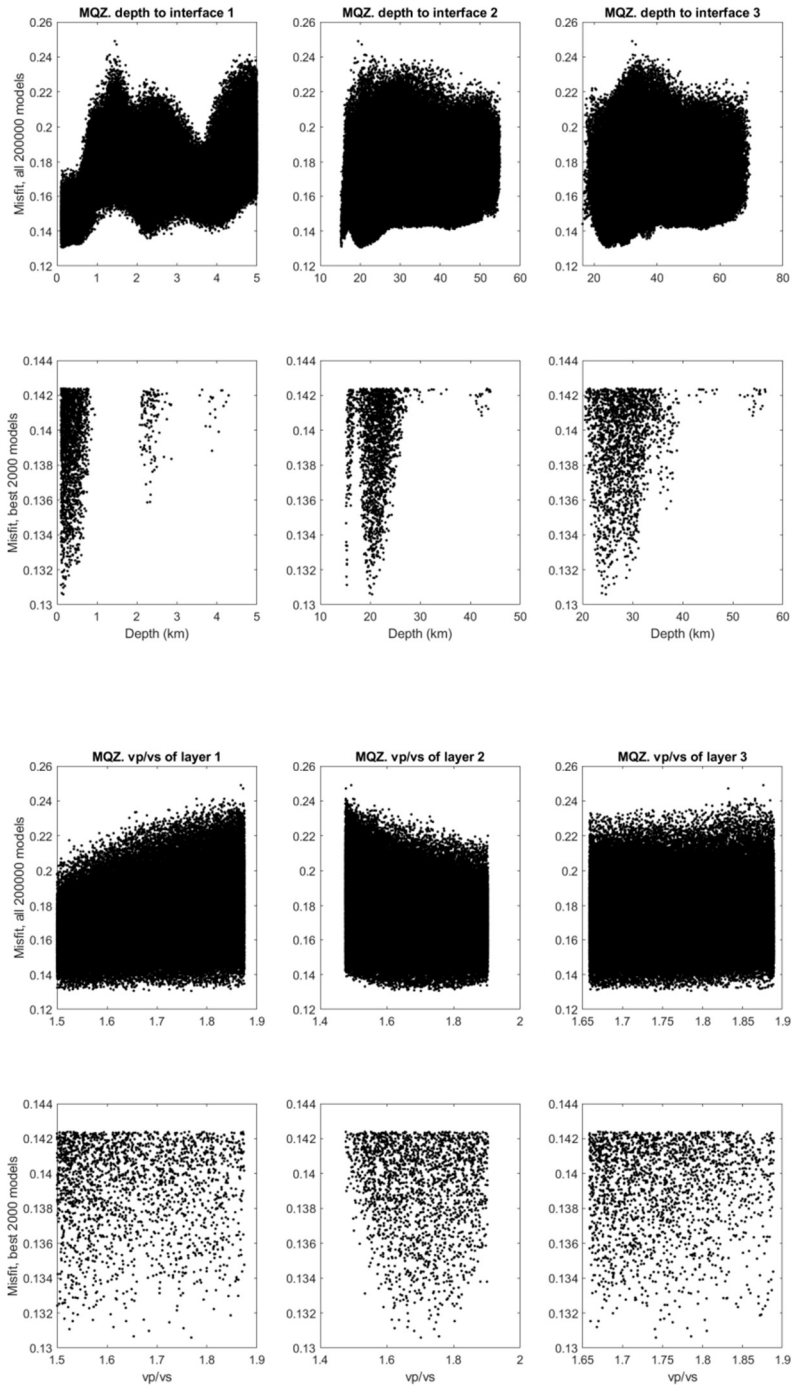

Figure 10.13: The best 2000 models for station MQZ. The best model has the following values: ***Layer 1*** *- Crustal thickness: 0.2 km;* ***Layer 2*** *- Crustal thickness: 20.2 km and Vp/Vs 1.70;* ***Layer 3*** *-Crustal thickness: 4.3 km; Misfit: 0.13.*

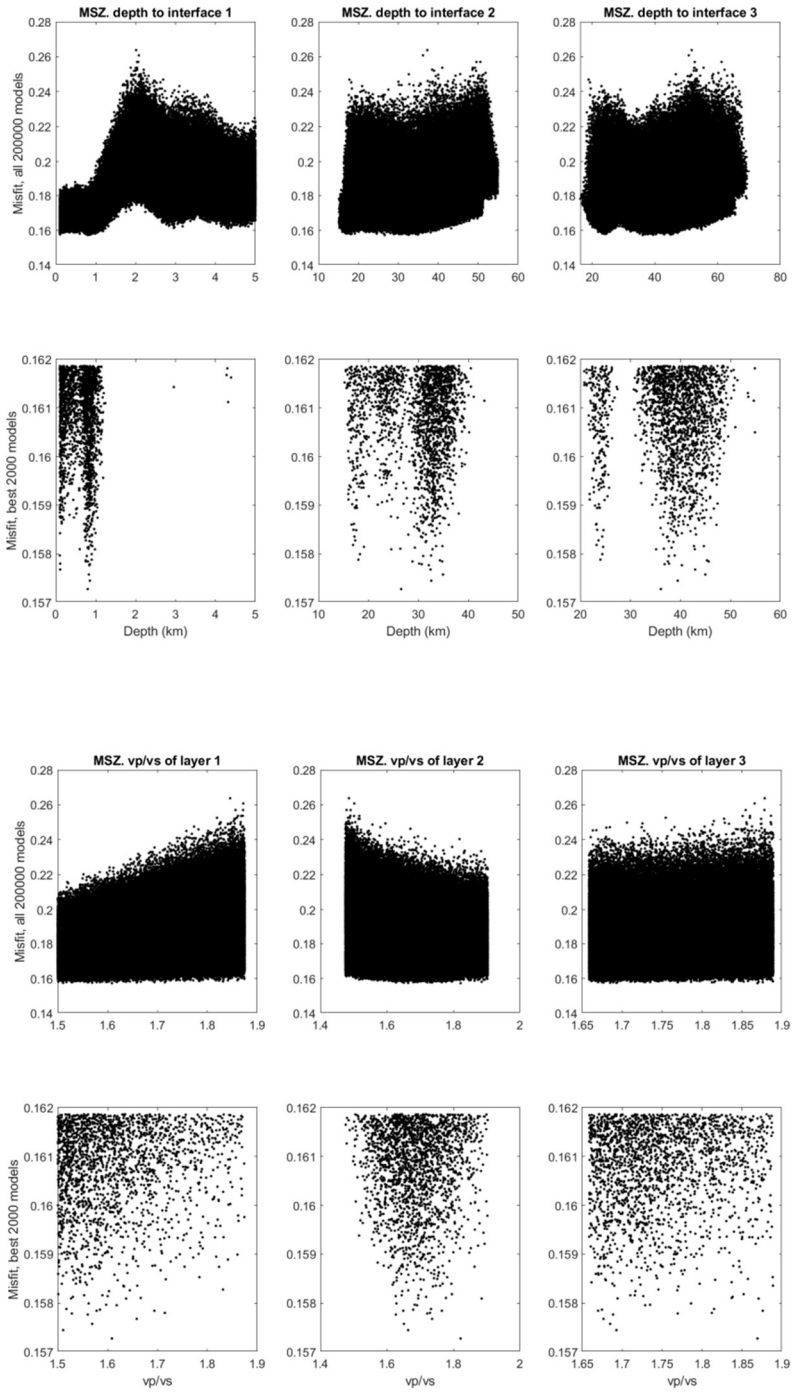

Figure 10.14: The best 2000 models for station MSZ. The best model has the following values: ***Layer 1*** *- Crustal thickness: 0.8 km;* ***Layer 2*** *- Crustal thickness: 25.8 km and Vp/Vs 1.82;* ***Layer 3*** *-Crustal thickness: 9.6 km; Misfit: 0.16.*

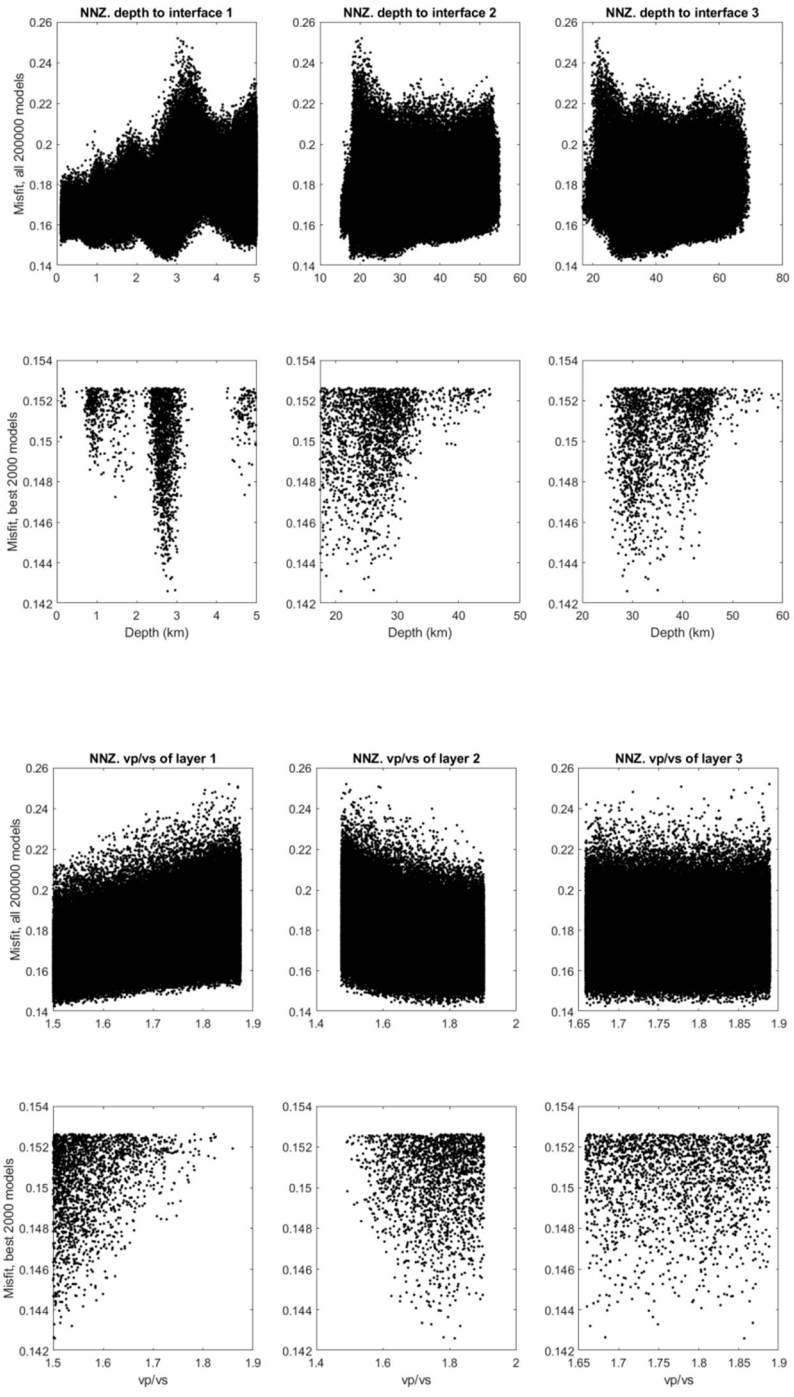

Figure 10.15: The best 2000 models for station NNZ. The best model has the following values: ***Layer 1*** *- Crustal thickness: 2.8 km;* ***Layer 2*** *- Crustal thickness: 18.1 km and Vp/Vs 1.82;* ***Layer 3*** *-Crustal thickness: 8.1 km; Misfit: 0.14.*

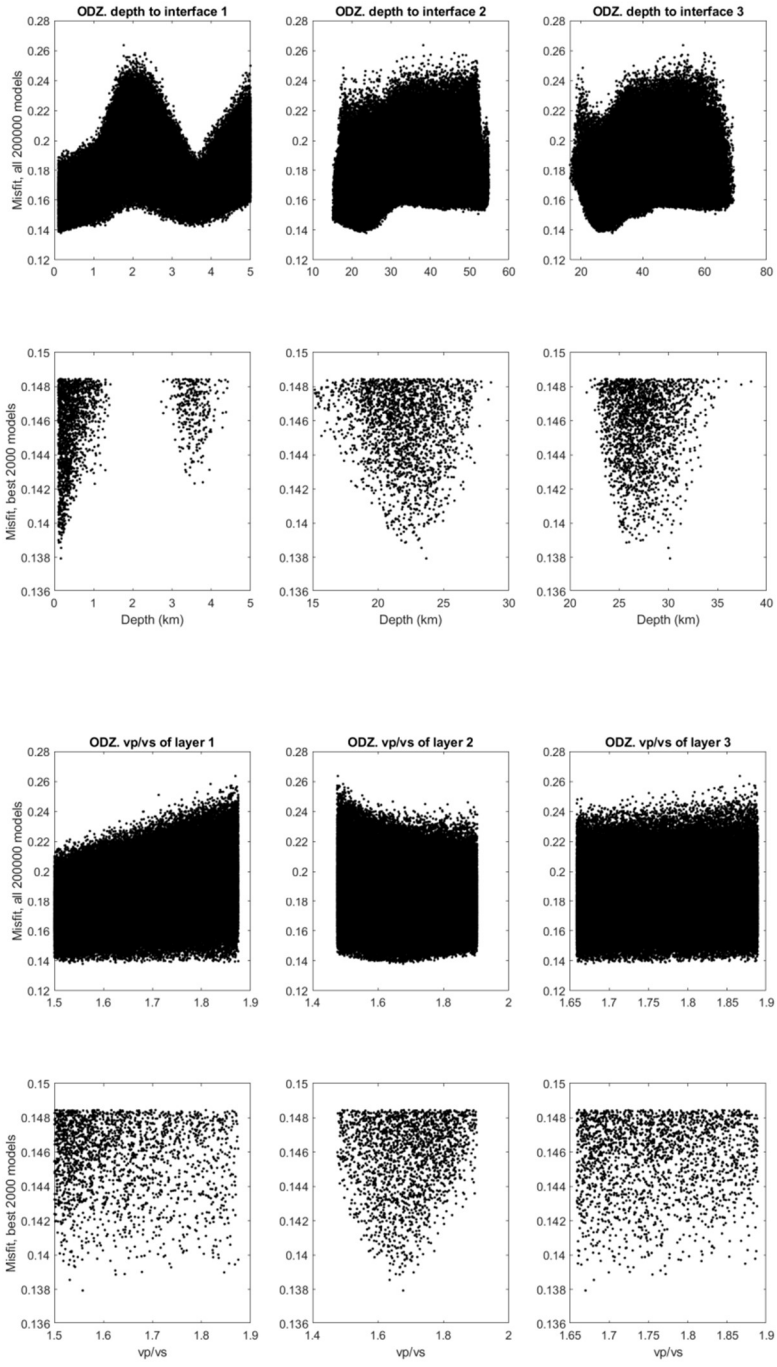

Figure 10.16: The best 2000 models for station ODZ. The best model has the following values: ***Layer 1*** *- Crustal thickness: 0.2 km;* ***Layer 2*** *- Crustal thickness: 23.5 km and Vp/Vs 1.68;* ***Layer 3*** *-Crustal thickness: 6.5 km; Misfit: 0.14.*

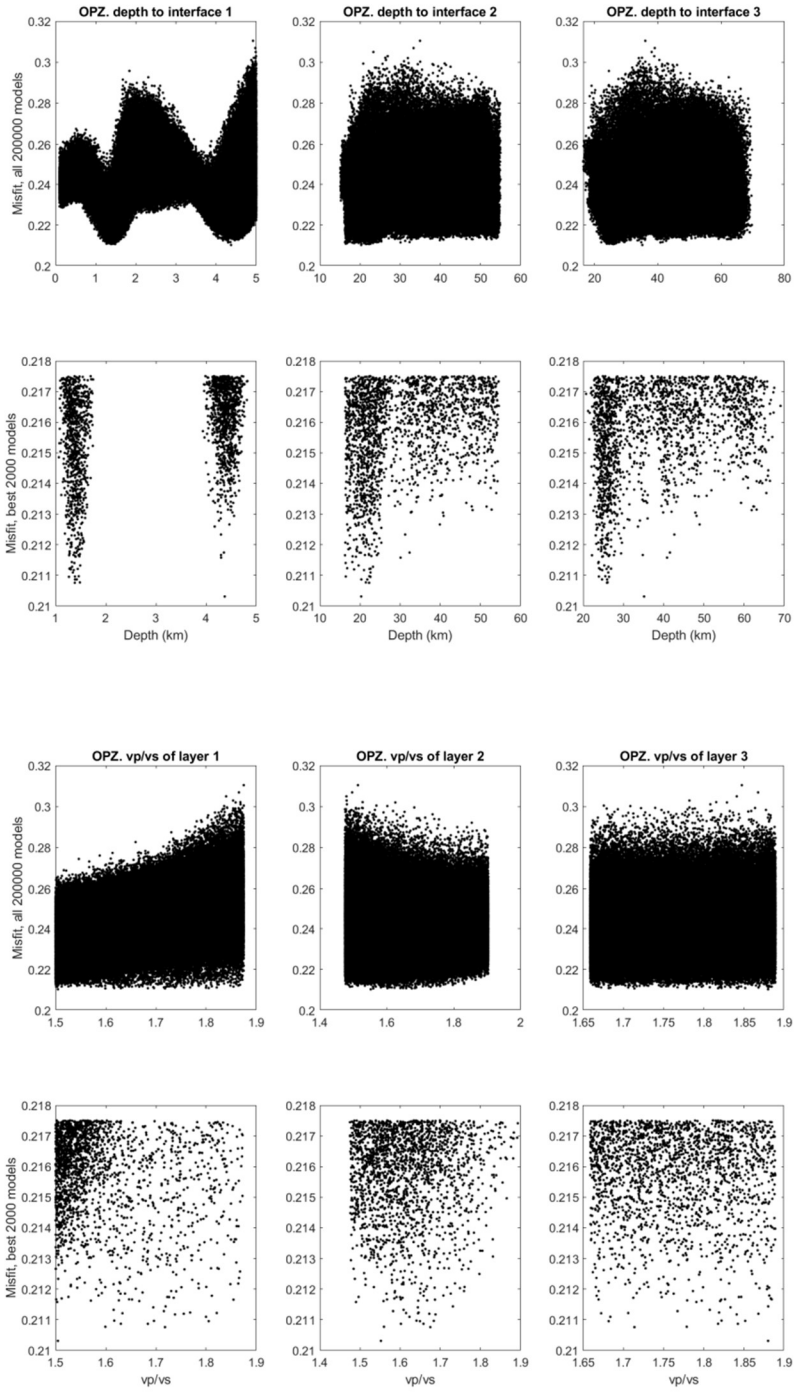

Figure 10.17: The best 2000 models for station OPZ. The best model has the following values: ***Layer 1*** *- Crustal thickness: 4.4 km;* ***Layer 2*** *- Crustal thickness: 15.9 km and Vp/Vs 1.55;* ***Layer 3*** *-Crustal thickness: 14.8 km; Misfit: 0.21.*

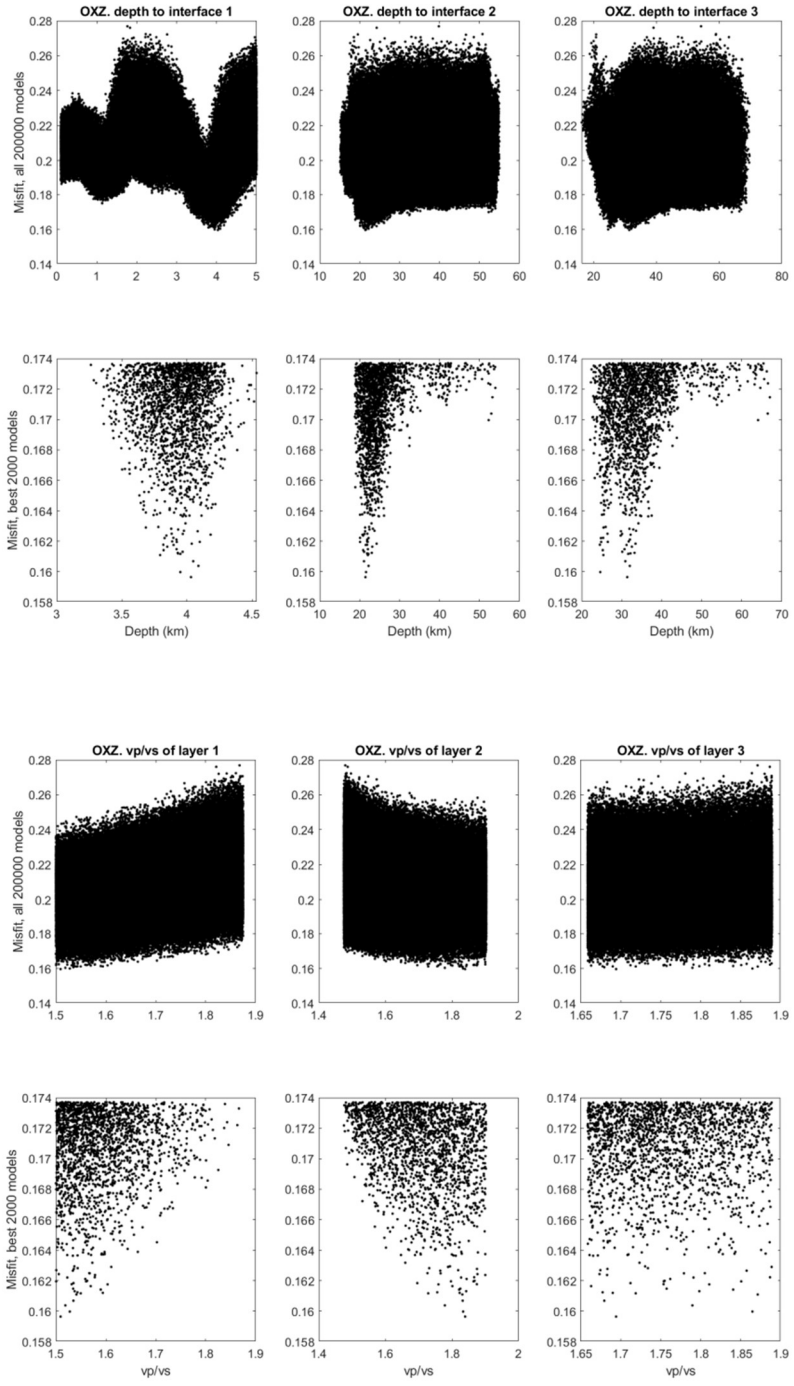

Figure 10.18: The best 2000 models for station OXZ. The best model has the following values: ***Layer 1*** *- Crustal thickness: 4.0 km;* ***Layer 2*** *- Crustal thickness: 17.4 km and Vp/Vs 1.84;* ***Layer 3*** *-Crustal thickness: 9.9 km; Misfit: 0.16.*

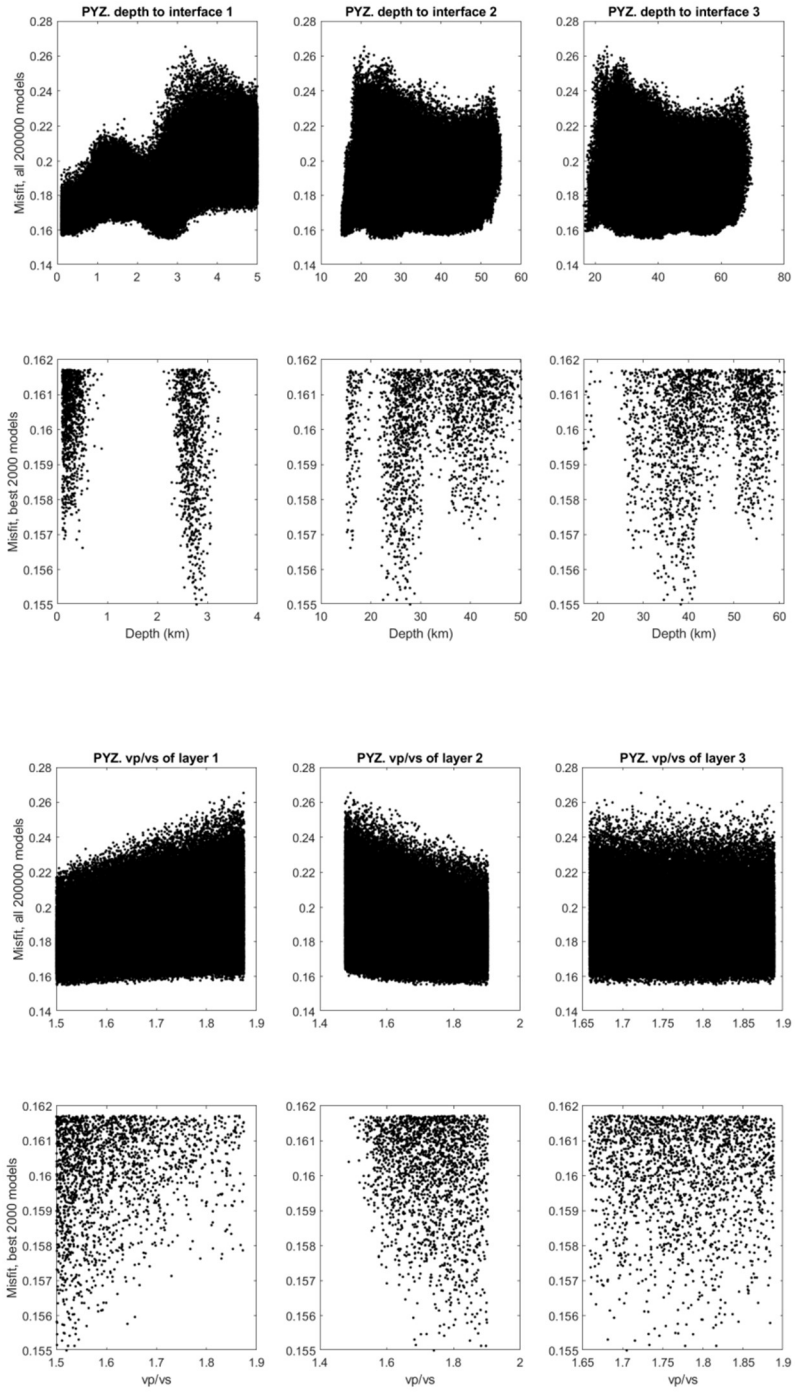

Figure 10.19: The best 2000 models for station PYZ. The best model has the following values: ***Layer 1*** *- Crustal thickness: 2.8 km;* ***Layer 2*** *- Crustal thickness: 25.1 km and Vp/Vs 1.74;* ***Layer 3*** *-Crustal thickness: 10.4 km; Misfit: 0.16.*

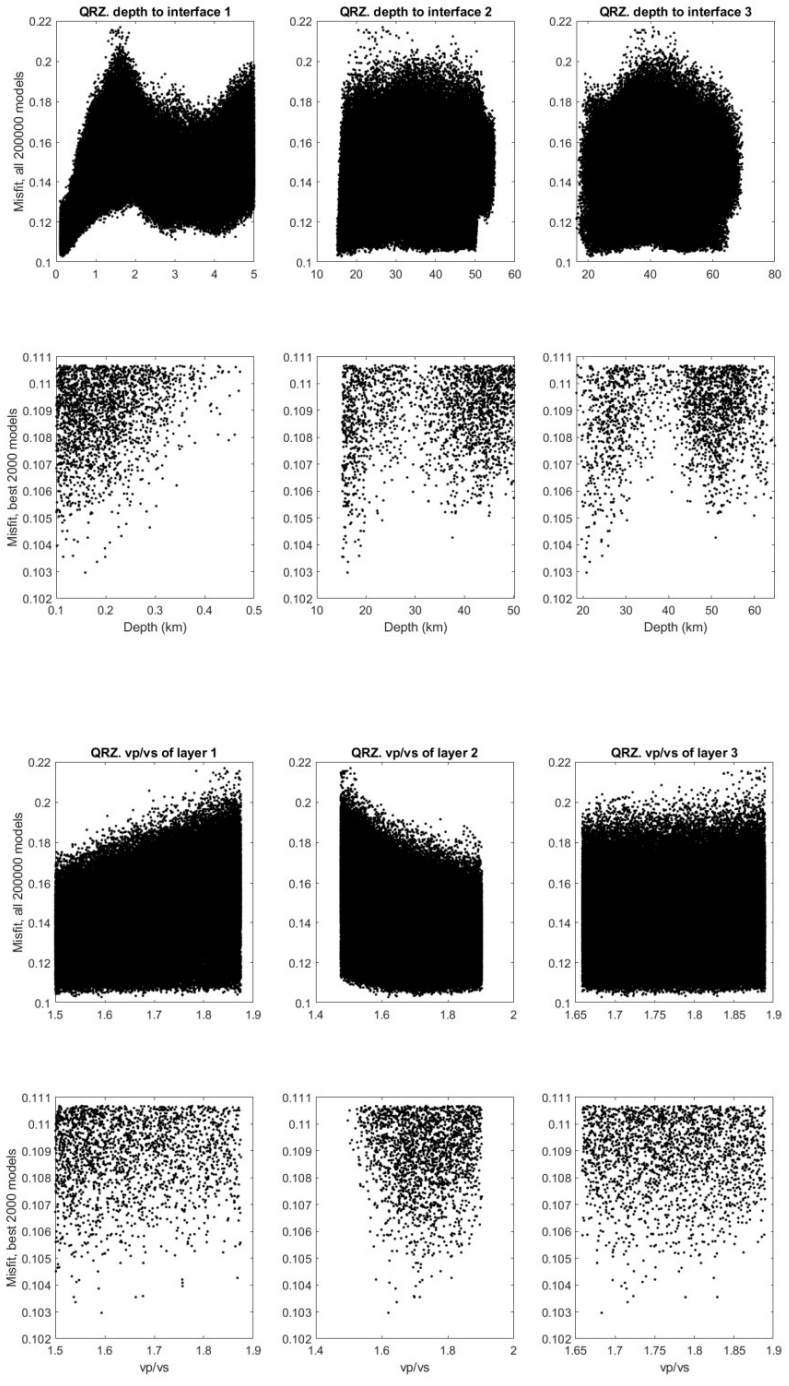

Figure 10.20: The best 2000 models for station QRZ. The best model has the following values: ***Layer 1*** *- Crustal thickness: 0.2 km;* ***Layer 2*** *- Crustal thickness: 16.1 km and Vp/Vs 1.62;* ***Layer 3*** *-Crustal thickness: 4.6 km; Misfit: 0.10.*

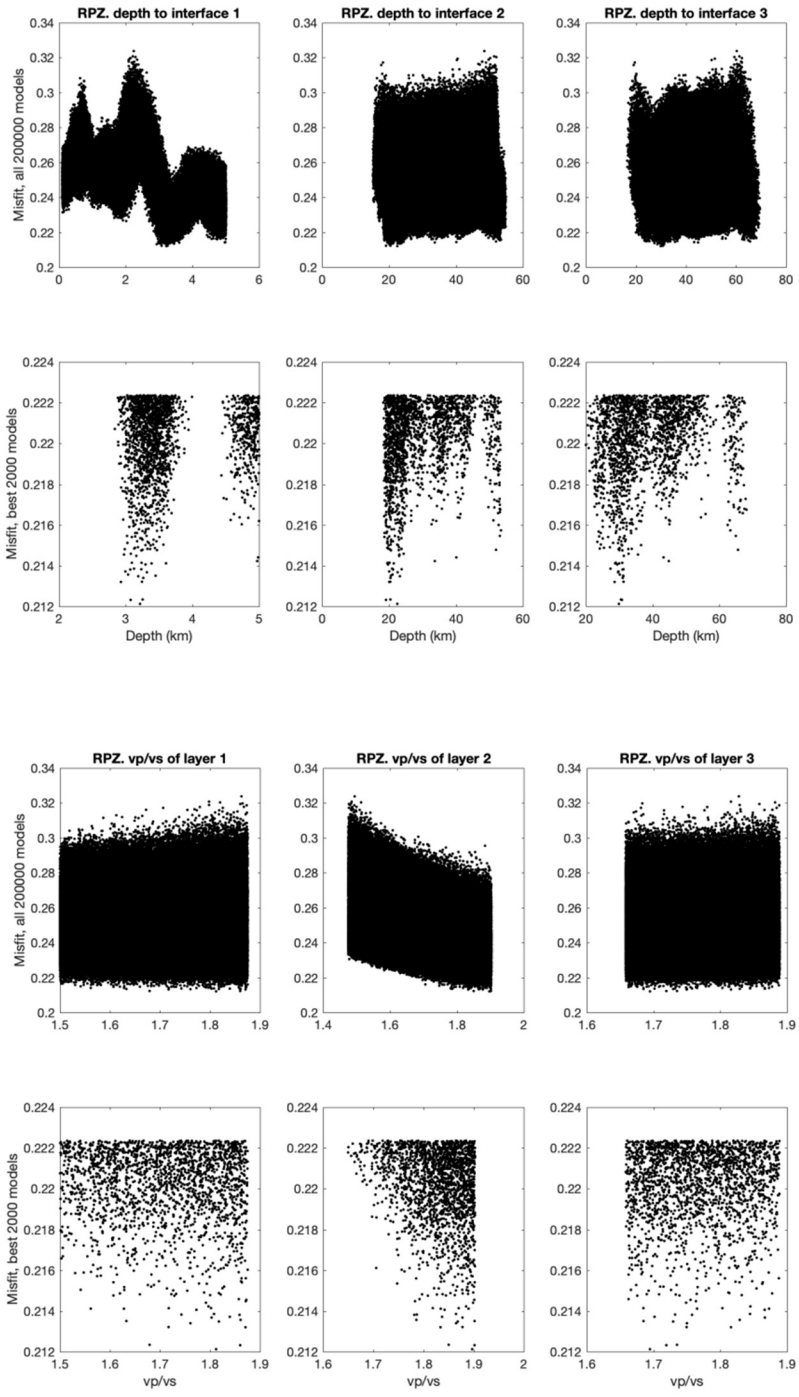

Figure 10.21: The best 2000 models for station RPZ. The best model has the following values: ***Layer 1*** *- Crustal thickness: 3.2 km;* ***Layer 2*** *- Crustal thickness: 19.2 km and Vp/Vs 1.90;* ***Layer 3*** *-Crustal thickness: 7.5 km; Misfit: 0.21.*

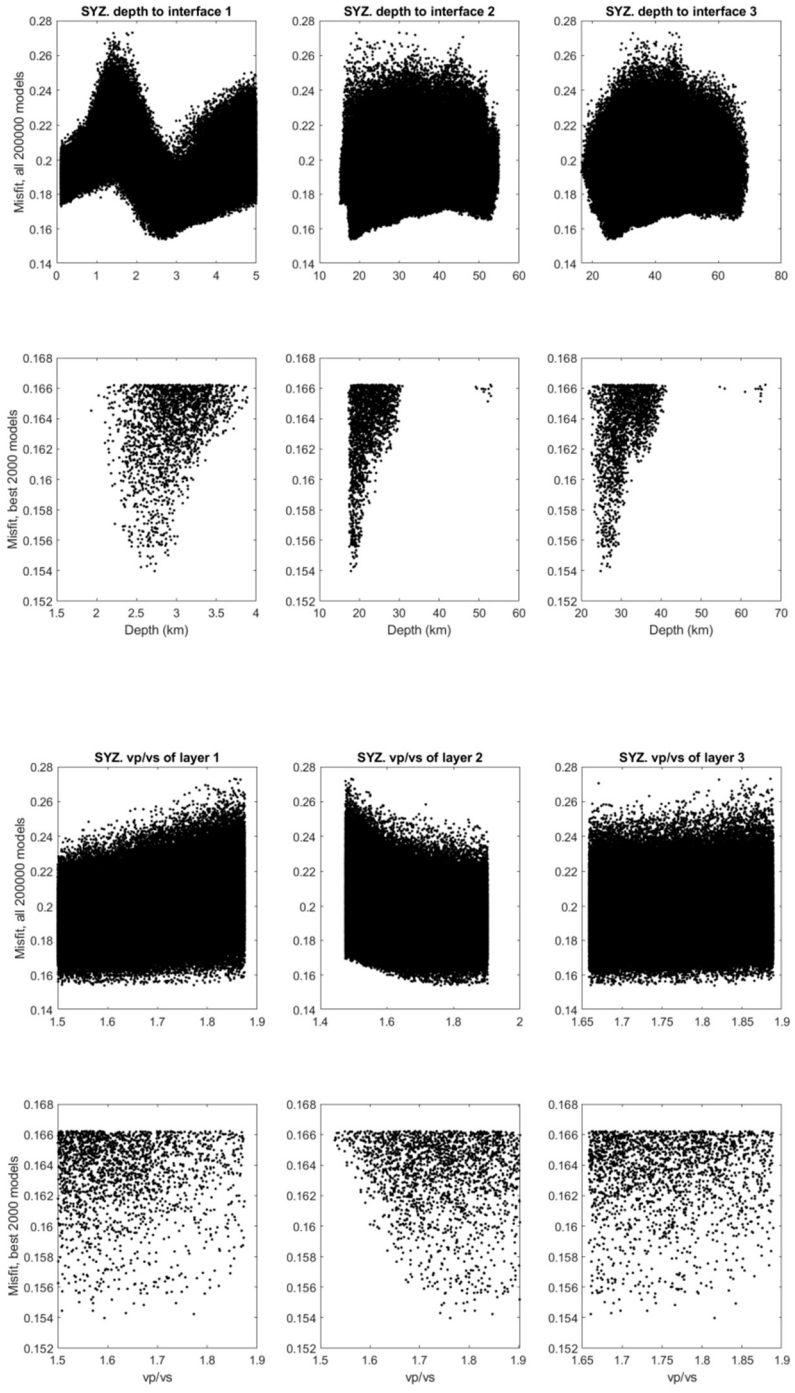

Figure 10.22: The best 2000 models for station SYZ. The best model has the following values: ***Layer 1*** *- Crustal thickness: 2.7 km;* ***Layer 2*** *- Crustal thickness: 15.2 km and Vp/Vs 1.76;* ***Layer 3*** *-Crustal thickness: 6.9 km; Misfit: 0.15.*

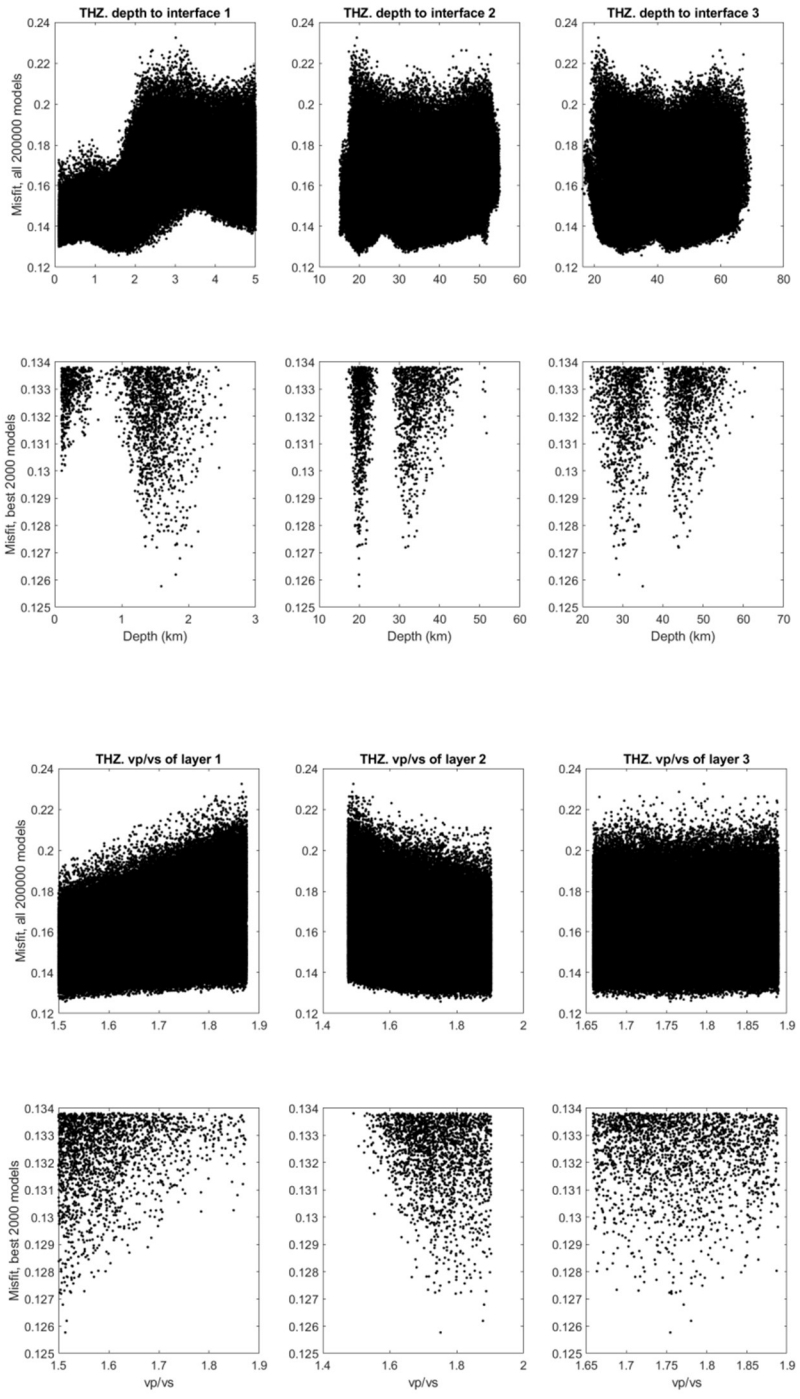

Figure 10.23: The best 2000 models for station THZ. The best model has the following values: ***Layer 1*** *- Crustal thickness: 1.6 km;* ***Layer 2*** *- Crustal thickness: 18.4 km and Vp/Vs 1.75;* ***Layer 3*** *-Crustal thickness: 15.0 km; Misfit: 0.13.*

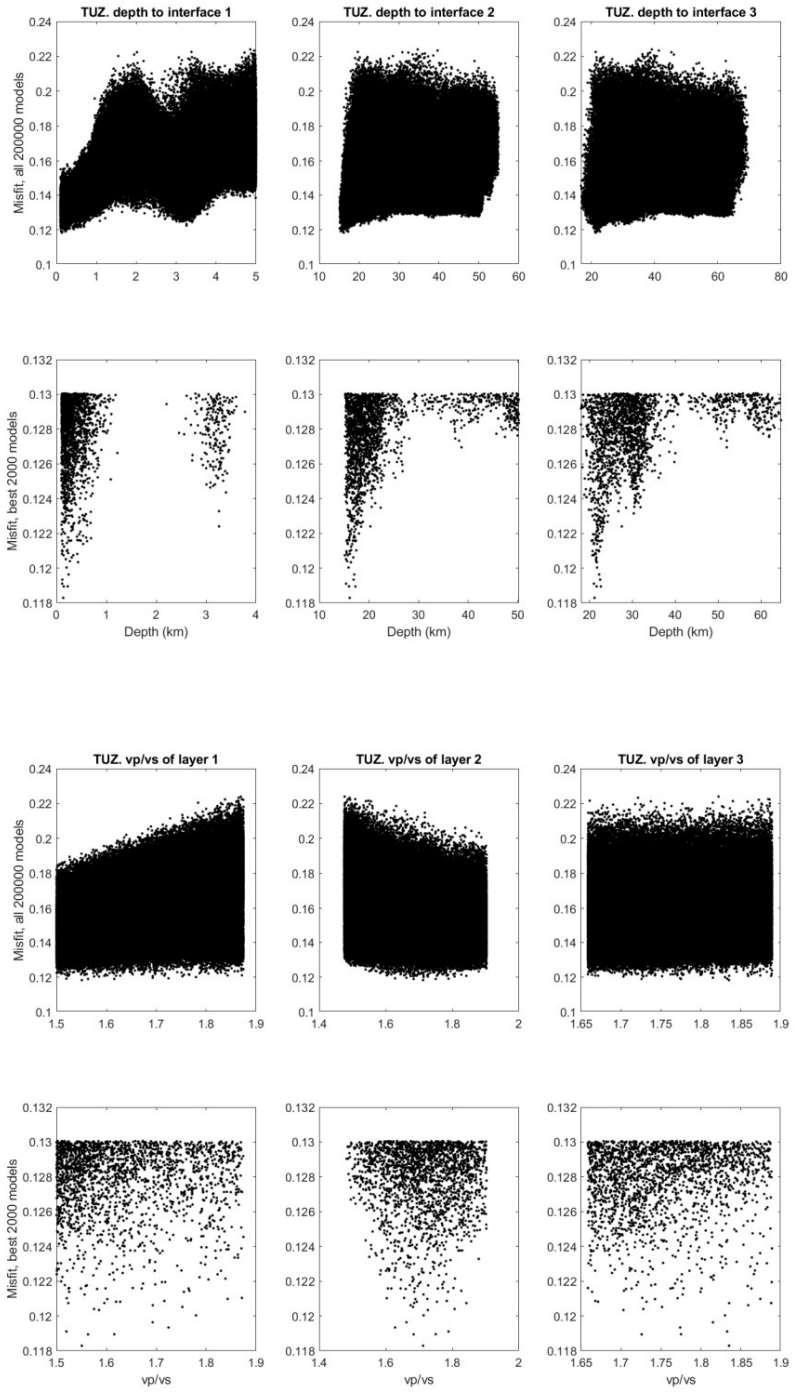

Figure 10.24: The best 2000 models for station TUZ. The best model has the following values: ***Layer 1*** *- Crustal thickness: 0.1 km;* ***Layer 2*** *- Crustal thickness: 16.0 km and Vp/Vs 1.71;* ***Layer 3*** *-Crustal thickness: 5.1 km; Misfit: 0.12.*

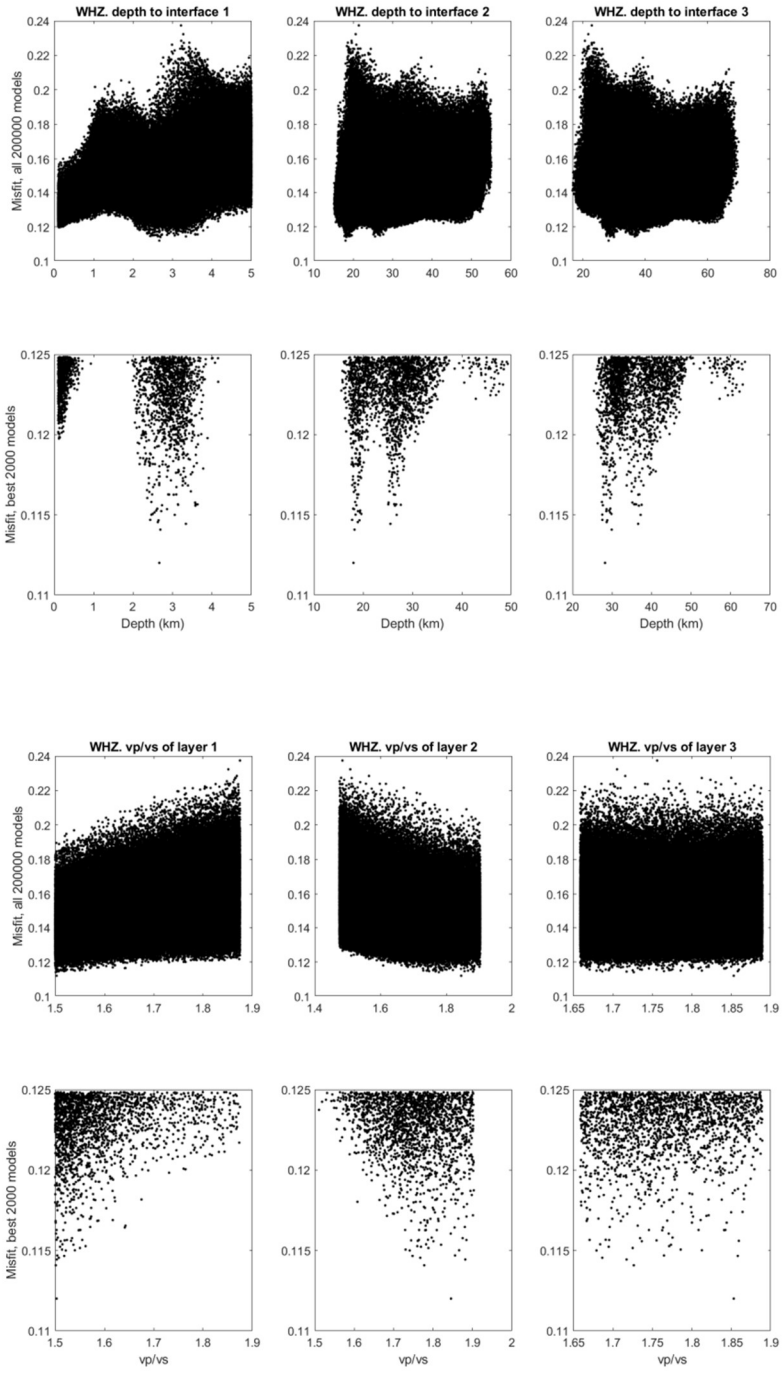

Figure 10.25: The best 2000 models for station WHZ. The best model has the following values: ***Layer 1*** *- Crustal thickness: 2.7 km;* ***Layer 2*** *- Crustal thickness: 15.4 km and Vp/Vs 1.85;* ***Layer 3*** *-Crustal thickness: 10.2 km; Misfit: 0.11.*

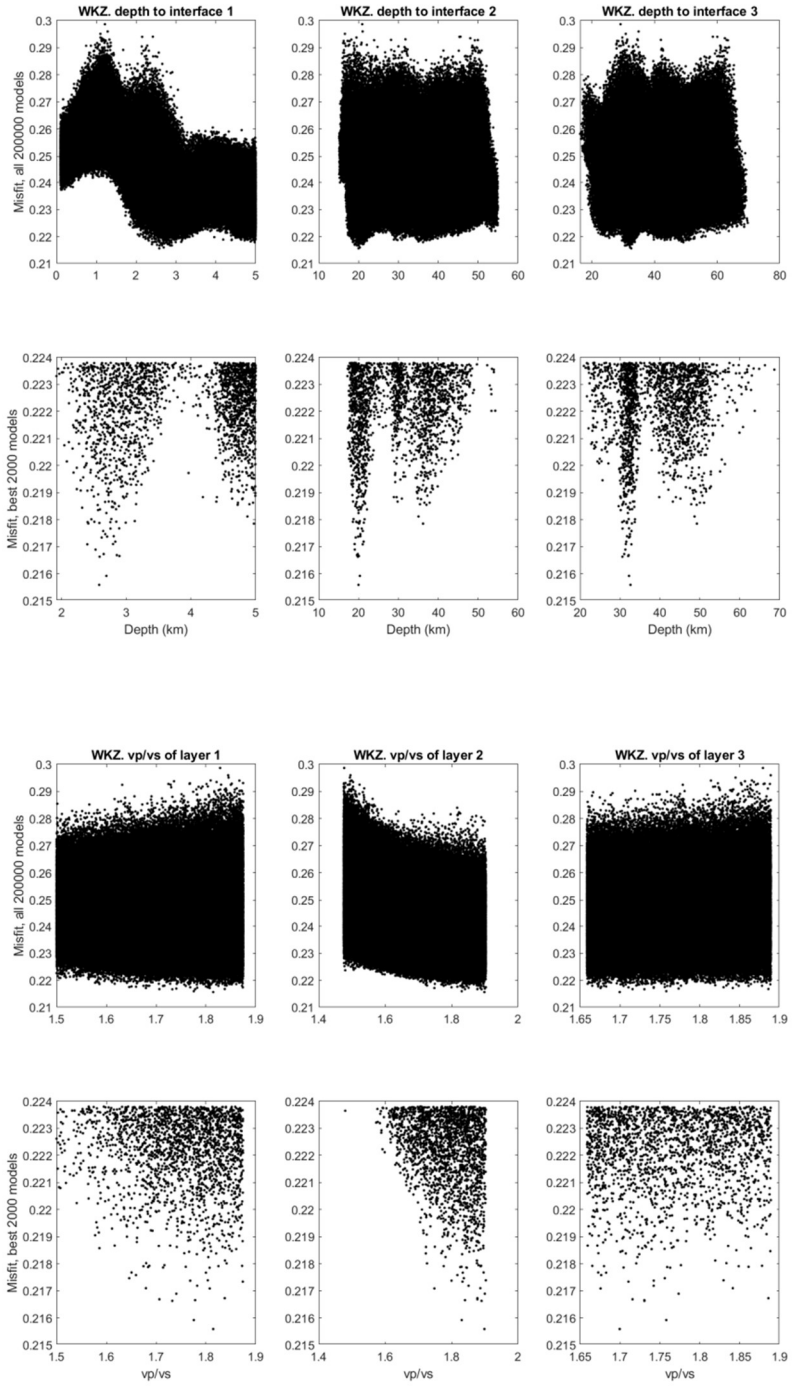

Figure 10.26: The best 2000 models for station WKZ. The best model has the following values: ***Layer 1*** *- Crustal thickness: 2.6 km;* ***Layer 2*** *- Crustal thickness: 17.4 km and Vp/Vs 1.90;* ***Layer 3*** *-Crustal thickness: 12.6 km; Misfit: 0.22.*

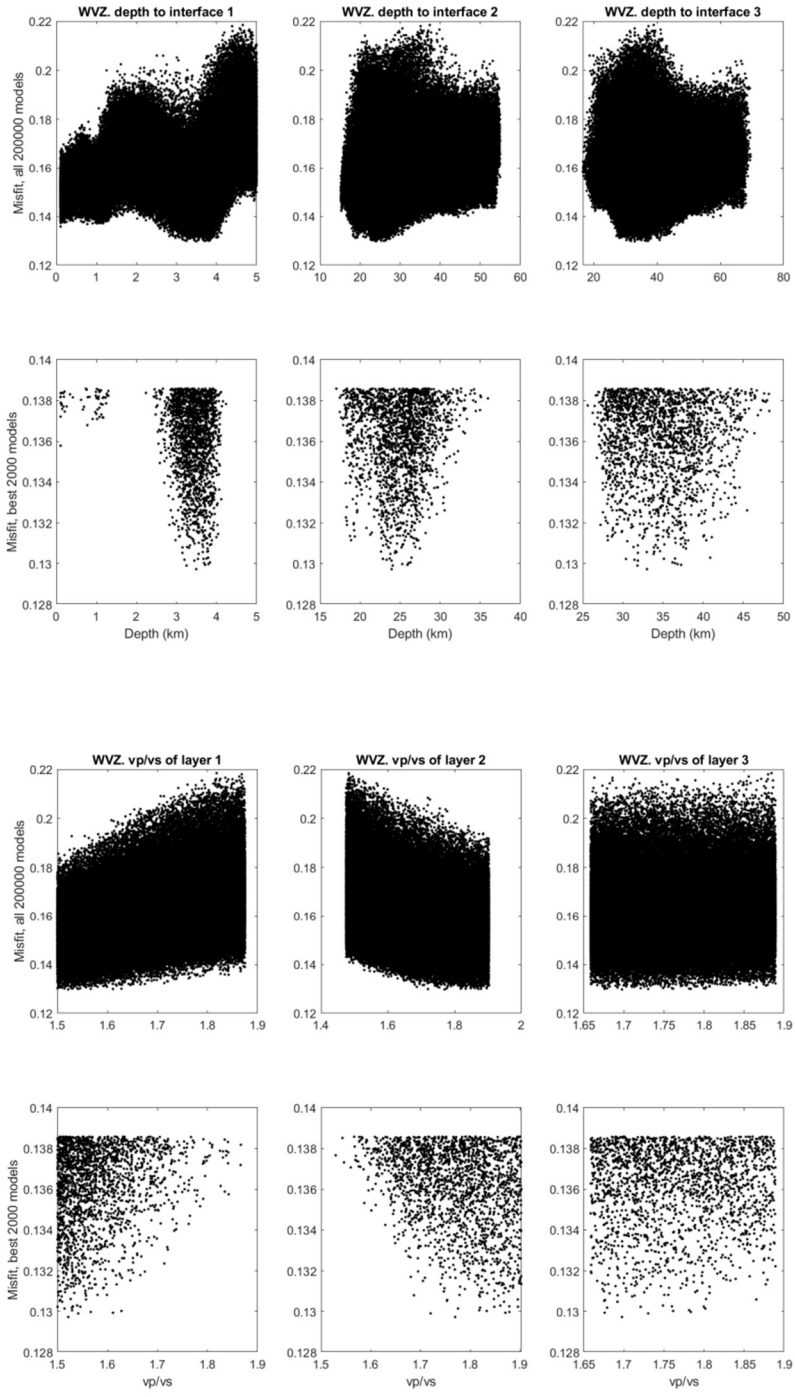

Figure 10.27: The best 2000 models for station WVZ. The best model has the following values: ***Layer 1*** *- Crustal thickness: 3.5 km;* ***Layer 2*** *- Crustal thickness: 20.4 km and Vp/Vs 1.77;* ***Layer 3*** *-Crustal thickness: 9.1 km; Misfit: 0.13.*